



EPFL

MASTER THESIS

Analyzing the effects of snow-atmosphere
interactions on snow surface dynamics based on
automated 3D laser scanning data

Student:

Loïc BROUET

Supervisors:

Prof. Dr. Michael LEHNING

Dr. Benjamin WALTER

Davos, April 2022

Abstract

The snow surface morphology is shaped throughout a winter season by atmospheric conditions, like precipitation, wind, solar irradiance, air temperature or relative humidity. Changes in morphology affect the snow surface roughness which influences the turbulent fluxes of sensible and latent heat, and thus the surface energy balance. The aerodynamic roughness length (z_0) is an important parameter to calculate the turbulent fluxes and to characterise the interaction between the atmosphere and the snow surface. However, z_0 values used to characterize snow surfaces are rare and often generalized. Moreover, direct measurements are often difficult to achieved and associated with large uncertainty. This study used a fixed automated high-resolution 3D laser scanner to continuously map the snow surface on an hourly basis. The methods of processing point clouds allow to derive surface roughness height maps. These maps were applied to several models to estimate z_0 values for each scan, based on the microtopographic approach. To validate the geometric z_0 values derived from the scanner, a sonic anemometer is used to directly measure the anemometric z_0 values on the study area. The results first highlight the robustness of the laser scanner and the methods used to derive snow height maps and snow roughness maps. The Lettau model for the derivation of z_0 from the scans was found to agree best with the measured z_0 values from the sonic during stable wind conditions. This point out that the z_0 values over the snow season range from 0.1 mm to 4 mm. Furthermore, the chosen interpolation cell size for the methods based on Lettau's equation and the window moving filter size for the detrending process turned out to have a large impact on the z_0 values, presenting a range up to 1 order of magnitude each or more. Snow surface reflectance values from the scanner were found to be representative of the surface snow grain size and shape under certain atmospheric conditions.

Keywords

Remote sensing, terrestrial laser scanning, surface roughness, snow, aerodynamic roughness length

Acknowledgements

My first acknowledgments go to my supervisors, Michi Lehning and Benni Walter, for giving me the chance to do this master thesis at SLF. Thanks a lot for the time invested in the completion of this thesis, and also for your encouragement, your guidance, and the freedom granted in the work.

I would like to thank also the Snow Physics group for the welcoming and motivating atmosphere. Thanks to Henning Löwe for the help, the precious advice, and for having me in his group. Thanks also to Matthias Jäggi for the help with the laser scanner installation in the field site.

Finally, many thanks to all the people I have met in Davos, with whom I shared ski tours, cross-country ski, bike tours, runs, evenings, in brief life in Davos, thank you for having these few months a enriching and unique experience.

Table of contents

Abstract	i
Acknowledgements	ii
1 Introduction	1
1.1 Background	1
1.2 Aims and scope of this thesis	3
2 Field site, experimental setup and data acquisition	4
2.1 Location	4
2.2 Experimental setup	5
2.2.1 Laser scanner	5
2.2.2 Sonic anemometer	10
2.3 Data acquisition	12
2.3.1 Laser scanner	12
2.3.2 Sonic anemometer	13
2.3.3 Meteorological and snow data	13
3 Methods	14
3.1 Preprocessing of the laser scanner data	14
3.1.1 Raw data	14
3.1.2 Segmentation	15
3.1.3 Cloth simulation filter	16
3.1.4 Point cloud interpolation	17
3.1.5 Digital elevation model detrending	18
3.2 Microtopographic z_0 derivation	19
3.2.1 Up-crossing frequency method	19
3.2.2 Raster method	21
3.3 Anemometric z_0 derivation	25
4 Results and discussion	26
4.1 Preprocessing of the laser scanner data	26
4.1.1 Snow height monitoring	26
4.1.2 Non-ground points	27
4.1.3 DEM interpolation: cell size sensitivity analysis	31
4.1.4 DEM detrending: window size sensitivity analysis	32
4.2 Aerodynamic roughness length z_0	36
4.2.1 Microtopographic method	36
4.2.2 Anemometric method	39
4.2.3 Comparison	40
4.3 Surface snow type analysis	44
5 Conclusions and Outlook	54
A Additional pictures	55
References	60

1 Introduction

Precipitation, air temperature, wind and solar irradiance are the main drivers shaping the snow surface morphology throughout a winter season. Snow surface features like sastrugis, ripples or rain funnels increase the snow surface roughness resulting in a larger surface area exposed to the atmosphere, also increasing the turbulence over the snow surface when the wind is blowing. Surface characteristics may significantly affect the surface energy balance, the mechanical stability of snow layers, or the exchange of chemical species with the atmosphere (isotopic composition).

To complete the surface energy budget, the turbulent fluxes of sensible and latent heat play an important role (Hock and Holmgren, 2005) but are particularly difficult to represent in modelling studies because of a lack of empirical data describing key surface processes and characteristics. A key parameter to derive the turbulent fluxes of sensible and latent heat between the snow surface and the atmosphere is the aerodynamic roughness length z_0 . In fact, the transfer coefficients of the turbulent fluxes (with the Bulk approach) are depending on z_0 which remains a major uncertainty and is one of the least understood and poorly parameterised property for the turbulent fluxes. Its correct parameterisation is critical in surface energy balance studies, since an order of magnitude change in z_0 can lead to a factor of two change in estimated turbulent fluxes (Munro, 1989, Hock and Holmgren, 1996, Brock et al., 2006). Moreover, turbulent fluxes are driven by the temperature and moisture gradient between the snow surface and air. An increase in the air temperature, e.g. in the context of climate change, increases the contribution of turbulent fluxes to the snow surface due to the larger temperature gradient.

z_0 is usually derived from wind speed measurements using anemometers. Typical values of z_0 on snow surfaces range from 0.01 mm to 20 mm. Nevertheless, calculating z_0 with wind speed sometimes requires a heavy and permanent station, providing only a single value per station. Another technique developed in the field of glaciology allows to derive z_0 from topographic data by using high resolution laser scanners (Smith et al., 2016). This novel technique makes it possible to characterize the surface roughness and to derive z_0 without large meteorological stations. Another advantage lies also in the characterisation of large surfaces for instance.

This work aims to assess the application of TLS to derive the temporal evolution of z_0 values from topographic data of a snow surface with very frequent scans. The work includes the preprocessing of the laser scanner data (Section 3.1 and 4.1), the derivation of z_0 from the DEMs with different models (Section 3.2 and 4.2.1), a validation of z_0 values against a sonic anemometer (Section 3.3, 4.2.2 and 4.2.3), and an analysis of the surface snow type based on the snow reflectance values (Section 4.3).

1.1 Background

The aerodynamic roughness length, also called z_0 , is the theoretical height above a surface at which the extrapolated horizontal wind velocity on a logarithmic profile drops to zero (Prandtl, 1926). It is also considered as a surface characteristic and is the length scale that characterises the loss of wind momentum attributable to surface roughness (topographical influence) (Smith et al., 2020). It's an indicator on the turbulent heat exchange rate between the snow surface and air. Usually the turbulent fluxes are derived from direct measurement of basic atmospheric variables such as the wind speed, the air temperature and the humidity. There exist three main methods to calculate the turbulent fluxes. The eddy covariance method often uses sonic anemometers to record the air movement in turbulent eddies. The profile method estimates the turbulent fluxes by doing an interpolation of the wind speed profile close to the surface. The bulk approach approximates the turbulent fluxes with basic atmospheric measurements and with z_0 values (i.e with the potential temperature and the specific humidity) (Chambers et al., 2020).

Despite the importance of this parameter, surface energy balance studies regularly use a spatially and temporally invariant value to represent z_0 , and often simply assume values based on data from previously published studies rather than measuring or parameterising surface roughness using in situ observations. A reason is that direct

measurements (eddy correlation or wind profile) need to construct and maintain meteorological stations which can be time consuming, costly and particularly difficult for remote areas (Quincey et al., 2017). Moreover, direct measurements can give only a point based value on z_0 . However, field observations show that z_0 changes spatially and temporally, and thus z_0 incorporated as a dynamic parameter may greatly improve models.

An increasing number of studies have sought to develop methods for quantifying z_0 over snow surfaces (Sanow et al., 2018), glaciers (Irvine-Fynn et al., 2014, Smith et al., 2016, Miles et al., 2017) and others surfaces (Nield et al., 2013, Eitel et al., 2011), using digital elevation models (DEMs) as a data source. They have shown that DEMs derived from terrestrial laser scanning and photogrammetry can provide estimates of the surface roughness where independent aerodynamic measurements are not available. The use of laser scanning is not new in the field of snow processes. DEMs are often used to calculate snow depth changes by comparing two DEMs captured at different times (e.g. Mott et al. (2010)), but today the availability and the use of high-resolution topographical data has greatly increased. In this thesis we focus on the use of DEMs to study the surface roughness. The ability of the DEM data to model snow surfaces at the millimetric or centimetric scale gives the possibility of calculating spatially and temporally varying z_0 based on measurements of surface microtopography (Rounce et al., 2015). Nonetheless, quantifying both spatial variation and temporal change of z_0 remains a key research challenge (Quincey et al., 2017). Microtopographic methods for estimating z_0 have become prominent in the literature in recent years, but are rarely validated against independent data or measurements (Brock et al., 2006). Considering how the measurements vary over a range of different surface types or scales, a comprehensive analyses for a scale and data resolution dependency is required. Furthermore, the campaigns are often conducted for short periods of time which is less relevant for a long term temporal variability. Estimating z_0 from topographic data allows to estimate the turbulent fluxes without meteorological stations, where a topographical z_0 can be used as an input for the bulk approach.

LiDAR (Light Detection And Ranging) systems are powerful to produce DEMs, with the main advantage of the possibility of collecting data at a very high spatial resolution and with a high temporal resolution. Therefore, a LiDAR provides a good possibility to continuously study the temporal and spatial variability of a snow surface. The major drawback is that they are quite expensive. Accordingly, the thesis follows an approach where LiDAR provides a large amount of high-resolution topographic data which then is used to build DEMs and estimate z_0 , and finally to evaluate its temporal evolution.

Many studies investigated z_0 values of glacier surfaces by using different approaches, with the aim of better estimating the surface energy balance (Smith et al. (2016), Quincey et al. (2017), Chambers et al. (2020), Dachauer et al. (2021)). However, still little is investigated about z_0 values for snow surfaces, where z_0 may vary because of snow surface morphology changes due to various atmospheric forcings like wind, solar irradiance or precipitation, and its implication on the turbulent heat exchange between snow surface and the atmosphere. The varying size of snow obstacles and their spatial distribution makes it difficult to define a single z_0 value for a given area. Moreover, the wind direction can have an effect on z_0 values, as the exposed area of the obstacles are not necessarily isotropic (Smith et al., 2016).

Here, we present the methods and results of a field investigation conducted at Weissfluhjoch (SLF Davos, Switzerland) over two winter seasons. A fixed automated high-resolution 3D laser scanner (FARO S120) was operated throughout the winter season 2020/2021 and 2021/2022 at the WSL/SLF Weissfluhjoch field site to continuously map the snow surface on an hourly basis. This unique data set allows to track changes in the snow height and surface morphology. The topographic data allow to derive surface roughness indicators as well as the aerodynamic roughness length of the snow surface for each scan. Moreover, a sonic anemometer has been installed in the laser scan area, to have an independent reference to compare the geometric and anemometric roughness length.

1.2 Aims and scope of this thesis

The aim of this master thesis is to assess the application of TLS to derive z_0 from topographic data, by using in particular a sonic anemometer to get reference measurements and to validate the z_0 values derived with the TLS. Then the aim is to derive z_0 temporal changes. The purpose is to improve our understanding of the effect of atmospheric conditions on the surface roughness and the resulting influence on the aerodynamic roughness length over the time on a snow surface. In a broader sense, it is about correlating spatio-temporal snow surfaces morphology variations measured with an automated 3D laser scanner to alpine atmospheric conditions. Section 2 describes the field site, the experimental setup and the data acquisition. Section 3 includes the methods from the raw point cloud to the calculation of the geometrical z_0 , and the derivation of the anemometric z_0 . Section 4 presents the results, first with the preprocessing of laser scanner data (Section 3.1) where the snow height is monitored, the cause of the non-ground points is investigated, and a sensitivity analysis is conducted on the cell size for the interpolation process and on the window size for the detrending process. Afterwards, the results of the z_0 from the DEMs and from the sonic are presented, and compared to evaluate which model better estimate z_0 from the scans (Section 4.2). Finally an assessment of the potential of the laser scanner to distinguish different surface snow types based on the reflectance values is presented (Section 4.3).

2 Field site, experimental setup and data acquisition

This work is based on datasets from the laser scanner, the sonic anemometer and also from different meteorological measuring device from the WFJ field site. This chapter presents the study site, the experimental settings and the data used in this work.

2.1 Location

The field site is located in Davos (Graubünden, Switzerland), highlighted by the red star on the Swiss map (Fig.2.1 a)), below the summit of Weissfluhjoch (2686 m.a.s.l.) on its South-East slope on a flat area at 2539 m.a.s.l. ($46^{\circ}49'47''\text{N}$ $9^{\circ}48'33''\text{E}$) (Fig.2.1 b)). Hereafter, Weissfluhjoch or WFJ refers to the test site and not to the peak. A map of the WSL/SLF Weissfluhjoch field site is presented at a smaller scale in Fig.2.1 c), where the SLF measurement station is delimited by a blue rectangle, the laser scanner is marked by a green dot and the scanned snow surface is indicated in yellow (not to scale). The long hut and the small hut are also indicated in black on the map. The field site is relatively flat, and a small hill situated on the South-East (point 2544 m.a.s.l.) makes the site fairly wind sheltered from all directions, however there is still wind coming mostly from the North-West. The study area approaches the small hill around point 2544 m.a.s.l. from the flat area and then has a slight slope of about 6-7 % (see in Fig. 2.2).

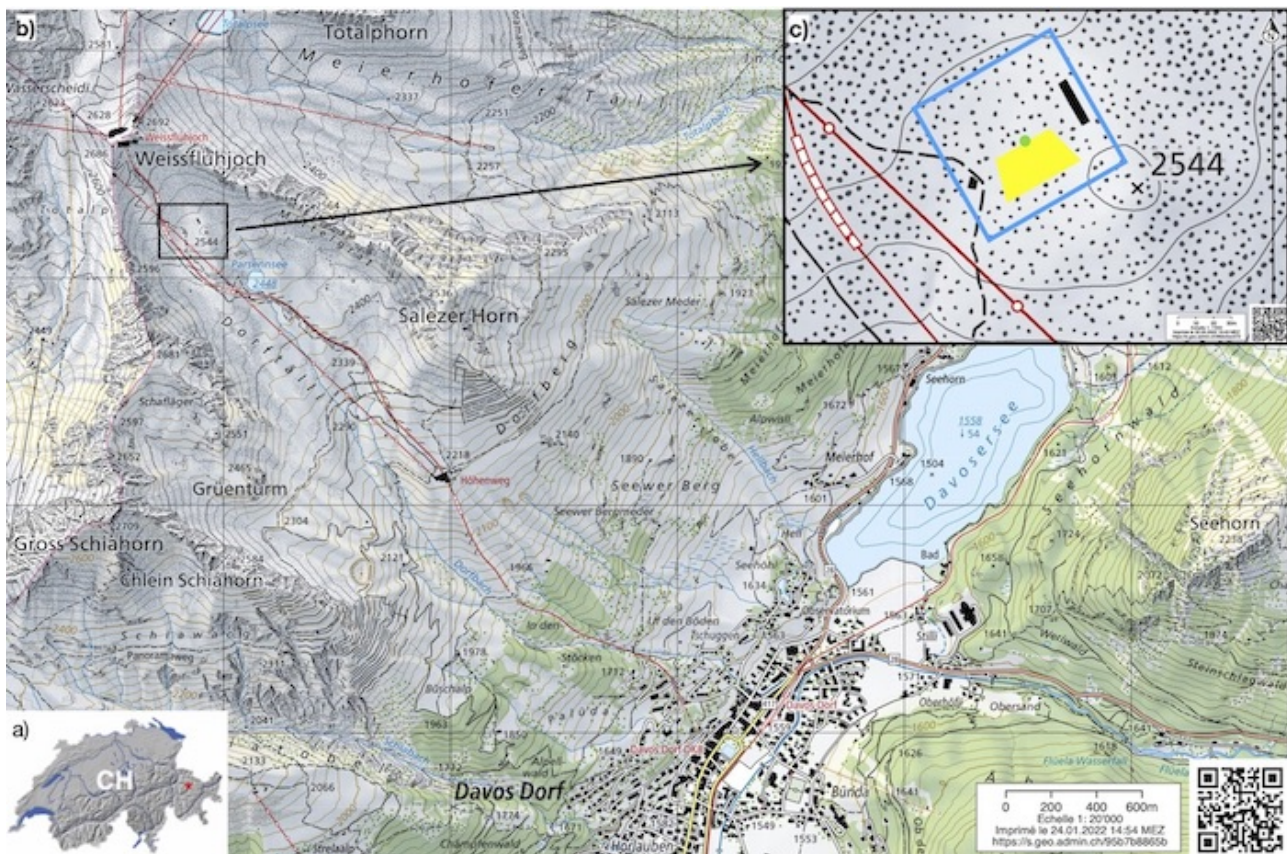


Figure 2.1: Field site

WFJ field site has the longest series of snow measurements for a high-altitude research station. The measurements started in 1936, which makes it one of the most important station for long-term observations in the Alps (Marty and Meister, 2012). Meteorological data is provided by (Weber, 2017) and (SLF, 2020). Among them, precipitation (RR), air temperature (TA), snow surface temperature (TSS), snow height (HS), wind speed (VW), wind direction (DW), relative humidity (RH) and solar radiation are measured continuously by automatic stations. In addition, new snow (HN) and a second HS measurement are taken manually every morning.



Figure 2.2: Study area (photo: Luca Bianchi). The scanner is located in the green circle.

2.2 Experimental setup

2.2.1 Laser scanner

A terrestrial laser scanner (TLS) is used to generate three-dimensional point clouds of the snow surface. The laser scanner has been installed on a metallic fixed structure at a height of about 5 m above the bare ground. This elevated position helped to increase the field of view and to decrease the incidence angle, which is the angle between the laser beam and the surface normal. Nevertheless, the incidence angle was large in the far field which occasionally led to measurements shadows. The scanner is located in the green circle in Fig. 2.2 and it points towards the South-East. A metallic half-box has been built to protect it from precipitation and wind, to avoid water entering the scanner, to eliminate the formation of hoarfrost, to prevent the internal temperature of the scanner from dropping too much with the wind chill effect and to protect it from direct solar radiation.

The scanner is connected to a rugged computer placed in a waterproof box at the foot of the metallic structure (see Fig. A.1), to operate the automated scanner and to automatically transfer the scans on a web server once acquired. The scanner is connected to the Internet via an Ethernet cable buried in the snow to the long hut. The scanned surface is surrounded with wooden piles and a rope so that no one enters the area and changes the snow surface. Moreover this guarantees a safe distance for the eyes in case people would be around the area without security glasses while the scanner is running. Indeed, it is difficult to know if a scan is in progress because the laser beam at 905nm is invisible and the scanner makes a low noise while it is operating. Warning labels have been placed on all ropes around the area, indicating that the area should not be crossed and that it is a category 3B laser that can cause eye injuries if the instructions are not followed correctly. The eye safety distance is, nevertheless, 6 m which is about the height of the scanner above the snow surface. So even in case people would ignore the safety warnings by entering the field and looking up to the scanner, eye safety is still guaranteed. A TLS is a terrestrial LiDAR system, which is an active remote sensing technique as it provides its own energy source for illumination. The advantage for active sensors is the ability to obtain measurements anytime, regardless of the time of a day or the season. The use of TLS has greatly increased since two decades to monitor the alpine environment such as landslides, avalanches, snow depth distribution, etc. The laser scanner model is a FARO® Focus3D S120 which is illustrated in Fig. 2.3. It is a high-speed three-dimensional laser scanner able to produce an assembly of millions of 3D measurement points of the environment (3D images) in a few minutes.

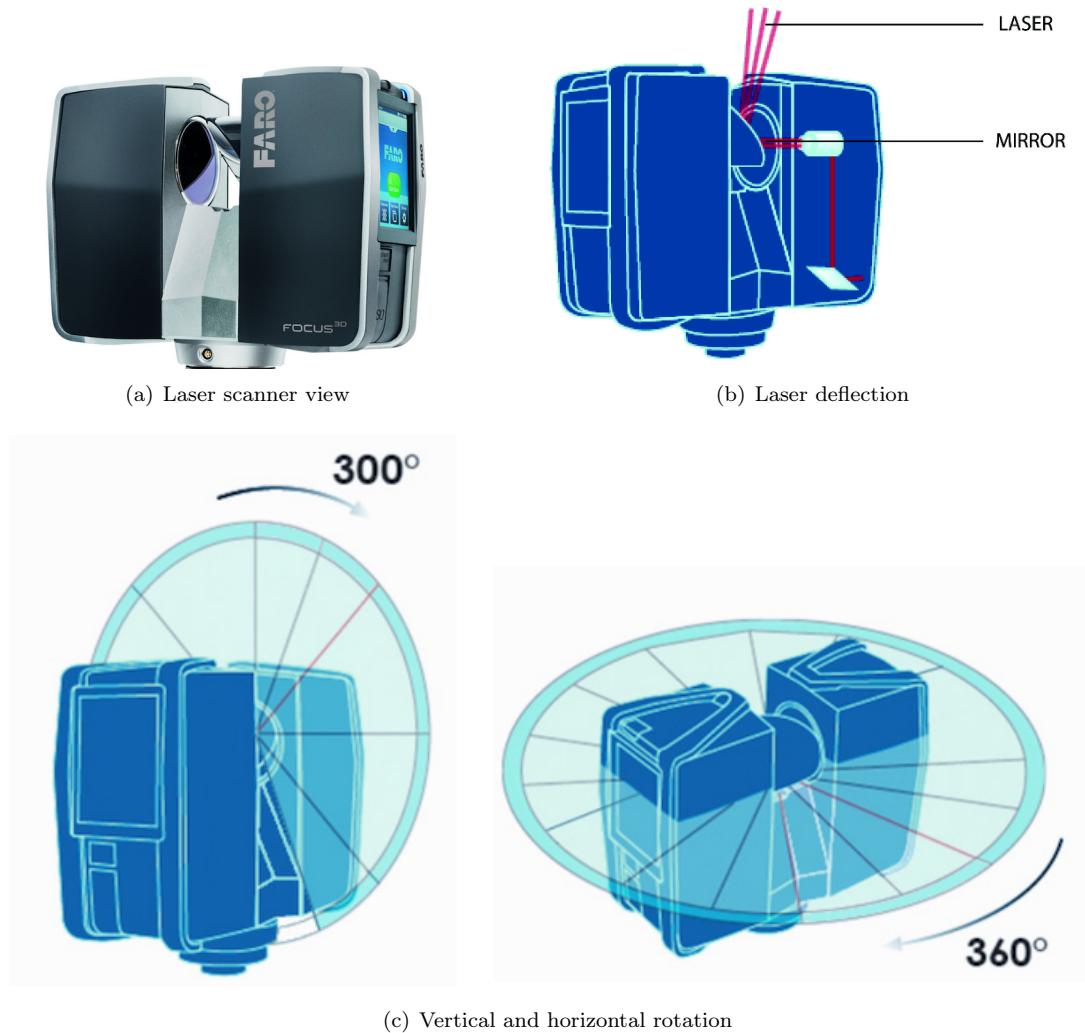


Figure 2.3: Faro Focus 3D S120 (FARO®)

The Focus3D works by sending an infrared laser beam to the center of its rotating mirror. The mirror deflects the laser beam on a vertical rotation around the environment being scanned (see Fig. 2.3(b)). The scattered light from surrounding objects is then reflected back to the scanner. The Focus3D scanners use phase shift technology to measure the distance, the scanner emits waves of different wavelengths which are then reflected back to the scanner. The distance from the scanner to the object is accurately determined by measuring the phase shifts between the emitted and the backscattered waves of the infrared light. The laser scanner uses phase-shift algorithms to determine the distance based on the unique properties of each individual phase based on this formula: $\text{Time of Flight} = \text{Phase Shift} / (2\pi \times \text{Modulation Frequency})$.

Phase-based scanners are able to collect data at a much faster speed than time-of-flight scanners, but their effective distance is much shorter. Additionally, phase-based scanners typically have more "noise" or false data, than time-of-flight scanners. The signal-to-noise ratio of the modulated signal is enhanced thanks to a modulation technique developed by Faro called "HypermodulationTM". The x, y, z coordinates of each point are then calculated by using angle encoders to measure the mirror rotation and the horizontal rotation of the laser scanner. These angles are encoded simultaneously with the distance measurement. Distance, vertical angle and horizontal angle make up a polar coordinate (δ, α, β) , which is then transformed to a Cartesian coordinate (x, y, z) . The scanner can cover a $360^\circ \times 300^\circ$ field of view (see Fig. 2.3(c)). In our case, to cover the entire study area, the scanner has the following settings: vertical rotation of -62.5° to 70° , and an horizontal rotation 200° to 340° .

In addition, the laser scanner determines the reflectivity of the captured surfaces by measuring the intensity of the backscattered laser signal. In general, bright surfaces reflect a greater portion of the emitted light than dark surfaces. This reflectivity value is used to assign a corresponding grey value to every single point.



Performance Specifications Focus^{3D}S

Ranging unit

Unambiguity interval: 153.49m (503.58ft)
 Range Focus^{3D}S 120¹: 0,6m - 120m indoor or outdoor with low ambient light and normal incidence to a 90% reflective surface
 Range Focus^{3D}S 20: 0,6m - 20m at normal incidence on >10% matte reflective surface
 Measurement speed (Pts/Sec): 122,000 / 244,000 / 488,000 / 976,000
 Ranging error²: ±2mm at 10m and 25m, each at 90% and 10% reflectivity

Ranging noise ³	@10m	@10m - noise compressed ⁴	@25m	@25m - noise compressed ⁴
@ 90% refl.	0.6mm	0.3mm	0.95mm	0.5mm
@ 10% refl.	1.2mm	0.6mm	2.20mm	1.1mm

Colour unit

Resolution: Up to 70 megapixel colour
 Dynamic colour feature: Automatic adaption of brightness

Deflection unit

Field of view (vertical/horizontal): 300° / 360°
 Step size (vertical/horizontal): 0,009° (40,960 3D-Pixel on 360°) / 0,009° (40,960 3D-Pixel on 360°)
 Max. vertical scan speed: 5,820rpm or 97Hz

Laser (Optical transmitter)

Laser power (cw Ø): 20mW (Laser class 3R)
 Wavelength: 905nm
 Beam divergence: Typical 0.19mrad (0.011°)
 Beam diameter at exit: Typical 3.0mm, circular

Data handling and control

Data storage: SD, SDHC™, SDXC™; 32GB card included
 Scanner control: Via touchscreen display and WLAN
 New WLAN access: Remote control, Scan Visualisation and download are possible on mobile devices with Flash®

Multi-Sensor

Dual axis compensator: Levels each scan: Accuracy 0,015°; Range ± 5°
 Height sensor: Via an electronic barometer the height relative to a fixed point can be detected and added to a scan.
 Compass: The electronic compass gives the scan an orientation. A calibration feature is included.



¹ Depends on ambient light, which can act as a source of noise. Bright ambient light (e.g. sunshine) may shorten the actual range of the scanner to lesser distances. In low ambient light, the range can be more than 120m for normal incidence on high-reflective surfaces. ² Ranging error is defined as the maximum error in the distance measured by the scanner from its origin point to a point on a planar target for normal incidence excluding noise. ³ Ranging noise is defined as a standard deviation of values about the best-fit plane for measurement speed of 122,000 points/sec. ⁴ A noise-compression algorithm may be activated to average points in sets of 4 or 16, thereby compressing raw data noise by a factor of 2 or 4. Subject to change without prior notice.

General

Power supply voltage: 19V (external supply), 14.4V (internal battery)
 Power consumption: 40W and 80W (while battery charges)
 Battery life: Up to 5 hours
 Ambient temperature: 5° - 40°C
 Humidity: Non-condensing

Cable connector: Located in scanner mount
 Weight: 5.0kg
 Size: 240 x 200 x 100mm
 Maintenance / calibration: Annual
 Parallax-free: Yes



Figure 2.4: Faro Focus 3D S120 technical specifications

The technical specifications of the Faro Focus 3D S120 are presented in Fig. 2.4. The user can choose different settings for the acquisition, related to the spatial resolution and the measurement speed, which gives at the end a point cloud with a certain number of points. The scanner can be remotely controlled via an Internet connection.

Here, the settings were chosen as a trade of between resolution and the resulting size of the file. This resulted in measurement speed of 488'000 Points/second. The resulting point cloud has about 60 millions points and the time for one scan was about 2 min. The resolution is set to "1/2" which means that the number of scan columns and rows are 1/2 of the scan at the full resolution "1". There is no noise compression, namely the number of points is not reduced. The point density on snow surface varies between the order of magnitude of 10^5 pts/m^2 and 10^3 pts/m^2 according to the horizontal distance from the scanner. This is due to the fact that with a fixed angular resolution the point density decreases as a function of distance and incidence angle of the laser beam.

The points are spaced horizontally at about 2 mm in the x direction and about 4 mm in the y direction, however this is an average because the spatial resolution depends on the object surface type and reflectance, as well as the object orientation relative to the scanning beam, the distance and the incident angle. For these settings, the time of scanning is about 2 min, and one scan is done each hour, so the temporal resolution is then 1h. It is assumed that the snow surface is not changing during the scanning time and that it is representative for the time of the scan. The laser wavelength is 905 nm (Near Infra-Red). This wavelength makes it specifically suitable to scan snow surfaces, which have a high reflectance at 905 nm. The light penetration is relatively small in snow at this wavelength (Prokop, 2008). The distance accuracy is about 1 mm as stated by Faro (see Fig. 2.4). Moreover a test conducted in comparing two scans close in time showed that the accuracy is about $\pm 1.5 \text{ mm}$ (see Fig. 2.5), so that the accuracy stated by Faro holds also for snow surfaces.

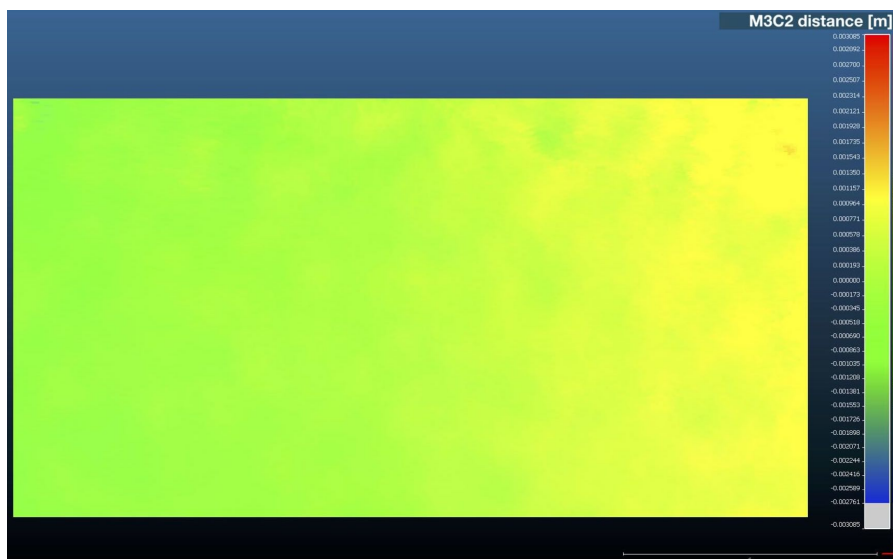


Figure 2.5: Difference between the scan on 2021-02-26 11:25 and 2021-02-26 12:25. The M3C2 (Multiscale Model to Model Cloud Comparison (Lague et al., 2013)) distance is the distance between the two point clouds.

The scanner doesn't have a GPS, so the absolute position of the laser scanner is not known and the point clouds can not be georeferenced (e.g. in a global coordinates system), so the point clouds are referenced in a local coordinate system. Georeferencing point cloud can be essential in the case where two datasets from different sources have to be compared. Here, two datasets from the same source are used. However the laser scanner has been dismantled and re-installed between the two campaigns. Therefore, the two datasets cannot be compared strictly, but given we are interested on surface features which are moving on the surface, the lack of georeferencing is not a problem. Moreover, only the scans from the same winter season are compared between

each other to derived snow height difference. The laser scans are automatically leveled thanks to a dual axis compensator (inclinometer) which corrects both vertical and horizontal angle measurements. To each point, an altitude value is assigned via an electronic barometer, and an electronic compass provides the scan orientation.

Some aspects of the scanner setup may induce errors or loss of information which are described below. In fact, this set up has the advantage to produce surface scans automatically, however, as the laser scanner is fixed, a small shadow zone may potentially be not measured by the scanner in a case of high incident angle. So the scanned surface may differ slightly from reality. To solve this issue, another laser scanner would be needed to capture the surface from another side. Given the methods applied to the point cloud, this issues seems unproblematic for the results, an issue that is discussed in Section 3.2.

The recommended internal operating temperatures for the laser scanner are between 5°C to 40°C, with operating limits between -20°C and 60°C of ambient air temperature. In our case the temperature can reach -20°C or slightly lower with windchill effect, and approaching these limits may have an impact on the measurement accuracy which is not quantified by the manufacturer. When the lower temperature limit is exceeded the scanner is automatically shut down to avoid damages, which happened sometimes during very cold weather conditions. To prevent the scanner shutdown, sometimes scans were done more frequently because scanning generates internal heat and can prevent cooling. In case the scanner shuts down, it is necessary to heat the scanner to raise the temperature, or to wait for the solar radiation to raise the scanner temperature.

Moreover, the scanner was installed with an inclination of about 60° from a vertical position to be directed towards the snow surface (see Fig. A.6). However the accuracy of the dual axis compensator (inclinometer) is specified for inclinations up to 5° and will degrade above 5° according to the manufacturer. If the scanner is inclined at more than 5°, it may have reduce the accuracy of the dual axis compensator.

Furthermore, according to the manufacturer, snowfall, rain or fog may lead to bad measurements and scanning should be avoided under these conditions. The major problem in our case is falling or drifting snow, because the scanner is operated in any weather conditions so the snowflakes may obstruct the field of view of the scanner and the snowflakes are scanned instead of others points on the surface. Under snowfall conditions or rain, the laserscans show points above the snow surface because of snowflakes or water droplets, and this induce a lack of points on the surface. The difficulty lies mainly in the post-processing of the scans performed during precipitation events, because these points need to be automatically removed for all scans to keep only the information of the snow surface. This process is explained in Section 3.1.3. The scanning performance is evaluated and presented in Section 4.1.2.

If the surface is directly illuminated by bright sunshine, this may increase noise, which is however not quantified by Faro. Scanning against direct sunlight may result in limited scan data in this area according to Faro, which is observed in our case. A comparison between a scan during the day (Fig. 2.6(a)) and the night (Fig. 2.6(b)) shows that a larger snow surface is captured by the scanner during the night, namely without solar radiation than during the day at noon when the solar radiation is maximum. The day of comparison (2021-02-26) was chosen to be a sunny day to see the effect of solar radiation. During the night the point cloud has about 60 million points, whereas during the day it has only about 45 million points. The area which is not scanned during the day corresponds also to an area where the incident angle is high, and given the scanner orientation the probability to interfere with sunlight is higher. However, only a certain area of the scan is kept for the post-processing, so the reduction of the scanned area due to solar irradiance is not a problem. We are more interested in the point densities which remain constant.

A test conducted for the same day, by comparing two scans close in time at noon and midnight led to a distance accuracy of 1 mm at midnight and 2.5 mm at noon, however, given that values are in or very close to the ranging error, we can not ultimately conclude that the distance accuracy is significantly affected by solar radiation. The possible errors sunlight-induced are not quantified here, however it would be interesting to investigate this in

more detail in future work. Nevertheless, it is assumed that the errors induced by the sunlight remain small and that the data acquired do not differ significantly from reality.

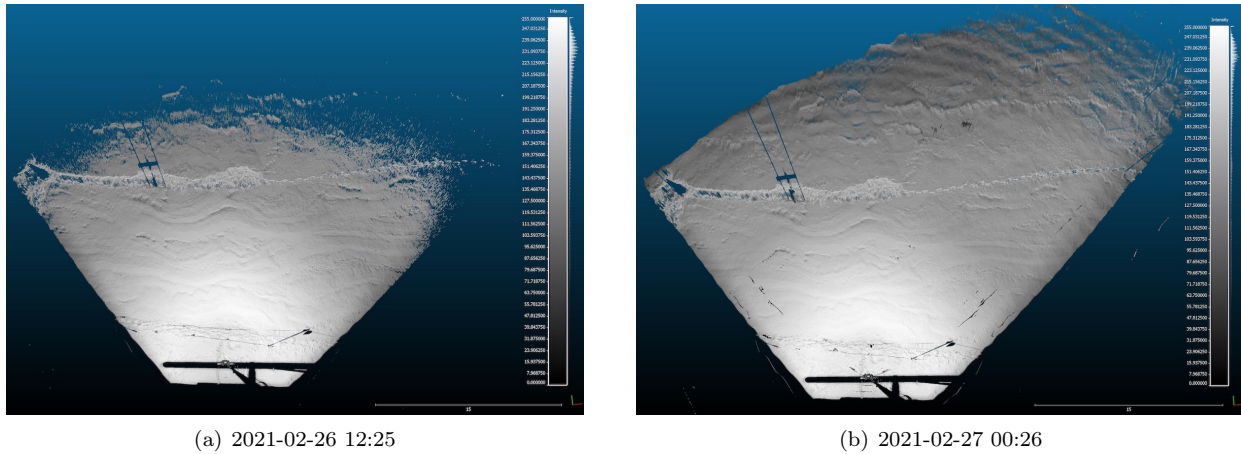


Figure 2.6: Comparison of the scanned area between the day and the night. The scalar field plotted is the reflectance (intensity) in grey scale.

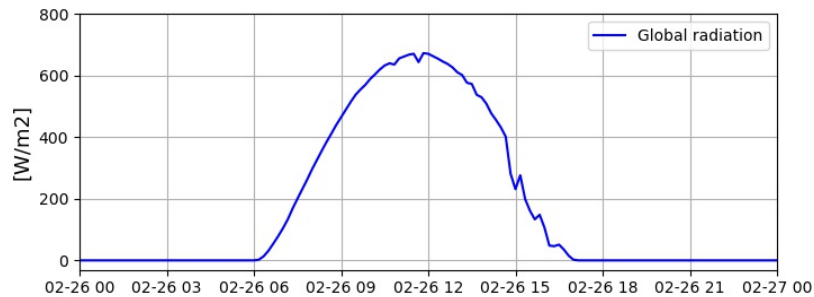


Figure 2.7: Solar radiation from 2021-02-26 00:00 to 2021-02-27 00:00

2.2.2 Sonic anemometer

A sonic anemometer has been installed in the scanned area for the second campaign. The goal is to measure the three-dimensional wind speed close to the snow surface and to derive the aerodynamic roughness length from the covariance term. The sonic anemometer uses ultrasonic sound waves to determine instantaneous wind speed by measuring how many sound waves traveling between a pair of transducers are speed up or slowed down by the effect of the wind, but it doesn't need wind energy (inertial force) for measurements as there are no moving parts and the wind velocity from "zero" m/s can be measured. It was developed in the 1970s (Nfaoui, 2012). It can take measurements at a high temporal resolution such as 20 Hz or even higher frequencies, thus it is well suited for turbulence measurements. Moreover, as there are no movables parts, it has an excellent environmental resistance, and accurate measurements can be conducted for long periods.

The sonic anemometer used is the Model DA-700 from Sonic Corporation, with a TR-90AH probe and a CA-75 model converter. A schema of this setup is presented in Fig. 2.8. It has measurement frequency of 20Hz, so it does 20 measurements per second or one measurement for each 0.05 s. The maximum measurable wind speed is 20 m/s and it has a resolution of 0.005 m/s. To calculate the wind speed, this anemometer uses the ultrasonic propagation reciprocal difference method which doesn't need a term of temperature.

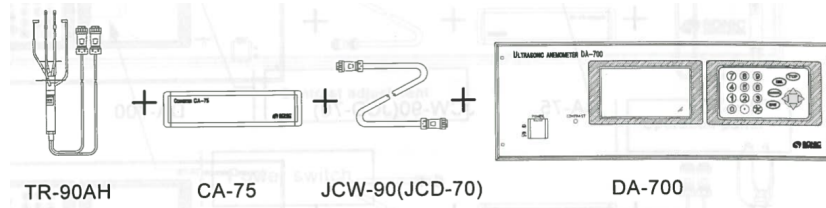


Figure 2.8: Schema of the probe and the computing units (source: Sonic Corporation)

The TH-90AH is a three-directional probe and is limited to a predominant wind direction at $\pm 45^\circ$. It has a measurement axis span of 5 cm and a schema of the probe is presented in Fig. A.7. It is mainly used for wind tunnels, indoor air currents, turbulence observation, or agricultural weather measurements for instance. The probe is adapted for our purpose, which is turbulence observation in an outdoor environment. Nevertheless, the probe is a simple drip-proof structure, and it should not be used outside in case of precipitation. Moreover, it has no heating system so frost can be formed on the probe heads. However, during precipitation events the probe was used but the data got discarded. If the probe was covered with frost after a precipitation event, it was cleaned so that the data could be used afterwards.

The sonic anemometer has been installed in the scanned area to capture the wind turbulence implied by the snow surface roughness. Therefore, the wind must first cross the study area, where the roughness is captured by the scanner, and then reaches the sonic anemometer. The location of the anemometer in the study area has been chosen as stated above by taking into account the main wind direction. The wind rose (Fig. 2.9) shows that the wind comes mainly from North-West on the site. We therefore decided to installed the sonic anemometer in the South-East part on the scanned area (Fig. A.8 and A.4). Ideally, it should be mounted as close as possible to the area used for the calculation of the snow surface roughness, however, it was not possible to installed it closer to the area because of a too short cable between the computing unit and the converter. Nevertheless, the area of influence for the main wind direction shows similar surface features as the area used for calculation.

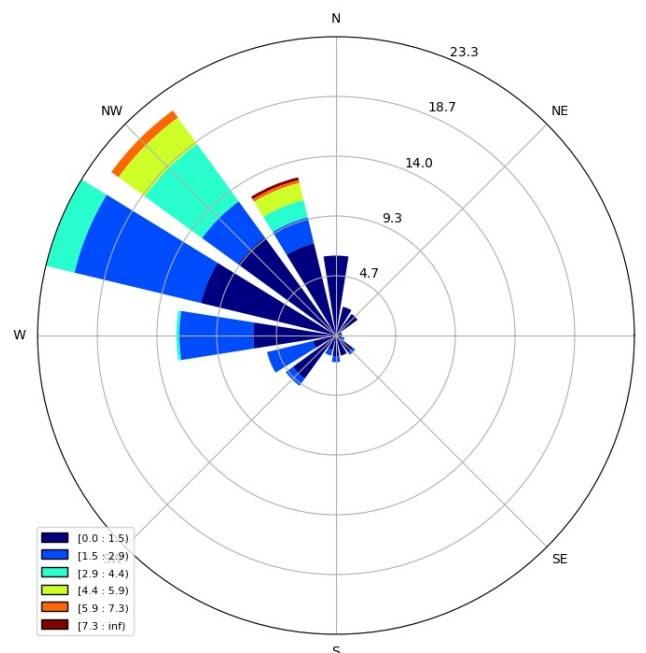


Figure 2.9: Wind rose at the WFJ field site the winter season of the first campaign

The probe was installed on a metal stick that was stuck in the snow (see Fig. 2.10), and was turned to NW. The CA-75 model converter was placed in a waterproof box buried in the snow at about 1 m away from the stick (see Fig. A.8). A 20 m cable was buried in the snow to connect the converter to the computing unit DA-700 which was installed inside the long hut and plugged to the power. A Campbell scientific CR1000 was used as a data logger, with a CFM100 to store the data logger's data on a removable CompactFlash (CF) card which was powered by a 12V battery. This setup allowed to pick up the data during field visits, to process them and to have enough storage on the card.



Figure 2.10: The sonic anemometer installed in the field

2.3 Data acquisition

In this section, the laser scans acquired in the field with the scanner, the wind measurements acquired with the sonic anemometer, and the meteorological data extracted from the WFJ field site, are described below.

2.3.1 Laser scanner

The data from the laser scanner was collected during two measurements campaigns. The scanner was first installed in early February 2021. The first campaign includes data from February 11, 2021, to June 21, 2021. However, there are data gaps because of technical issues with the laser scanner. The scanner shut down a few times due to low temperatures or other technical (hardware and software) issues that were solved over time. Sometimes it was not possible to go on site as soon as the device stopped working. The scanner was dismantled during the summer and it has been sent to the manufacturer for maintenance, repair and calibration. Afterwards, the scanner has been installed again at the end of October 2021, and a second campaign was conducted starting from October 28, 2021 and the measurements are still in progress, and will be done until June 2022.

Table 2.1: Number of scans performed per month

	Number of scans per month
Campaign 1	
February 2021	217
March 2021	575
April 2021	302
May 2021	256
June 2021	176
Campaign 2	
October 2021	38
November 2021	543
December 2021	662
January 2022	693
February 2022	551

The number of scans performed per month is summarized in Table 2.1 for the two measurements campaigns. In total, 1526 have been performed during the first campaign and 2487 during the second one taking into account a period until the end of February 2022. The data used in this thesis are however limited to the scans of February, March, April, and June 2021, and January, February 2022, the reasons are explained below in Section 3.1.

2.3.2 Sonic anemometer

The sonic anemometer was installed on January 13, 2022. The probe and the converter have been dismantled a first time on January 20 before a precipitation event to prevent possible damages, they were installed again on January 24 and dismantled a second time on January 27. The setup was installed again on February 2 and it has not been uninstalled since. The different periods of data collection are summarized in Table 2.2.

Table 2.2: Data collection with the sonic anemometer

	Installation	Disassembly	Probe height
Collect 1	13/01/2022	20/01/2022	45 cm
Collect 2	24/01/2022	27/01/2022	32 cm
Collect 3	03/02/2022	-	32 cm

2.3.3 Meteorological and snow data

The meteorological data and the snow data from the WFJ field site station are available online from SLF on <https://measurements.slf.ch>, for the data of air temperature (TA), snow surface temperature (TSS), snow height (HS), new snow (HN), wind speed (VW), wind direction (DW), relative humidity (RH). The precipitation and solar radiation data are available from MeteoSwiss on the IDAweb data portal <https://gate.meteoswiss.ch>. All data was measured continuously at a resolution of 10 min during two measurements periods of the laser scanner.

3 Methods

The following Section describes how the scanner data is prepared for the z_0 calculations, from the raw point clouds of the snow surface to the detrended DEMs. Moreover, the different models used to calculate the aerodynamic roughness length from the DEMs are presented, including the raster and the transect methods. In addition, the methods used to process the sonic anemometer data are described.

3.1 Preprocessing of the laser scanner data

3.1.1 Raw data

The raw data from the laser scanner is saved on a hard drive connected to a computer in the field, and the scans are regularly uploaded online on a server. From there, they can be downloaded and processed. FARO scanners produce a proprietary format called FARO Laser Scan with the extension .FLS, containing the raw point cloud data. The manufacturer is selling a software to process the point clouds, which is called SCENE. However, the open source software Cloud Compare developed by Daniel Girardeau-Montaut (CloudCompare, 2022), which allows as well to read and process .FLS files (on Windows computer only) is used. In this master thesis only open source software is used.

The raw data is about 400 MB for one scan, resulting in a total of approximately 1.5 TB per season. The point clouds contain between 47 and 60 million points depending on solar radiation and snowfall. A raw scan is illustrated in Fig. 3.1 where the plotted scalar field corresponds to the reflectance (also called intensity) in grey scale. The view is from the top and perpendicular to the surface, the laser scanner is located at the bottom. Close to the laser scanner, the rope with the flags is visible (in grey) with a metal stick. Also the shadow on the snow surface produced by the rope with the flags is visible which doesn't contain points and is colored in black/dark blue. The scanner has been setup so that the scanned area is inside the limited area framed by the wood sticks and the rope. The scanned area is about 300 m^2 . The raw data contains zones where the surface is not well captured because of obstacles, snowflakes or rain droplets, or because of low point densities due to high incident angles for instance.

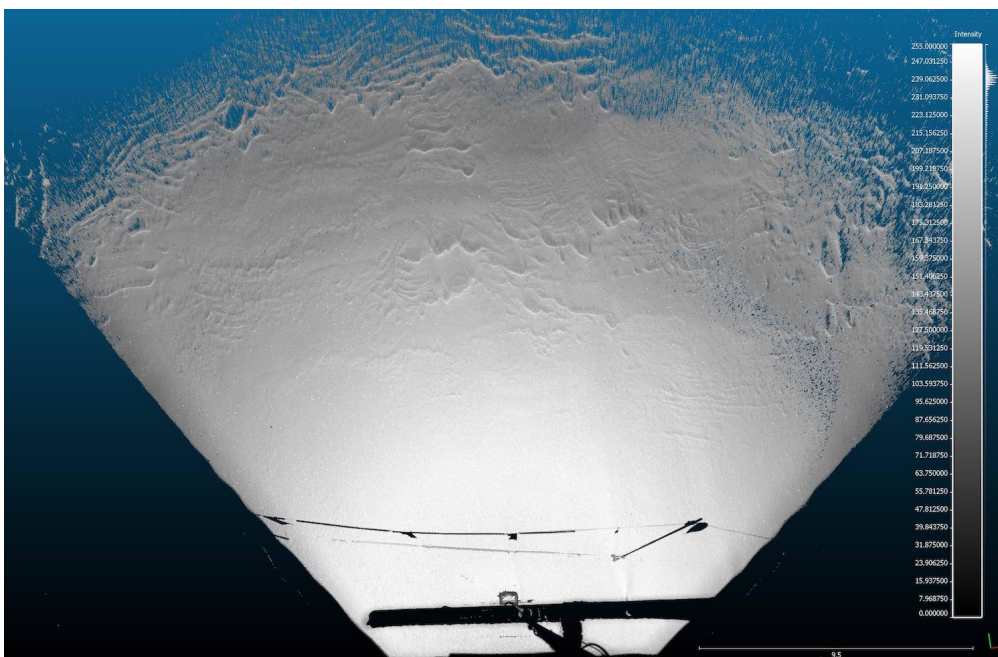


Figure 3.1: Raw laser scan on 2021-02-11 14:32 (CloudCompare)

3.1.2 Segmentation

The raw data needs to be segmented to keep a snow surface that is not influenced by obstacles such as the rope and the flags in front of the laser scanner and the metal stick. Moreover, there were sometimes footprints below the rope because this zone allows crossing between the long hut and the small hut, and also to access to the laser scanner. To process the data easily with Python, a rectangular area is defined and a rectangular polyline is used to segment the scans. The polyline is visible in green in Fig. 3.2 and is placed in order to capture the largest possible area, excluding the influence of obstacles or a low point cloud density at distances far from the scanner. Furthermore, when the incident angle increases, the point density decrease, and to keep the spatial resolution relatively constant, the most distant area from the scanner are removed. Between February 25, 2021 and April 15, 2021, a Snow Particle Counter was installed in the scanned area, in the left upper corner (see Fig. A.2), so the segmentation allows to exclude it. The segmented area obtained is about 20m x 9m and is illustrated in Fig. 3.3.

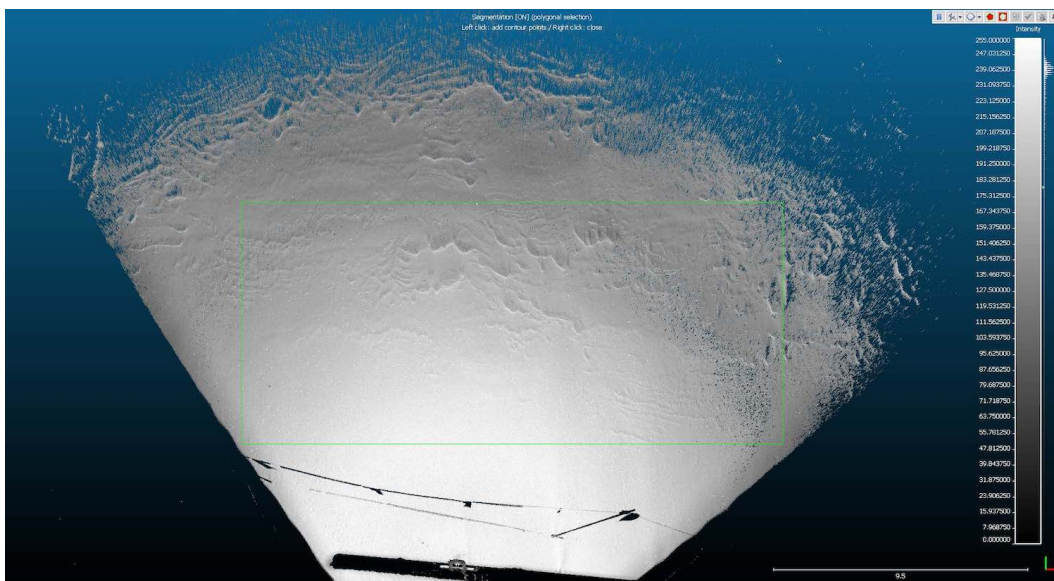


Figure 3.2: Raw laser scan with a polyline on 2021-02-11 14:32 (CloudCompare)

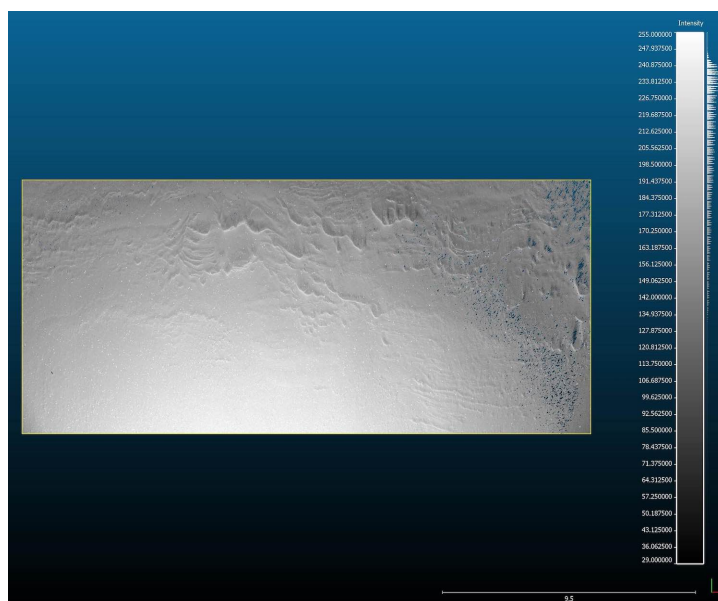


Figure 3.3: Segmented laser scan on 2021-02-11 14:32 (CloudCompare)

The segmentation process can be done only by loading manually the scans in CloudCompare. The scans are performed and loaded in the same coordinate system, thanks to the inclinometer, the altimeter, and the compass. The altimeter is an electronic barometer and the measured altitude depends on the atmospheric pressure as the result of atmospheric pressure variations. It is observed that the scanner height is varying between about 2350 m and 2750 m, whereas the real height on the scanner is about 2541 m. The scanner height can be adjusted but it has to be done manually for each scan, which could not be done here for time reason. The shift in height implies a shift on the z axis, however, if the scans are projected on the x-y plane they are at the same location. When the polyline is defined, the z axis is set as vertical and it allows to segment several scans at the same time and the same area on the scans. The computer used allowed to load and process about 10 scans at the same time. The computer has the following characteristics: Intel Core i9 processor 2.80 GHz and 48 GB of RAM with Windows 10. This manual process was very time consuming for the large number of scans, a computer with better performance would allow to do this process faster, or perhaps the software SCENE facilitates this operation.

The scans performed at the end of April 2021, May 2021 and from November 2021 to the beginning of February 2022 were done without the use of the inclinometer, because there was an error with the inclinometer and it has been turned off. Consequently, the scans were not leveled properly and in the same way, and the change in height between the scans has implied a shift in the y-direction. The only way to process these scans was to do the segmentation manually for each of them, and after to level each scan so that the z axis is perpendicular to best fitted plane to the segmented area. This process was very time consuming, the scans of January and February 2022 were processed in priority, because it corresponds to the sonic anemometer campaign, and the data were necessary to do comparisons. Due to time constraints, all the scans where the inclinometer was turned off had not been processed in this thesis, however they will be processed in a future work.

3.1.3 Cloth simulation filter

During snowfall events, the snowflakes are captured by the laser scanner and therefore there are some points on the scans which do not correspond to the snow surface. It can be caused as well by a random noise from the scanner because some points are captured below the snow surface for instance which is illustrated by the red points in Fig. 3.5. It is necessary to separate the points belonging to the surface to the erroneous ones. For this purpose, the CSF (Cloth Simulation Filter) plugin is used in CloudCompare. It uses a data filtering method based on cloth simulation (Weil, 1986). It's a new filtering method developed by Zhang et al. (2016) which required only a few easy-to-set parameters. The point cloud is inverted and a rigid cloth is used to cover the inverted surface (see Fig. 3.4). The interaction between the cloth nodes and the corresponding points are analysed, and the locations of the cloth nodes can be determined to generate an approximation of the ground surface. The ground points are extracted by comparing the original point cloud to the generated surface. In Fig. 3.4 the goal is keep only the bare surface, so the process remove the house and tree points.

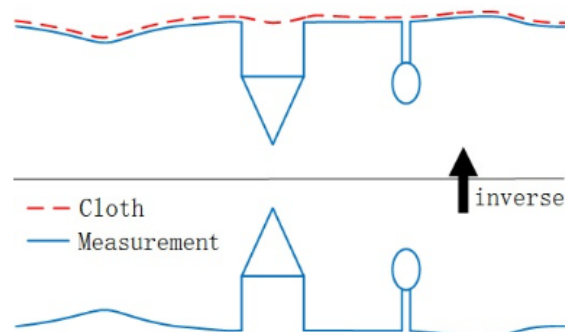


Figure 3.4: Overview of the cloth simulation algorithm (Zhang et al., 2016)

Different settings can be chosen by using the CSF plugin. The first one regards the type of the scanned surface, three types are purposed (steep slope, relief, and flat) which will determine the rigidness of the cloth on the inverted surface. Then, there is the cloth resolution which is the grid size [m] of the cloth used to cover the terrain. The bigger the cloth resolution, the coarser the DEM. Finally, the classification threshold [m] allows to classify the point clouds into ground and non-ground parts based on the distances between points and the simulated terrain. After several tests, the ultimately scene type used is "flat" with a cloth resolution and classification threshold of 0.3 m. This step can be critical, because if there are points left above the surface then they can bias the interpolation and the model calculation later.

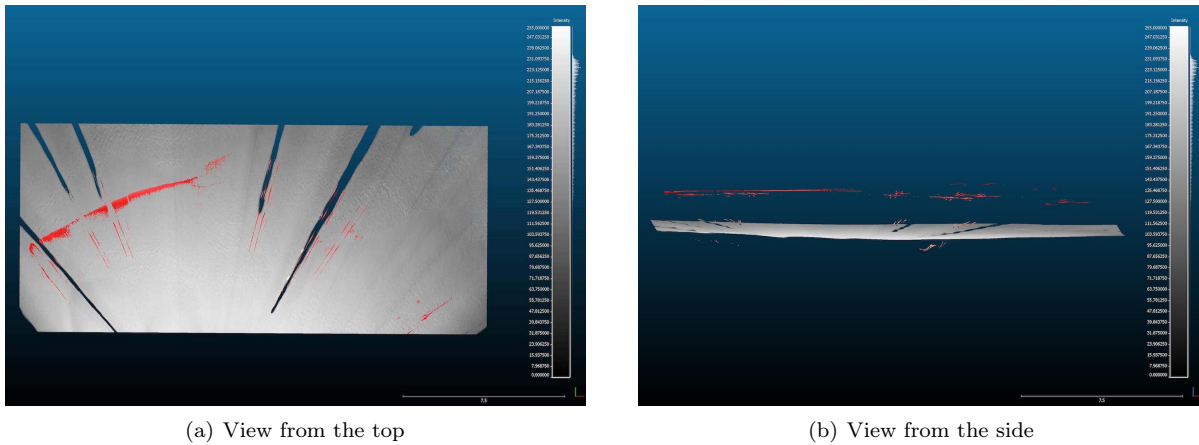


Figure 3.5: Noise to be removed with the CSF filter, during a snowfall event for a scan on 2021-03-16 23:27

3.1.4 Point cloud interpolation

Afterward, the point clouds are interpolated in regular grids with the altitude value. The nearest-neighbor method is used, and the cell size of the grid is defined to 5 mm to have one point per cell at least. Thus digital elevation models (DEMs) are obtained of which an example is presented in Fig. 3.6.

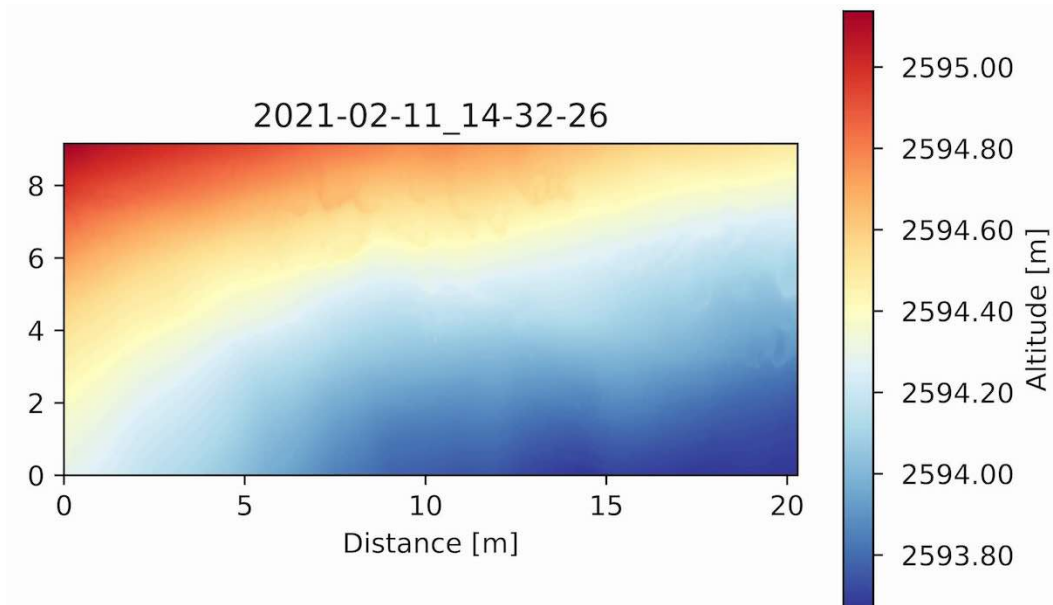
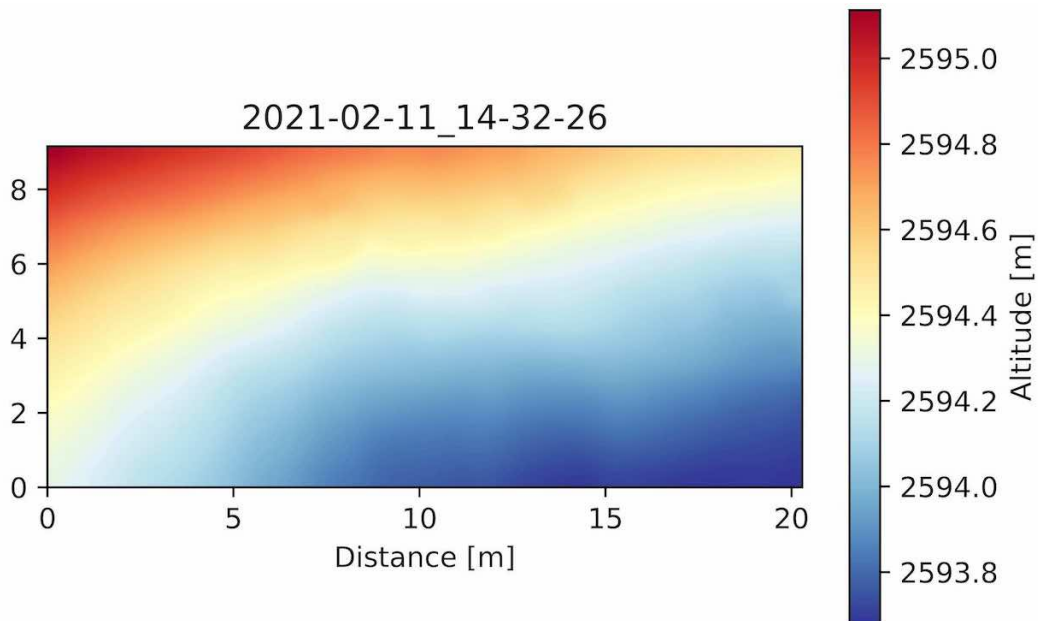


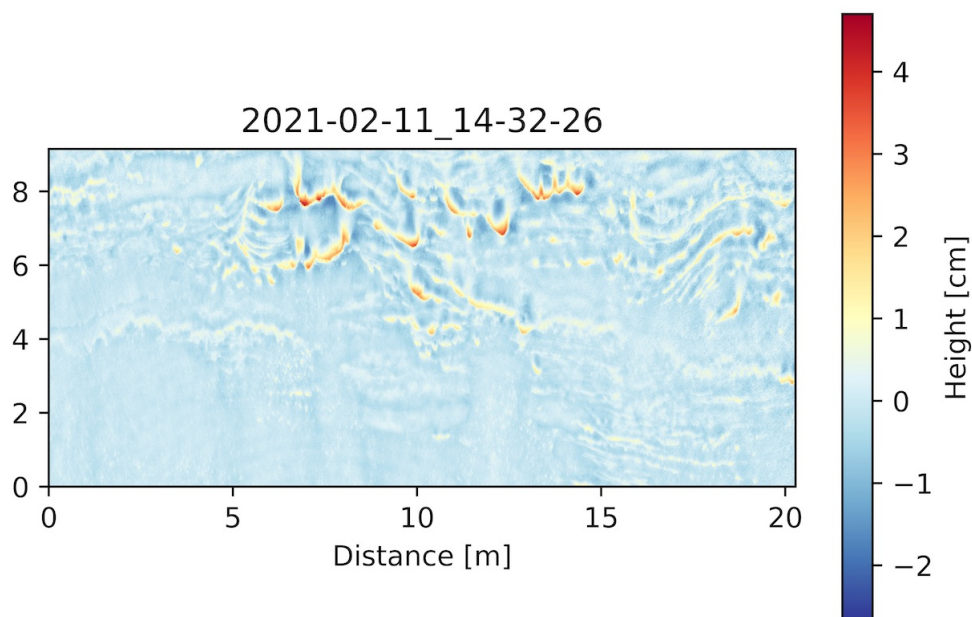
Figure 3.6: Raster obtained after the point cloud interpolation with the altitude value, for a scan on 2021-02-11 14:32

3.1.5 Digital elevation model detrending

The DEMs show the topographic variability at a large scale on the scanned area. However, we are interested in capturing the surface roughness which is a topographic variability at a smaller scale. For this purpose, a low-pass filter is applied to the DEMs to obtain the topography at a large scale (see Fig. 3.7(a)). Several filters are considered to get the trend: a convolution filter with i) a Gaussian or ii) an average kernel, iii) a bilateral filter and iv) a guided filter. Afterwards the trend is subtracted from the original DEMs and the small scale variations are obtained (Fig. 3.7(b)). A sensitivity analysis and an experiment were carried out to highlight the influence of the window size of the low-pass filter on the result and which range of window size should be chosen. The results are presented in Section 4.1.4



(a) DEM with altitude trend



(b) DEM detrended

Figure 3.7: Detrending process for the scan on 2021-02-11 14:32

3.2 Microtopographic z_0 derivation

The aerodynamic roughness length is calculated for each DEM after detrending the data. The most common models to calculate z_0 from topographic data, on glaciers and snow surfaces (Quincey et al., 2017), are based on the work of Lettau (1969), where the following equation for the bulk aerodynamic roughness length has been developed:

$$z_0 = c_d h^* \frac{s}{S}, \quad (3.1)$$

where h^* is the effective obstacle height [m], s is the silhouette or frontal area of the obstacle [m^2], S is the horizontal ground area [m^2], and c_d corresponds to the average drag coefficient of a characteristic roughness element, the value $c_d = 0.5$ has been proposed by Lettau (1969). c_d is defined as the ratio of wind kinetic energy to surface stress, it considers the change in effective drag by individual roughness elements which increase relative sheltering. The value of 0.5 is widely used, especially in glaciology.

The original equation (Eq. 3.1) has been adjusted and further developed in a few studies leading to several methods to estimate z_0 . Moreover, Nield et al. (2013) developed empirical relations between surface roughness metrics and z_0 , which are also considered for the calculation in this thesis.

Different approaches are then used and compared to estimate the aerodynamic roughness length. Afterward, the model with the best performance in comparison with the z_0 value derived from the Sonic data is chosen to process all the data. The models are divided into two groups where different hypotheses are considered. The first one uses the up-crossing frequency (explained below) of the detrended profile on the mean height for each transect (hereafter called up-crossing frequency method) to calculate z_0 . The second one considers all the grid cell heights to derive z_0 . The input data is the detrended DEMs which have the same cell size as the interpolated DEMs, namely a cell size of 5 mm. The methodological steps for z_0 calculation are summarized in Fig. 3.11.

3.2.1 Up-crossing frequency method

The up-crossing frequency method models the roughness elements by counting how many times the detrended profile crosses the mean transect height from below to above as illustrated in Fig. 3.8, it is called the zero-up-crossing frequency (f). This frequency f and the transect length X are taken as input to calculate the frontal area s and the ground area S of Equation 3.1 (Munro, 1989).

This method considers a simple approximation of the roughness elements based on the following assumptions Smith et al. (2016): all roughness elements are of equal height and equally spaced, they do not shelter each other and they are isotropic (same frontal area for the four wind directions). These assumptions are not representative of the reality, however, Munro (1989) found that it gave a good approximation with 12% of difference to the reference values measured with a wind tower.

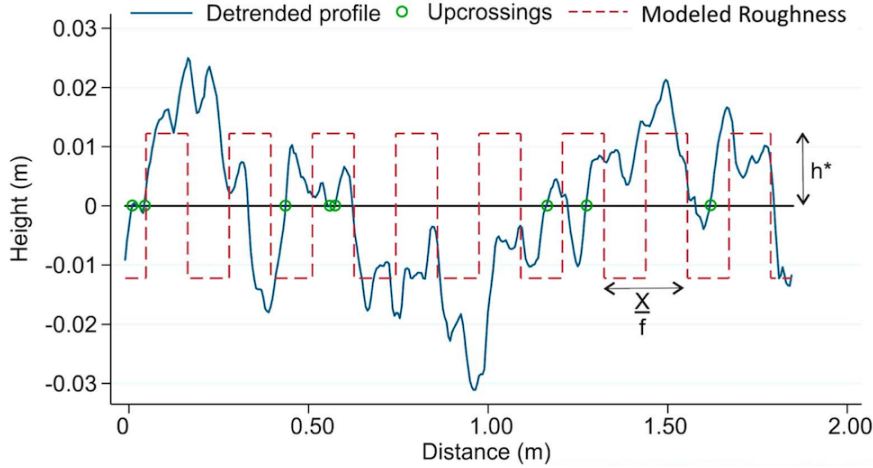


Figure 3.8: Schematic illustration of the up-crossing frequency method modelling the roughness elements (red) the detrended profile (blue) for a transect of length X . The green circle shows the zero-up-crossing from below ($-h^*$) to above (h^*) the mean height of the detrended profile (source: Smith et al. (2016)).

Lettau

In the model of Lettau the height of a roughness element h^* [m] is defined as the average vertical extent of the roughness elements, leading to the following equation:

$$s = \frac{h^* X}{2f}, \quad (3.2)$$

and the aerodynamic roughness length is expressed as follow:

$$z_0 = \frac{f (h^*)^2}{4X} \quad (3.3)$$

One value is calculated for each row or column depending on the wind direction considered, and the final z_0 value for the DEM is taken as the mean.

Munro

The method of Munro (1989) simplified the Equation 3.1 of Lettau (1969). Here the height of a roughness element h^* [m] is twice the standard deviation σ of the detrended transect height. The frontal area s [m^2] and the ground area S [m^2] are then expressed as follow:

$$s = \frac{\sigma X}{f} \quad (3.4)$$

$$S = \left(\frac{X}{f}\right)^2 \quad (3.5)$$

Using Eq. 3.1, the aerodynamic roughness length is:

$$z_0 = \frac{f \sigma^2}{X} \quad (3.6)$$

The final DEM z_0 value is calculated in the same way as with Lettau's model.

Nevertheless, the definition of h^* is not unanimous in the recent studies, some authors adhere to the definition of $h^* = 2\sigma$ (e.g. Irvine-Fynn et al. (2014), Chambers et al. (2020)) and others to h^* as the mean height of all points above the detrended plane (e.g. Smith et al. (2016), Quincey et al. (2017)). The parameters used for the different models are summarized in Fig. 3.9.

The up-crossing frequency method presented in this section takes only the number of up-crossings from the surface roughness, but it does not consider individual heights of the roughness elements. This first type of method may be more appropriate if the data availability is limited or if the computing power is low (Smith et al., 2016). In our case, the data availability is not a problem, but the computing power is an important point given the large number of scans to process. In addition, Rounce et al. (2015) showed that the Lettau model is more suitable for low densities of roughness elements because otherwise aerodynamic interference between roughness elements would impact the value of z_0 . This aspect should be considered to compare the models. The use of another type of method would be then advisable, in particular to fully use the surface roughness input data.

Parameter	Smith	Chambers	Fitzpatrick	Munro	Lettau
Effective obstacle height h^* (m)	Mean height above the detrended plane	$2 \times$ standard deviation of z above detrended plane	Mean height above the detrended plane	$2 \times$ standard deviation of detrended profile	Mean obstacle height
Silhouette area s (m^2)	Frontal area above detrended plane across whole sub-grid calculated for all four wind directions		Frontal area across window above the height of the first row cells calculated for all four wind directions	Frontal area of a modelled roughness element: $h^*X/2f$. With X = transect length, f = transition frequency	
Ground area S (m^2)	Full area of DEM sub-grid		Area of moving window	Ground area of a modelled roughness element: $(X/f)^2$	
Drag coefficient c_d	0.5				
Roughness length z_0 (m)	$z_0 = c_d h^* \frac{s}{S}$				

Figure 3.9: This is an overview of the parameters used for the different models (source: Dachauer et al. (2021))

3.2.2 Raster method

Another method developed more recently, called the "raster method" is presented here. This method is also based on Eq. 3.1 from Lettau (1969). The roughness elements are determined by considering the elevation value of each cell of the grid where the cell size is the same as from the interpolation. The surface roughness is defined as the difference in elevation between two adjacent cells. The frontal area s is calculated as indicated in Fig. 3.10 with the elevation differences for each cardinal wind direction. In order to consider the sheltering effect between close roughness elements, only the frontal areas above the detrended plane are taken into account (Smith et al., 2020).

The advantage of this method is the full use of the surface roughness input data without simplification. The assumptions made for the up-crossing frequency method, that "all roughness elements are of equal height and equally spaced, they do not shelter each other and they are isotropic (same frontal area for the four wind directions)" are not necessary with the raster method because each cell is taken into account for the calculation. Moreover, this method allows to calculate one z_0 value per wind direction, which can allow to detect a wind direction dependency.

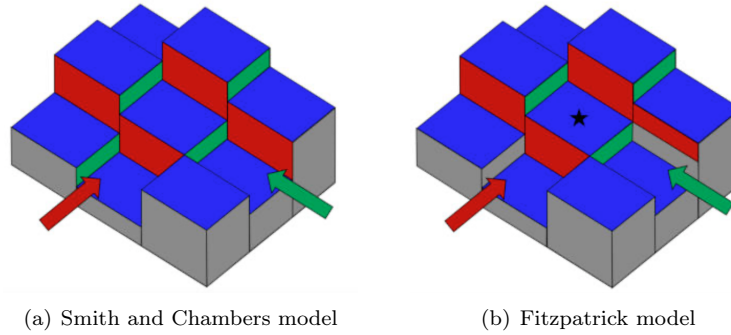


Figure 3.10: Schematic illustration of raster method underlying the frontal area s for two different wind directions: one in red and a second in green, for the model of Smith and Chambers and the one of Fitzpatrick (source: Dachauer (2020)).

Smith

The first raster model is the "DEM-based" approach from Smith et al. (2016). The frontal area s and the obstacle height h^* are calculated for each row or column of the grid. h^* is calculated as the mean elevation of all the cells above the detrended plane. As illustrated in Fig. 3.10(a), the frontal area is for a given wind direction the area visible from a row cell to the next cell in the row if the cell considered has a lower elevation, and in this case the area is calculated as the elevation difference times the cell width. For the whole grid the frontal area value is the sum of the value for each row or column. Note that the sheltering effect of the cells above the detrended plane, namely the cells with a positive value after the detrend processing, are used for the calculation. Smith et al. (2016) assume that the cells below the detrended plane are not affecting the surface roughness. The ground area S is the whole area of the grid. Finally, for each DEM, four different z_0 values are calculated, one for each wind direction.

Chambers

The second raster model comes from Chambers et al. (2020) and is derived from the Smith model. The only difference is related to the definition of h^* , which is here defined as twice the standard deviation of elevations above the detrended plane.

Fitzpatrick

The last model has been developed by Fitzpatrick et al. (2019), it is based on the "Block estimation". Here a moving window on the grid is used to process the data. The moving window goes through the whole grid, from cell to cell, and it calculates one z_0 value for each cell at the center in the moving window by considering the other cells in the window. For a cell to be at the center of the moving window, the window should be an odd number (i.e. one cell at the center plus an even number of cell around the cell considered). Another difference from the previous model is regarding the sheltering effect: the frontal area considered is only the area which is higher than the first window cell for a given direction (see Fig. 3.10(b)).

Fitzpatrick et al. (2019) define the frontal area as:

$$s = \left(\sum_{i=1}^n \max(z_{ij}) - z_{i1} \right) \cdot \text{cellwidth}, \quad (3.7)$$

where i and j refer to the column and row indices respectively in the moving window and n is the number of rows. Fitzpatrick et al. (2019) defined h^* on the same way as Smith et al. (2016), which is the mean elevation above the detrended plane. One z_0 value is then calculated for each cell, and the global value for the whole grid

is taken as the mean. This model has the advantage to consider the adjacent cells from all wind directions for a given cell to calculate its z_0 value, however this approach is computationally more demanding.

Smith et al. (2016) used another approach called "Point Cloud-Based Approach", which uses directly the point cloud to calculate a z_0 value. For each grid point, a normal vector is computed. The silhouette area s is represented by the number of normal vectors facing each cardinal direction (i.e. within a 90° bin centered on the cardinal direction). Points below the detrended plane and "flat" surfaces are defined by a normal vector greater than 80° from horizontal, and are not used in the estimation of s . The plot area S is approximated by the total number of points in the cloud (approximation of the 3D surface area). Finally, the effective obstacle height was calculated as the mean height above the detrended plane of all points above that plane. This approach was not used in this thesis, however, it may be the subject of future investigations based the scanner data.

Empirical relations from Nield et al. (2013)

Nield et al. (2013) combined wind tower measurements with terrestrial laser scanning of small plots (20 plots in total) to develop empirical relationships between z_0 and diverse surface characteristics. We chose three of the best fitted empirical parameterizations which are based on: the standard deviation of obstacle heights h_σ [m] (Eq. 3.8), the mean h_{mean} [m] and the maximum h_{max} [m] of obstacle height (Eq. 3.9 and 3.10 respectively), and on the sill [m^2] of a fitted semivariogram for an elevation profile (Eq. 3.11). Nield et al. (2013) developed other relations but here we use the relations with a single parameter and with $R^2 > 0.7$.

$$\ln(z_0) = 0.29 + 1.33 \cdot \ln(h_\sigma) \quad (3.8)$$

$$\ln(z_0) = -0.28 + 1.33 \cdot \ln(h_{mean}) \quad (3.9)$$

$$\ln(z_0) = -2.02 + 1.50 \cdot \ln(h_{max}) \quad (3.10)$$

$$\ln(z_0) = 0.60 + 0.67 \cdot \ln(s) \quad (3.11)$$

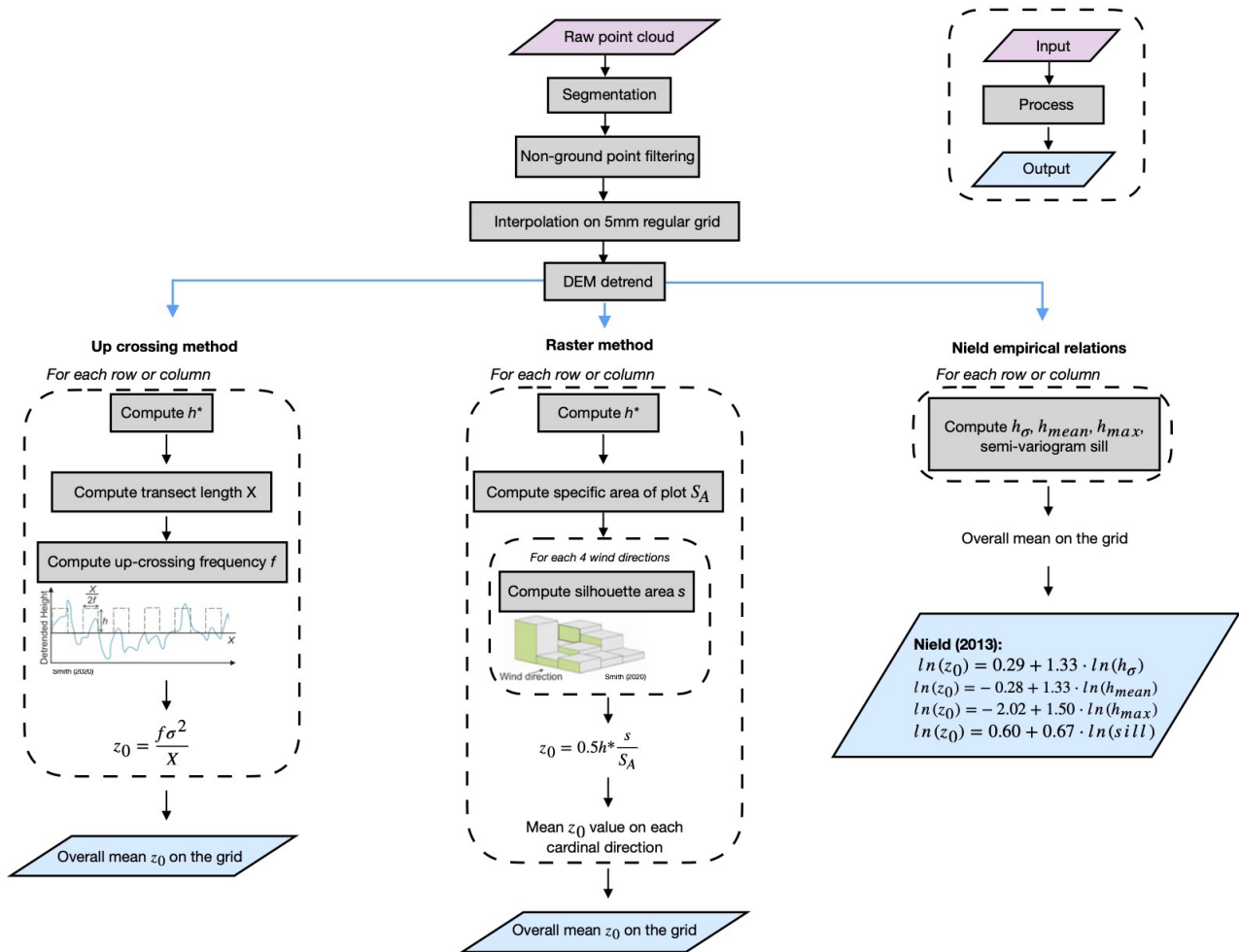


Figure 3.11: Scanner data processing flowchart

3.3 Anemometric z_0 derivation

The aerodynamic roughness length z_0 is further calculated from ultra-sonic anemometer data, which contains the wind speed in three dimensions: u , v , and w are the three wind speed components in x , y , z direction respectively. The processing includes first filtering of extreme values, and a double rotation of the data to have u_y and u_z , such that their mean is zero. Afterwards, the fluctuations are extracted by using the Reynolds decomposition such that the wind speed u is equal to:

$$u(x, y, z, t) = \bar{u}(x, y, z) + u'(x, y, z, t) \quad (3.12)$$

Where \bar{u} denote the wind speed expectation over a certain time period called the Reynolds averaged time, and u' is the fluctuation term. The Reynolds decomposition is illustrated in Fig. 3.12 for one Reynolds averaged time.

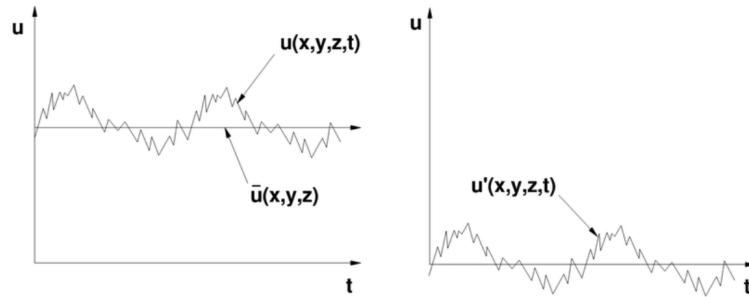


Figure 3.12: Reynolds decomposition for the wind speed u

The friction velocity u_* is determined from the covariance of the fluctuations of the horizontal (u' , v') and vertical (w') wind components such that:

$$u_* = \left[\overline{(u'w')^2} + \overline{(v'w')^2} \right]^{1/4} \quad (3.13)$$

Finally, z_0 is derived for the logarithmic wind profile which is defined as:

$$u(z) = \frac{u_*}{\kappa} \ln \left(\frac{z}{z_0} \right), \quad (3.14)$$

where z denotes the height where the measurements are made, namely the height of the probe, $u(z)$ is the mean wind speed at the height z , a κ is the von Kármán constant which is 0.41 (dimensionless).

4 Results and discussion

4.1 Preprocessing of the laser scanner data

4.1.1 Snow height monitoring

In a first step, the data was used to monitor the evolution of the snow height and to compare it to a reference snow height at the WFJ field site. To monitor the snow height evolution, all the scans over the first campaign with the laser scanner are compared to a reference scan on 2021-02-10 05:32 to get snow height differences. The reference scan was chosen such that its surface is as smooth as possible. The point cloud comparisons were carried out with the segmented point clouds as input, and the plugin M3C2 (Multiscale Model to Model Cloud Comparison (Lague et al., 2013)) in CloudCompare was used to calculate the distance between two point clouds. Then, the average value of snow height difference to the reference scan and the standard deviation are considered. The snow heights with the laser scanner are obtained by using the snow height value from IMIS data for the reference scan. This first processing allows to monitor the snow height evolution on the scanned surface at WFJ field site and serves as a validation of the reliability of the DEMs derived from the laser scanner data. The snow height difference is plotted as a function of time in Fig. 4.1 in blue, and the standard deviation for each comparison is plotted as errors bars in red. The snow height measured at the WFJ field site is plotted in green.

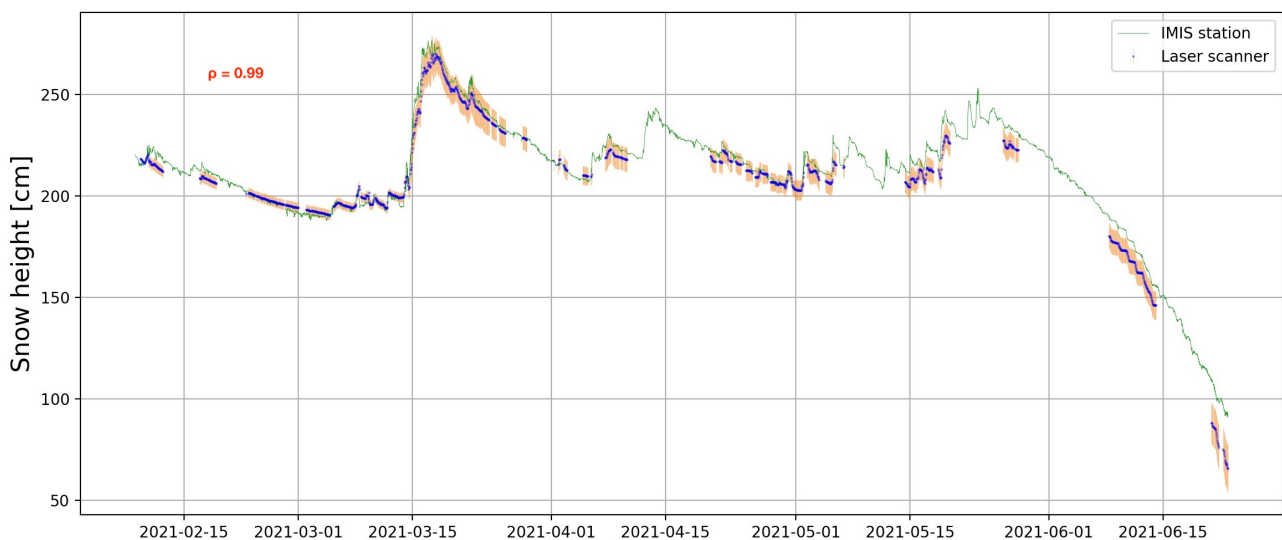


Figure 4.1: Mean of snow height difference [cm] compared to the scan on 2021-02-10 05:32 with error bars, and the IMIS snow height [cm] as a function of time from February 9 to June 21, 2021

The snow height varies at most 80 cm in mid-March after a major snowfall event during the snow season. The melting period starts around the end of May. The standard deviation expresses how much the members of a group differ from the mean value for the group. It indicates the spatial snow height variability in the area, namely how uniform the snow height change is in the area. It was found to be higher during and after a big snowfall event (ca. ± 10 cm), for instance, mid-March or at the end of the snow season in June when the surface roughness is high. The lowest values for the standard deviation were found from February to mid-March when precipitation and wind were low. Note that there are some gaps in the data because of the technical issues with the laser scanner.

The snow height from the scanner is obtained from the mean snow height difference which depends on the reference scan. It is observed that the values and curve shape of the laser scanner snow height are very similar to the ones of the IMIS snow height. The IMIS snow height is measured with a multi-point laser which is located at a different place than the area studied with the laser scanner, and the snow height does not evolve

in the same way at these two locations, that's why the values and shapes are not strictly identical. However, they are very strongly correlated with a Pearson's correlation coefficient of $\rho = 0.99$. Figure 4.2 shows the laser scanner snow height versus the IMIS snow height, the points are close to the 1:1 line on all the snow height range which indicates the strong correlation between both variables. The laser scanner allows to calculate a snow height difference between scans, here a snow height value from the IMIS data is used to convert the snow height differences in snow heights to facilitate understanding, however, this doesn't affect the correlation found between both variables. This first result demonstrates the ability of the laser scanner to monitor the snow height over the whole season. This allows e.g. for detailed snow water equivalent determinations as well as its spatial and temporal variations. The overall good agreement of the mean snow height derived from the scans with the snow height from the station indicates a high accuracy of the scanner.

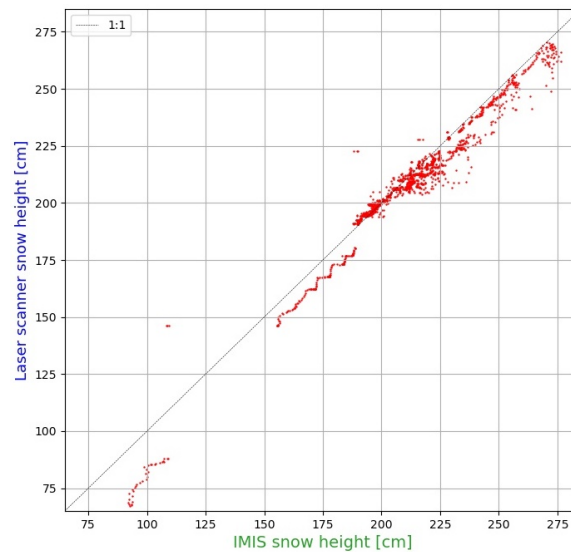


Figure 4.2: Mean of snow height difference [cm] versus the IMIS snow height [cm], with the 1:1 line (black), for the period between February 9 to June 21, 2021.

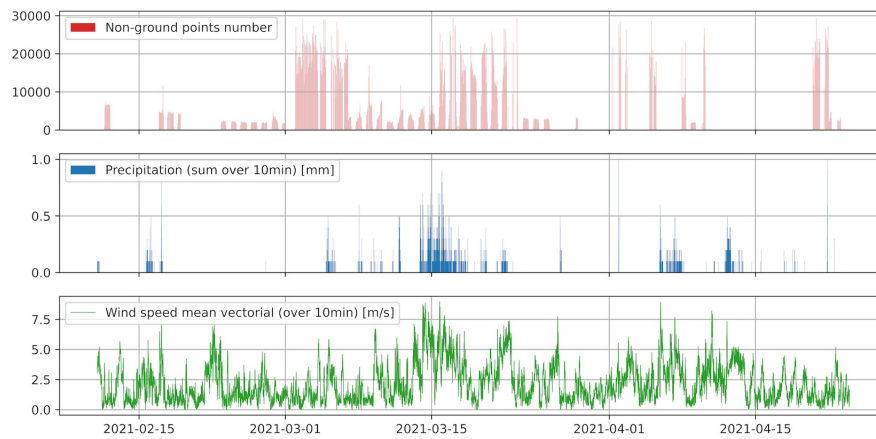
4.1.2 Non-ground points

Non-ground points are present on the point clouds. These points are almost all removed by using the CSF filter described in Section 3.1.3. Nevertheless, about 10% of the scans processed were put aside because they contain points very close to the surface (about 10 cm height) and these points could not be removed with the CSF filter, which leads to extreme values in z_0 calculation. The non-ground points may degrade the snow surface point cloud and the results derived from it. The question is why are these non-ground points still present, and if atmospheric conditions such as precipitation, wind, solar radiation or relative humidity have an influence on the surface point cloud, and if the scan quality is significantly affected.

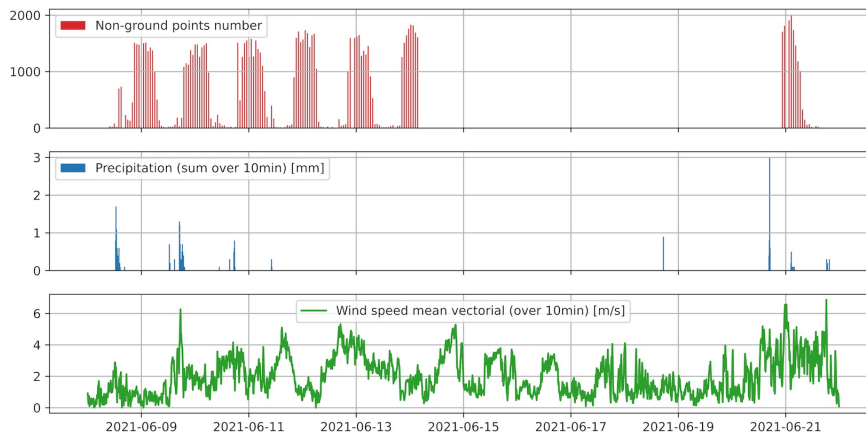
The first variables likely to affect this problem are precipitation with falling snow and wind with blowing snow. Figure 4.3 shows the number of non-ground points, the precipitation, and the wind speed as a function of time. By looking at Fig. 4.3(a)-4.3(c), the number of non-ground points does not seem significantly being linked to precipitation events or to strong wind events.

In fact, the non-ground points number and the precipitation show a correlation close to zero, and the Pearson's correlation coefficients are 0.05, -0.11 and -0.12 respectively for the three periods considered (Fig. 4.4). The correlations are calculated for each of the three-time periods to check that the results are similar, and if not to find an explanation on the period characteristic leading to a result significantly different. The non-ground points number as a function of the precipitation is presented in Fig. 4.4, with linear regression. For the second and the third period, the negative correlation coefficients suggest that an increase in the precipitation implies a lower

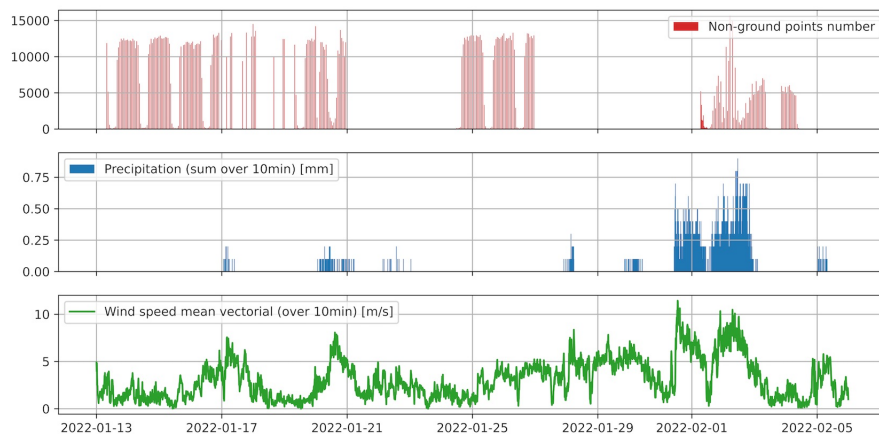
number of non-ground points, which is counter intuitive because the snowflakes or the rain droplets may be scanned and represent non-ground points. Moreover, the wind speed and the non-ground points number show also a very low correlation (see Fig. 4.5), where the correlation coefficients for the three periods are respectively 0.03, -0.18 and -0.13. For the period 3, the negative correlation coefficients is counter intuitive because a high wind speed would tends to a higher number of non-ground points with blowing snow for instance. For period 2 the negative coefficient seems less counter intuitive given the snow type in June. Consequently, the non-ground points number shows a very little or no correlation with precipitation and wind events.



(a) February 11 to April 23, 2021



(b) June 8 to 22, 2021



(c) January 13 to February 5, 2022

Figure 4.3: Non-ground points, precipitation (mean over 10min) and wind speed (mean over 10min) at WFJ field site as a function of time

In Fig. 4.3(b) and Fig. 4.3(c), the number of non-ground points shows diurnal variations: the number is maximum around midnight and minimum around noon. The diurnal variations for the second and the third periods (Fig 4.3(b) and 4.3(c)) seem inversely proportional to the global radiation because the maximum of global radiation is around noon when the number of non-ground points is at its minimum, and inverse for midnight. The correlation coefficient between the global radiation and the non-ground points number is -0.68 and -0.64 for the period 2 and 3, which indicate a relatively strong negative linear dependence between both variables.

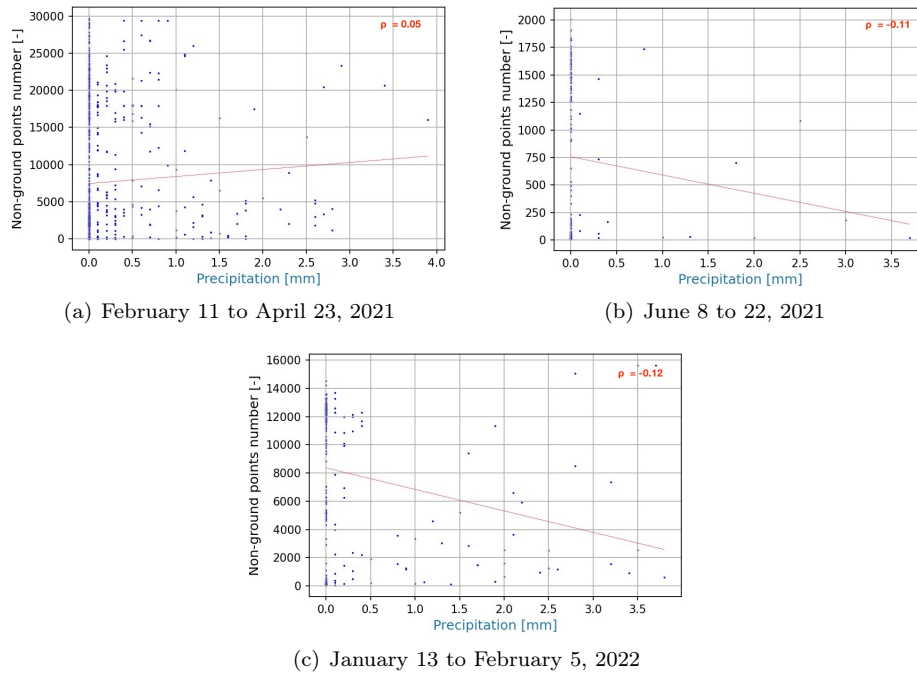


Figure 4.4: Precipitation (sum over 1h) [mm] versus non-ground points number [-]

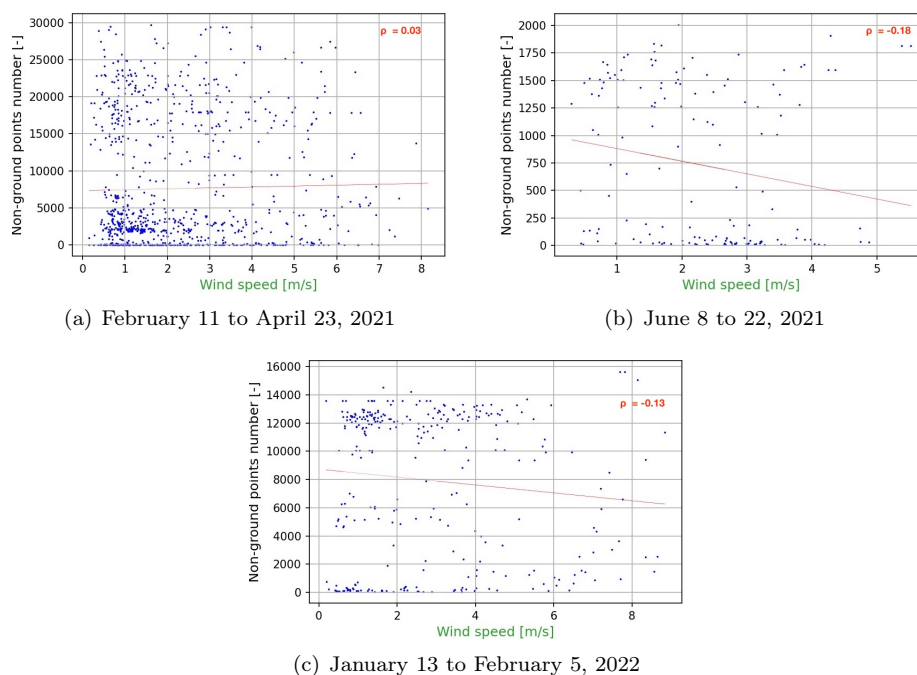


Figure 4.5: Wind speed (mean over 1h) [m/s] versus non-ground points number [-]

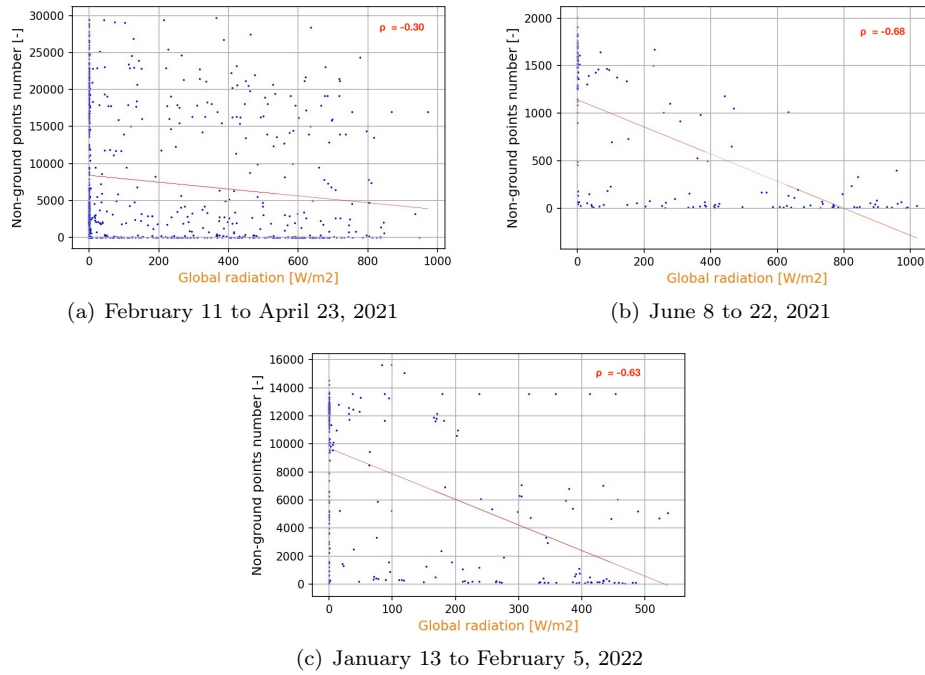


Figure 4.6: Global radiation (mean over 1h) $[W/m^2]$ versus non-ground points number [-]

Nevertheless, a comparison between these three periods is tricky because the first period (February 11 to April 23, 2021) is more than two months with various atmospheric conditions, whereas the third period (January 13 to February 5, 2022) is about two weeks, the second is about one week. A hypothesis is that clouds or snow dust are formed during the night, an indicator to investigate this is the relative humidity. However, the correlation of the non-ground points number with the relative humidity is close to zero, 0.13, 0.06, and -0.17 for the three periods respectively, this hypothesis is then rejected.

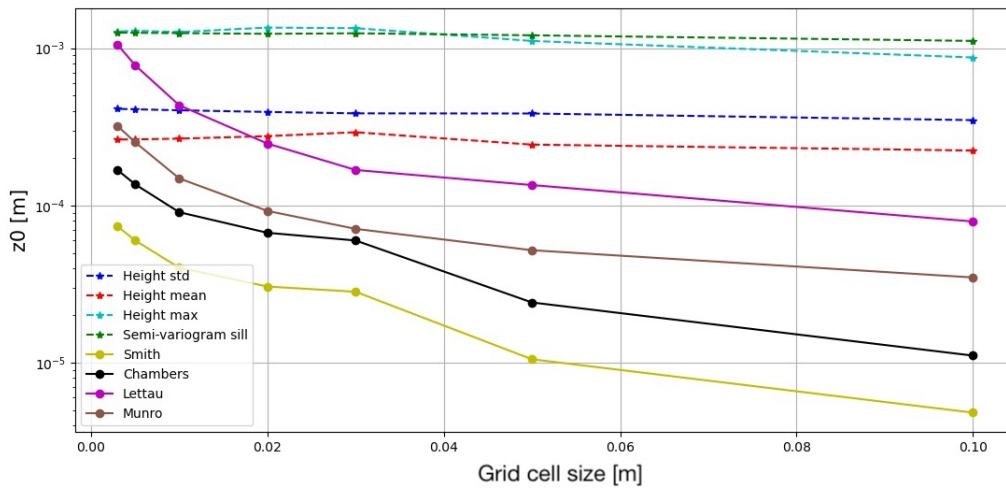
Another hypothesis would be linked to the long wave radiation emitted by the snow surface when the sky is clear. The emission of infrared radiation could interfere with the laser scanner, which operated in near-infrared (905 nm). The correlation of the non-ground points number with the emitted longwave radiation is 0.09, -0.22, and -0.24 for the three periods, respectively. This correlation is low for the period 1, and is moderately negative for the periods 2 and 3. Without strong linear dependency between both it is difficult to validate this hypothesis.

Thus, the origin of the non-ground points is not clearly determined. Some potential causes may be difficult to measure or verify, for instance, these non-ground points could be due to random noise from the scanner. This may become a field of investigation for a future study.

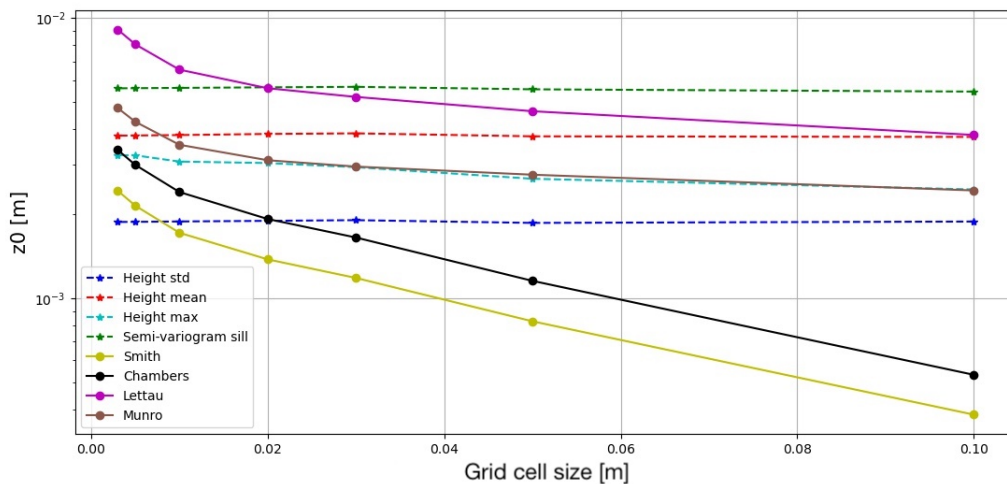
4.1.3 DEM interpolation: cell size sensitivity analysis

The grid size used for the interpolation is 5 mm x 5 mm and which is chosen to be as small as possible to have at least one point per cell, and a DEM with the highest spatial resolution. Based on the previous statement, the choice of a cell size of 5 mm is the most suitable. However, it is observed that the z_0 values calculated change if the cell size changes. A large grid size has a smoothing effect on the surface, whereas a smaller grid size captures more roughness elements leading to a higher frontal area s and a higher z_0 value. Figure 4.7 shows z_0 as a function of the cell size. It appears that for the models based on Lettau's equation, z_0 increases when the cell size decreases. The scan chosen for Fig. 4.7(b) presents a high surface roughness where z_0 is higher for this scan than for the scan studied in Fig. 4.7(a), and the two raster models (Smith and Chambers) show a higher variability on z_0 when the cell size changes. With a lower cell size, the surface is modeled more finely and more roughness elements are taken into account, leading to a higher z_0 in particular with a rough surface. Note that

the models depending on the roughness height and on the semi-variogram sill show very little influence to the cell size.



(a) Scan on 2021-02-17 17:32



(b) Scan on 2021-06-21 04:29

Figure 4.7: Dependency of mean z_0 values to the cell size used for the DEM interpolation, for each models and two different scans

4.1.4 DEM detrending: window size sensitivity analysis

The window size of the low-pass filter affects the height of the snow features obtained after the DEM detrend process. To understand its influence, an experiment was conducted with small snow towers built on the surface at two different locations (see Fig. A.9). Each tower height is known, and they range between about 5 cm and 11.5 cm. The DEM of the scan with the snow towers is detrended with different sizes of the moving window filter (from 3 cm to 120 cm). Figure 4.8 shows the snow tower height on the detrended DEM for the biggest and smallest tower as a function of the moving window filter size. From a window size of 0.6 m, the height of the big tower is about 11.5 cm which corresponds to measured height. The same observation is made for the small tower. Above 0.6 m, the height increase slightly and has a plateau shape. Based on this experiment, a window size of 0.6 m seems appropriated to capture a realistic height, and in order to have also a value as small

as possible to capture the small-scale variations. A large window size has a smoothing effect on the surface, whereas with a smaller window size, the smoothing effect is less pronounced and the variability at a small scale is captured.

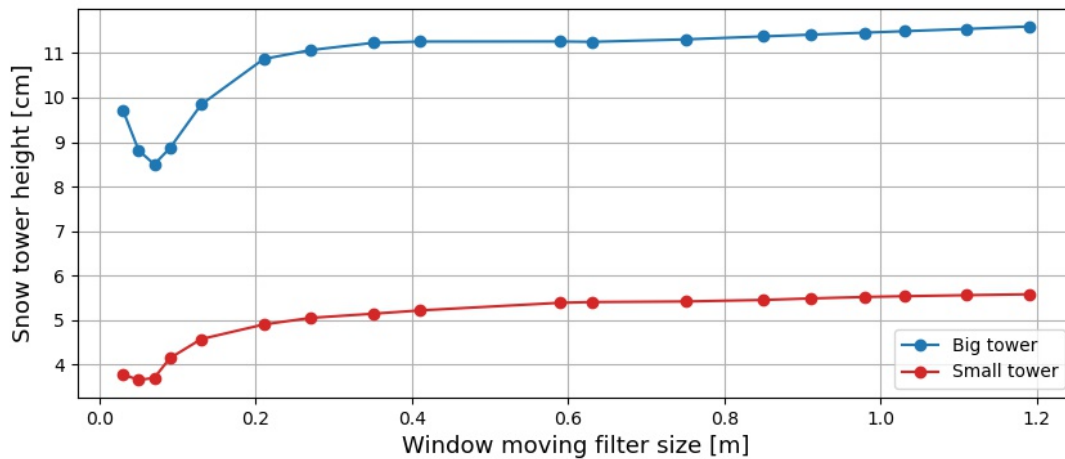
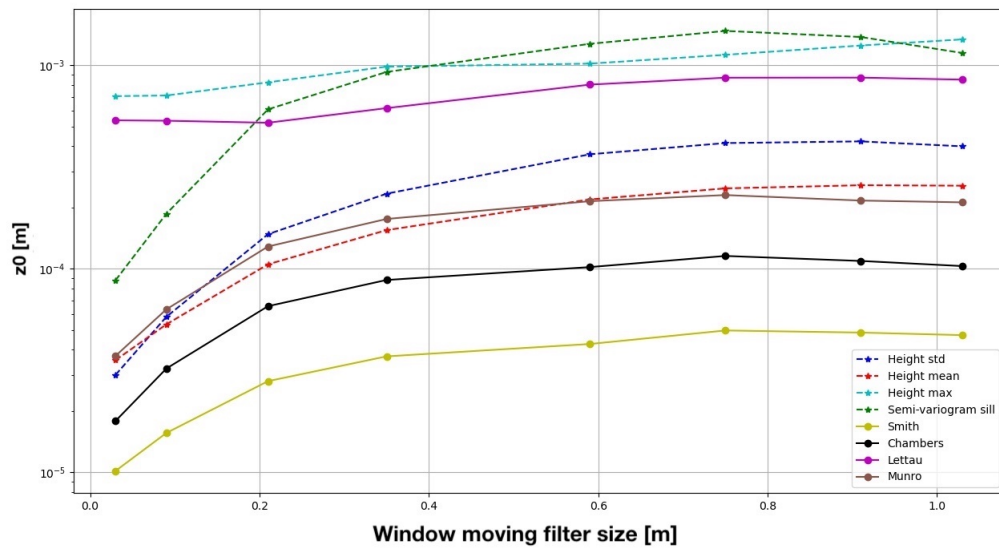
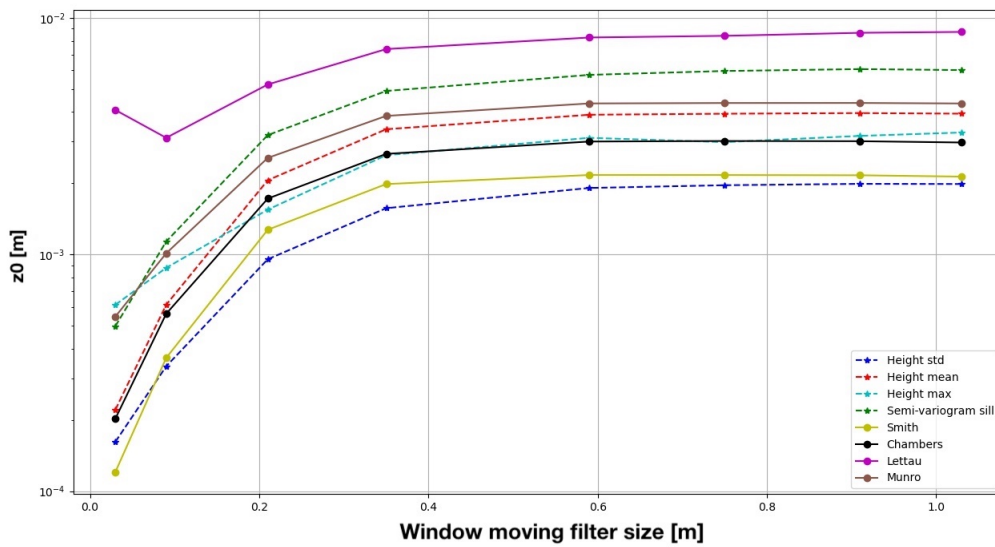


Figure 4.8: Dependency of the calculated snow tower height to the moving window filter size for the detrending process

However, the snow towers built have not the same geometric characteristics as the snow surface features, so a sensitivity analysis of the window size is carried out on z_0 values for the different models. The results are presented in Fig. 4.9 for two scans, a first one on February 17 where the roughness elements are small and non-homogeneous (see Fig. 4.10(a)), and a second on June 21 with high and very homogeneous roughness elements (see Fig. 4.10(b)). For these two types of surfaces, it appears as well that from a window size of 0.6 m the value of z_0 is quite constant.

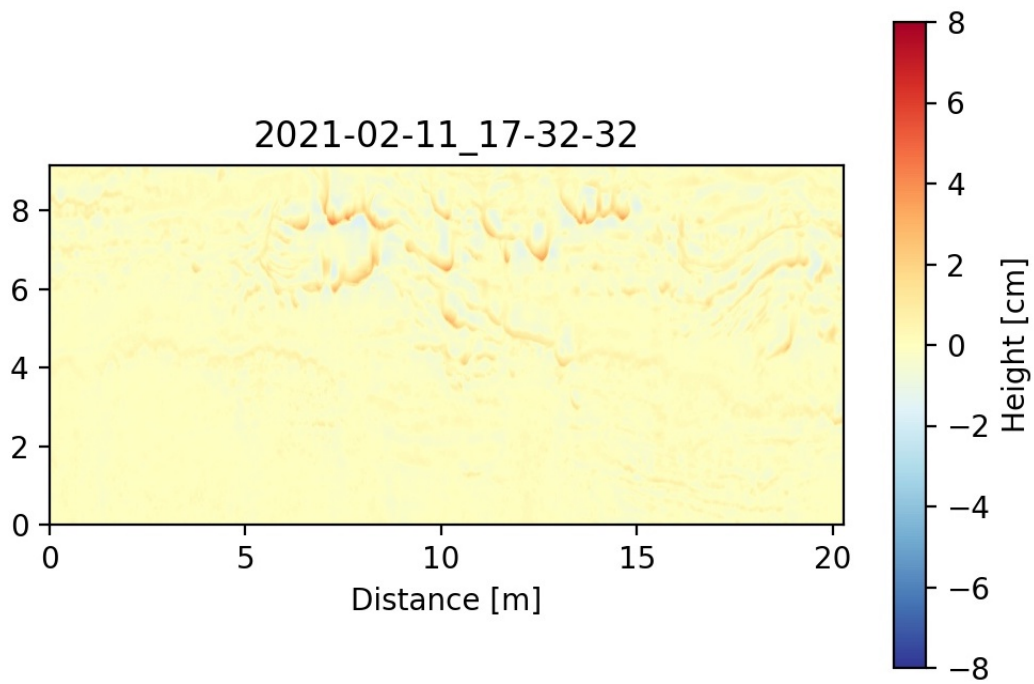


(a) Scan on 2021-02-17 17:32

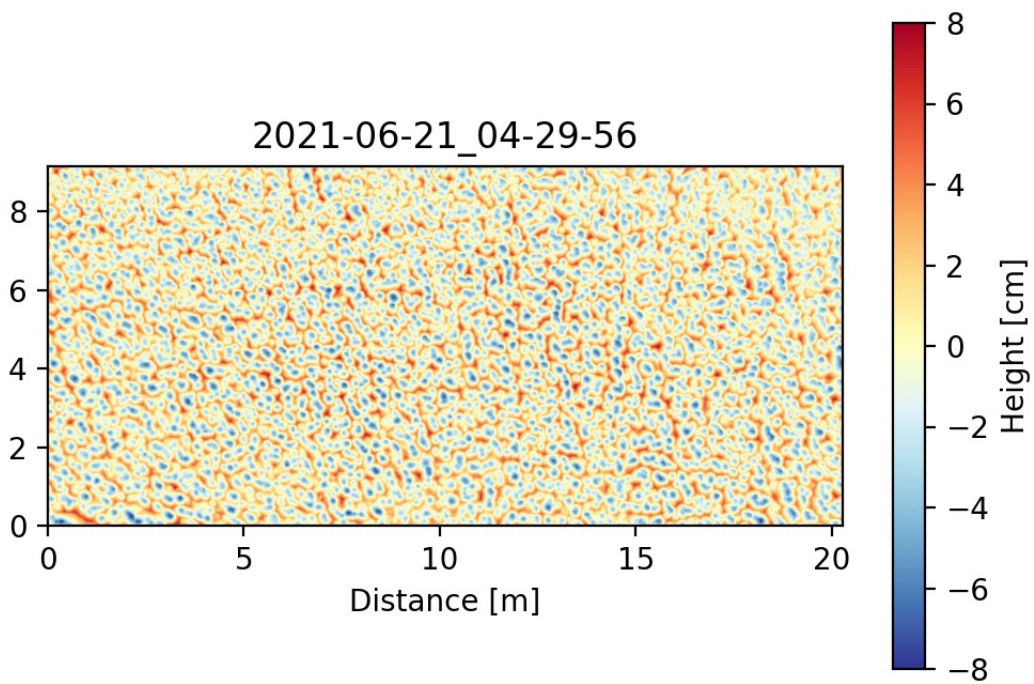


(b) Scan on 2021-06-21 04:29

 Figure 4.9: Dependency of mean z_0 values on the moving window filter size for the detrending process



(a) Scan on 2021-02-17 17:32



(b) Scan on 2021-06-21 04:29

Figure 4.10: Detrended DEMs

4.2 Aerodynamic roughness length z_0

4.2.1 Microtopographic method

First, the different models are compared on a small-time period from 2021-02-16 22:11 to 2021-02-18 10:04. Figure 4.11 presents the z_0 values as a function of time. The z_0 values obtained with the different models vary by about an order of magnitude between the higher and the lower values. The model of Lettau, "height max" and the semi-variogram sill show the higher values, for this period on the second part z_0 is about 0.6 mm. The model "height max" is particularly sensible to extreme values of height because it takes the maximum height to derived z_0 . Munro's model shows lower z_0 values, about half (ca. 0.3 mm) of the values from the three models discussed previously. The model of Chambers, and the "height mean and std" show similar values of about 0.1 mm. The Smith model presents values almost two times lower (about 0.05 mm). Finally the Fitzpatrick model leads to values ten times smaller compared to the model of Smith, therefore it was chosen to put it aside. Overall all the models show the same z_0 variability across the time period.

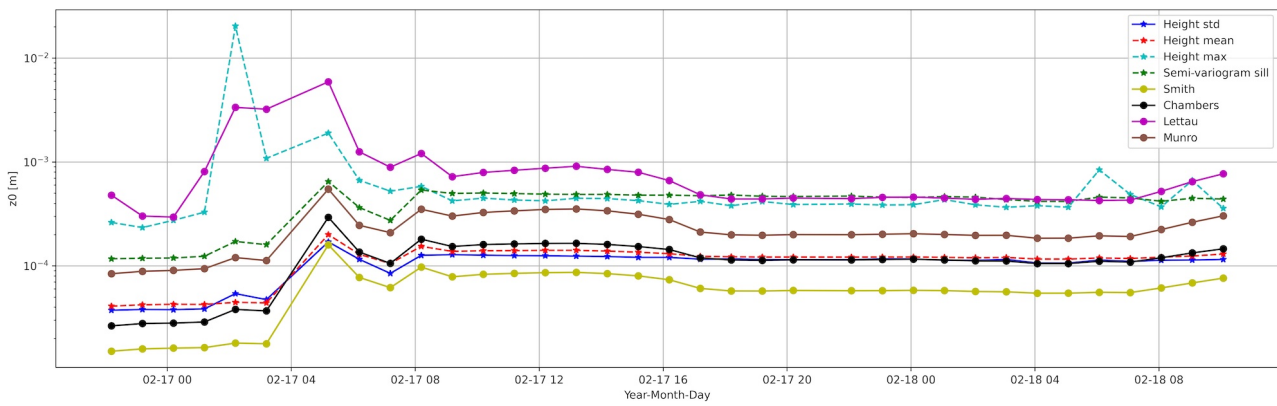


Figure 4.11: Comparison of z_0 calculation for the different models on the period from 2021-02-16 22:11 to 2021-02-18 10:04

Regarding the surface variability for the first 6 h, the surface was quite smooth with differences in height of about 2 cm (see Fig. 4.13(a)), and with relatively constant z_0 values during this period. Then the wind speed increased with a precipitation event (see Fig. 4.12) resulting in a rough surface, with height variations of about 5 cm (see Fig. 4.13(b)), leading to an increase in z_0 . While the wind speed decreased, the surface got smoothed out a bit with height difference of about 2 cm (see Fig. 4.13(c)), and z_0 remains constant from there on but at a slightly higher level.

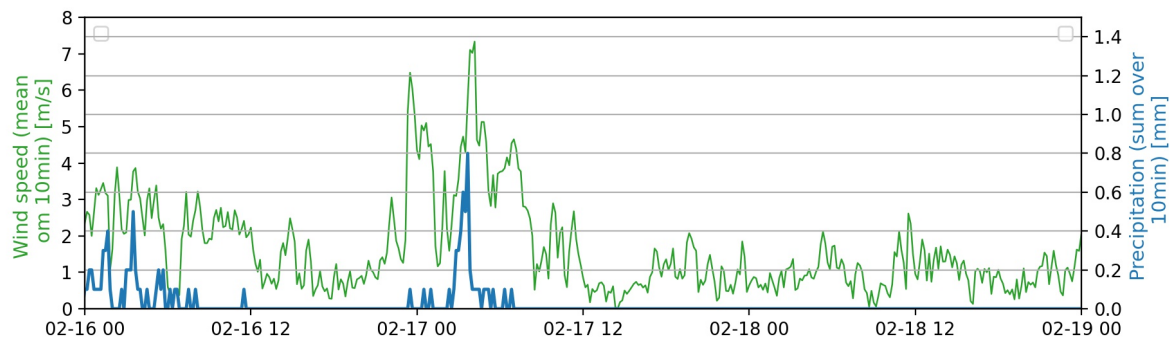
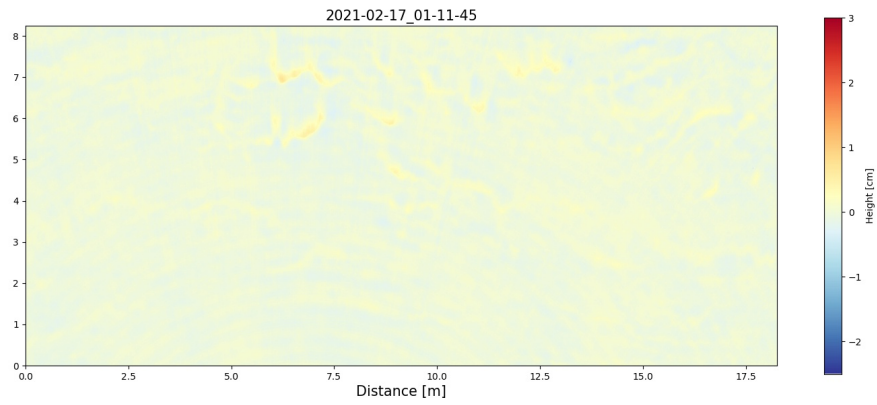
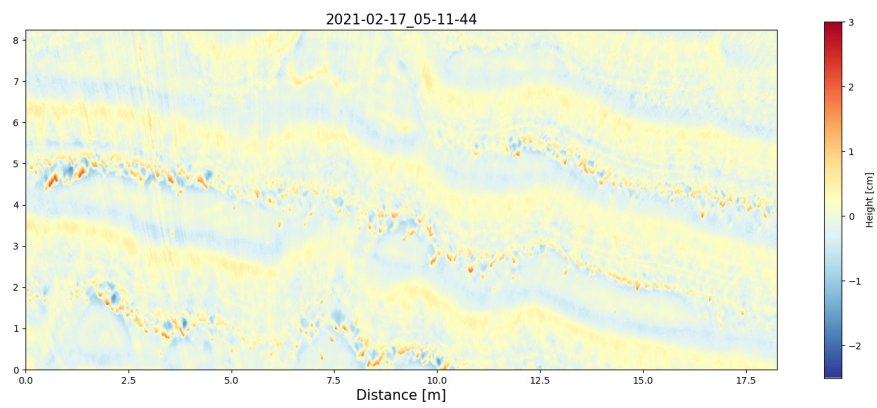


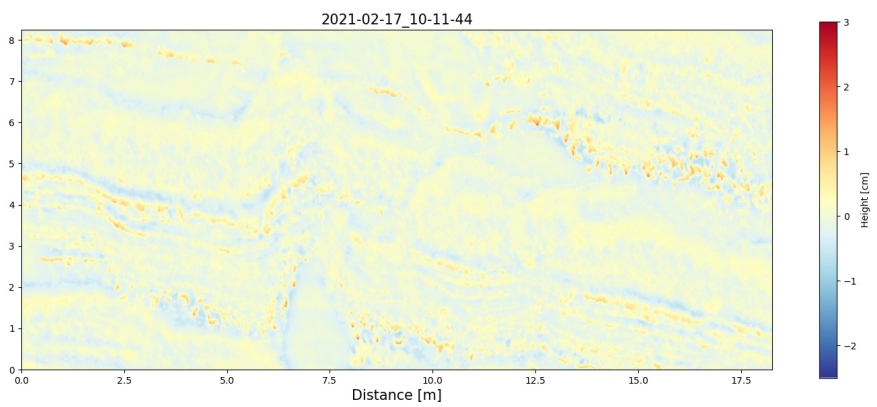
Figure 4.12: Precipitation (mean over 10min) [mm] and wind speed (mean over 10min) [m/s] as a function of time from 2021-02-16 to 2021-02-19



(a) Scan on 2021-02-17 01:11



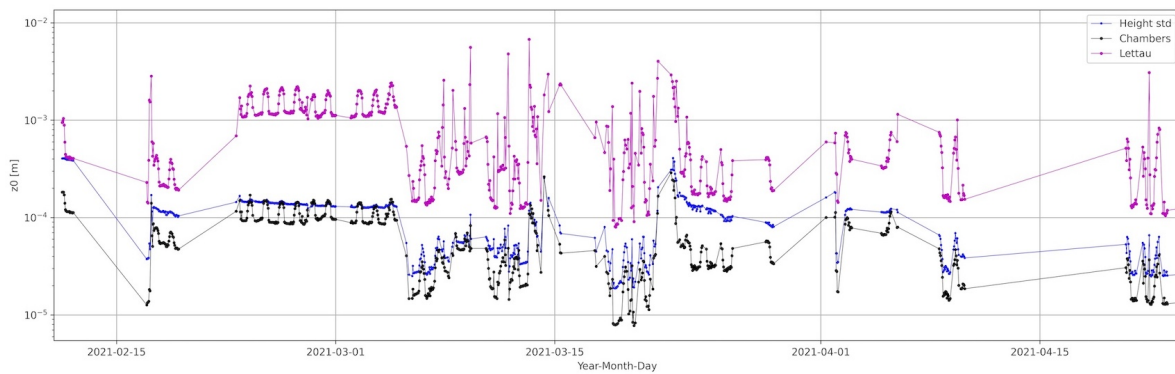
(b) Scan on 2021-02-17 05:11



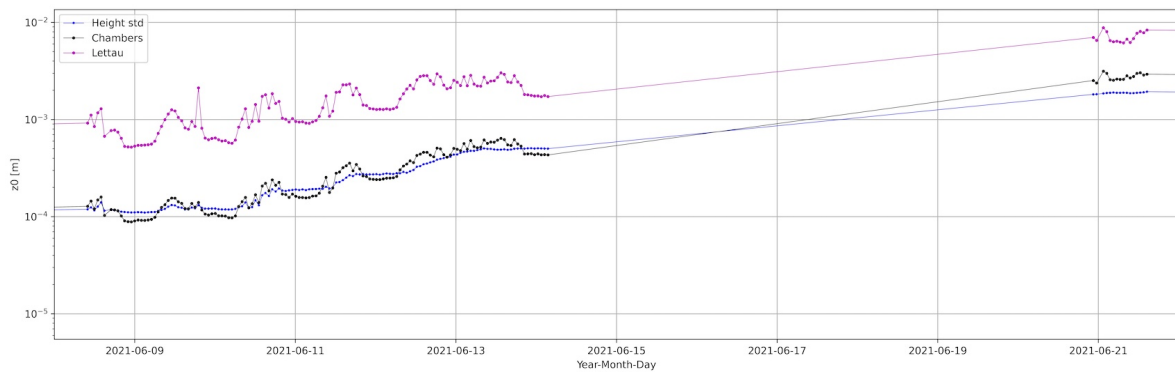
(c) Scan on 2021-02-17 10:11

Figure 4.13: Detrended DEMs for three different scans taken for the period of the model comparison shown in 4.11

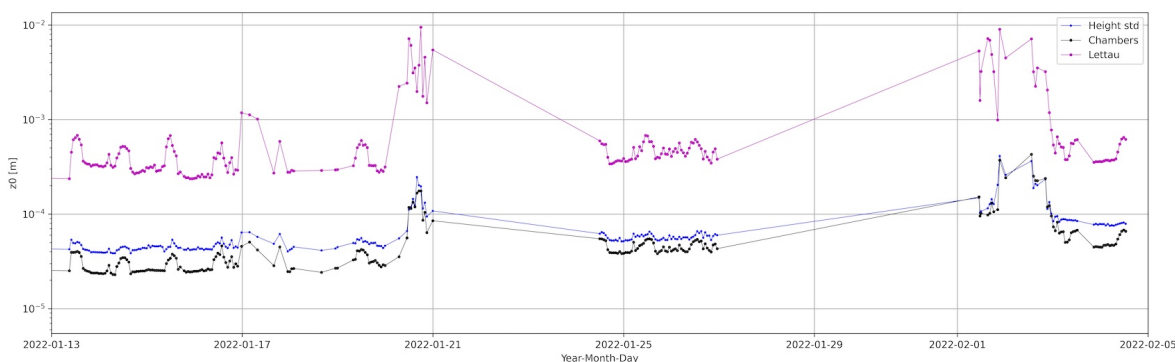
Three models have been chosen to calculate z_0 on all scans: i) the model of Lettau, ii) Chambers, and iii) the standard deviation of the height. The aim is to keep the models that are close to the upper/lower boundaries and to the median of all models to get a readable plot, to get an overview of the temporal variability of z_0 , and to use different types of models based on different assumptions. For the upper boundary, the model "height max" was not chosen in case a few non-ground points would remain, this would lead to an extreme over-estimation of z_0 . For the lower boundary, the model Smith was not chosen as it was somehow apart. Afterwards, a comparison of all models against z_0 from the Sonic is conducted to exclude models based on their performance to estimate z_0 .



(a) February 11 to April 23, 2021



(b) June 8 to 22, 2021



(c) January 13 to February 5, 2022

 Figure 4.14: Topographical aerodynamic roughness length z_0 as a function of time

Figure 4.14 shows the topographical aerodynamic roughness length z_0 as a function of time, for three periods. The first period, from February 11 to April 23, 2021 (Fig. 4.14(a)) overall shows a high z_0 variability over time with variations of more than an order of magnitude for the three models. As expected from the previous comparison, the Lettau model gives higher z_0 values than the others models, and the values derived from the

height standard deviation are slightly higher than the one from Chambers. The larger z_0 variations are observed in particular around mid-March, when there was a strong snowfall event and a lot of wind leading to frequent changes of the surface morphology. At the end of February and beginning of March, a diurnal variability is observed from the models based on Lettau and Chambers equation: z_0 shows a maximum around mid-day and a minimum around midnight. However, this is probably due to an atmospheric variable with a diurnal variability. This could be also due to a few remaining points above the surface which showed also a diurnal variability, it still needs to be investigated and corrected.

The second period, from June 9 to 21, 2021 (Fig. 4.14(b)), shows an increase of z_0 due to the increase in roughness during the melting season, this increase in roughness between early June and the end of June can be observed in Fig. 4.33. Here, again the Lettau and Chambers models show a diurnal variation, which is not representative of the z_0 variation in reality. Between June 9 and 21, z_0 increases by about one order of magnitude with the increase in roughness. The third period, from January 13 to February 5, 2022 (Fig. 4.14(c)), shows large variability in z_0 around January 20 and the beginning of February because of snowfall events and strong wind shaping the snow surface. Lettau and Chambers's models show again diurnal variations. The z_0 values derived are globally in agreement with the literature, over the snow season the z_0 values range from 0.1 mm to 4 mm, by excluding some extreme values. An analysis on the temporal changes of z_0 would be interesting for the continuation of this study.

4.2.2 Anemometric method

The z_0 values derived from the sonic anemometer are presented below. Two time periods are considered for the data: 2022-01-18 to 2022-01-20 and 2022-01-24 to 2022-01-27. The results present very high values of z_0 , for instance in Fig. 4.15 for the first ten hours and on 2022-01-26 at 12:00. It appears that these outliers are likely due to strong changes in the wind direction, which is observed on Fig. 4.16. The sonic probe being adapted for a fixed range of wind direction which is setup for the main wind direction, if the direction is out this range the probe and the metal stick can distort the z_0 values by creating additional turbulence, this is one of the limitation of the setup. Consequently, a filter based on the wind direction is applied to the Sonic data, to keep them only for a fixed range of wind direction.

The z_0 values after filtering are presented in Fig. 4.17 for the period 2022-01-25 to 2022-01-27. They show an amplitude between 0.1 mm and 1.2 mm, however, their evolution seems to be unrealistic because z_0 shows a few strong increases and decreases in a few hours only. The filtered values for the period 2022-01-18 to 2022-01-20 are presented in Fig. 4.18, they range from 0.1 mm to 1.2 mm. Here again the evolution seems unrealistic with strong variations in a few hours. Although they are not as extreme as for the pre-filtering situation, these increases and decreases seem still be due to wind instabilities (variations in wind direction and speed).

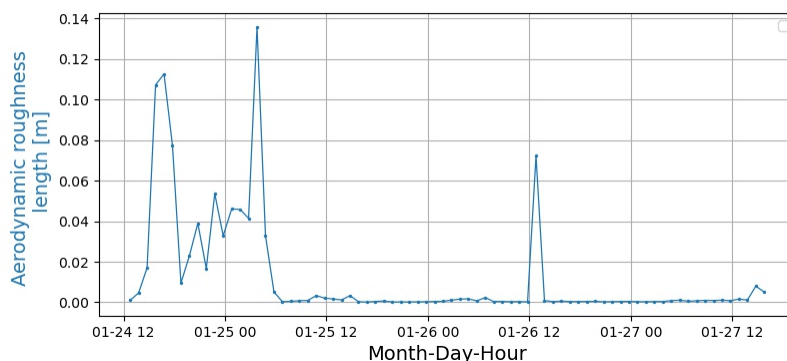


Figure 4.15: Aerodynamic roughness length z_0 as a function of time from 2022-01-24 to 2022-01-27

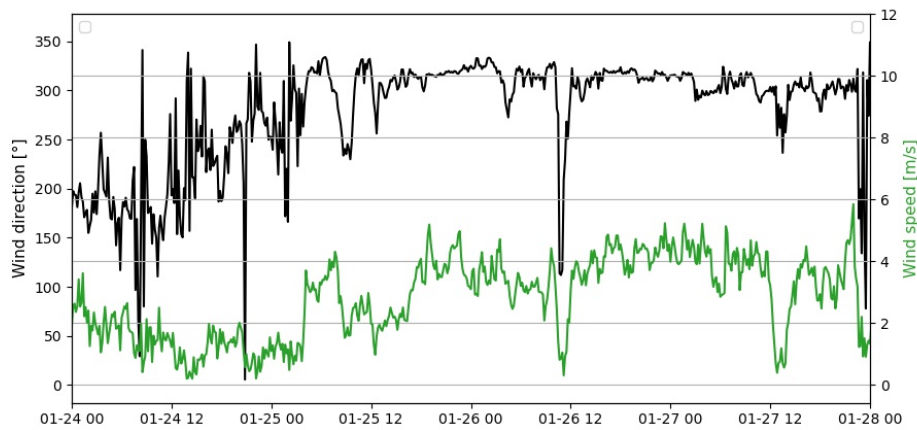


Figure 4.16: Wind speed (mean over 10 min) [m/s] and wind direction (mean over 10 min) [°] at WFJ field site as a function of time (Month-Day-Hour) from 2022-01-24 to 2022-01-27

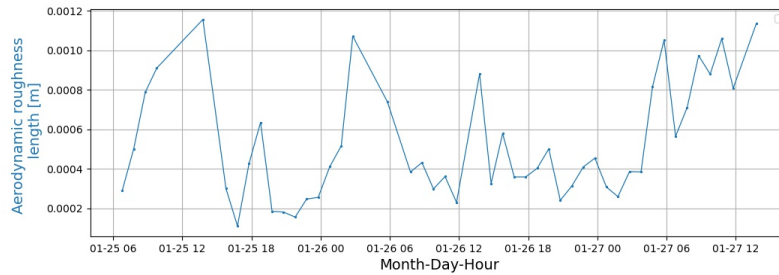


Figure 4.17: Aerodynamic roughness length z_0 as a function of time from 2022-01-25 to 2022-01-27 after filtering

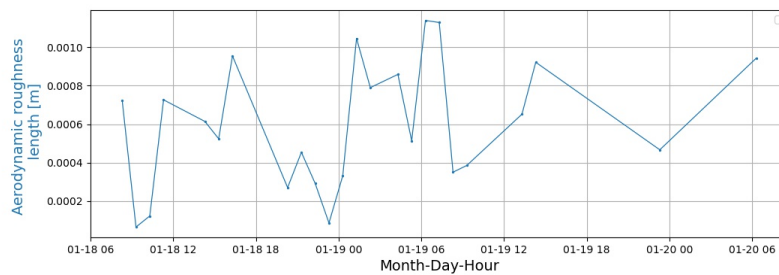


Figure 4.18: Aerodynamic roughness length z_0 as a function of time from 2022-01-18 to 2022-01-20 after filtering

4.2.3 Comparison

The z_0 values from the different models are compared for both periods discussed previously with the z_0 values from the sonic anemometer. Figure 4.19 shows z_0 derived from both approaches for the period from 2022-01-25 to 2022-01-27. It appears that the values from the sonic anemometer showed several peaks far above the data from the scanner, however these peaks already seemed unrealistic and most probably affected by unstable wind speed and direction conditions. Apart from these peaks, the models of Lettau, Height max and Semi-variogram sill are the closest models to the sonic data in comparison the others models. On this period, z_0 is on average equals to 0.53 mm from the sonic, 0.47 mm from Lettau, 0.30 mm from Height max and 0.24 mm from the Semi-variogram sill.

Figure 4.21 presents the z_0 values derived from the sonic anemometer versus derived with the DEMs for each model. This highlights the previous observation, the model of Lettau, Height max and Semi-variogram sill for the derivation of z_0 agree better with the z_0 values from the sonic anemometer in comparison to the other models (Fig. 4.21(d)-4.21(h)), because the point clouds (Fig. 4.21(a)-4.21(c)) are closer to the 1:1 line which is the line where the values from the scanner and the sonic would be identical. The Lettau model shows a moderate positive correlation with the data of the sonic anemometer for this period, with correlation coefficient of 0.26. However, for the model Height max shows a correlation coefficient close to zero ($\rho=-0.03$), and the Semi-variogram sill model is moderately negatively correlated ($\rho=-0.25$). These correlation coefficients are of the same sign as the slope of the linear regression plotted in Fig. 4.21 and colored in red. Based on these elements, the model of Lettau gives the closest estimates of z_0 to those of the sonic for this period.

The z_0 values comparison for the period from 2022-01-19 to 2022-01-20 is presented in Fig. 4.20. Similar to the other period, the models of Lettau, Height max, and Semi-variogram sill are the closest models to the sonic data. In this period, z_0 is on average equals 0.59 mm from the sonic, 0.39 mm from Lettau, 0.38 mm from Height max, and 0.20 mm from the Semi-variogram sill. Figure 4.22 presents the z_0 values derived from the sonic anemometer versus derived with the DEMs for each model. The correlation of the model estimations with the data of the sonic anemometer is similar way to the other period, with $\rho=-0.48$ for the Lettau model, $\rho=0.03$ for Height max, and $\rho=-0.63$ for the Semi-variogram sill.

The model of Lettau for the derivation of z_0 from the scans was found to agree best with the measured z_0 values from the sonic anemometer during stable wind conditions for both periods.

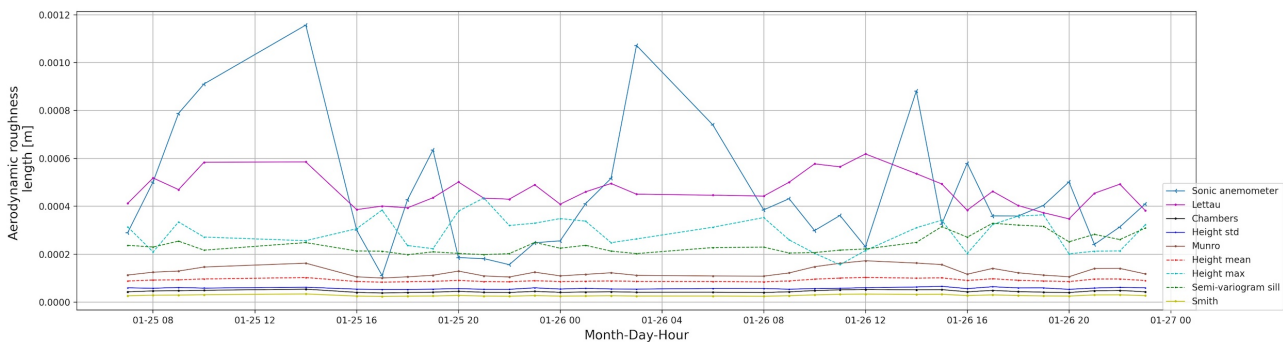


Figure 4.19: Comparison of the aerodynamic roughness length z_0 derived from the sonic anemometer and the laser scanner, as a function of time from 2022-01-25 to 2022-01-27

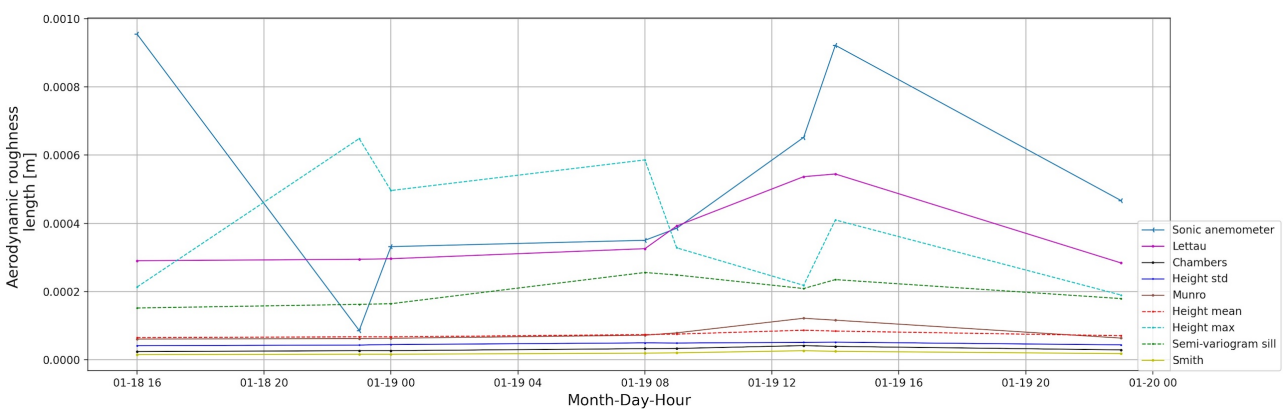
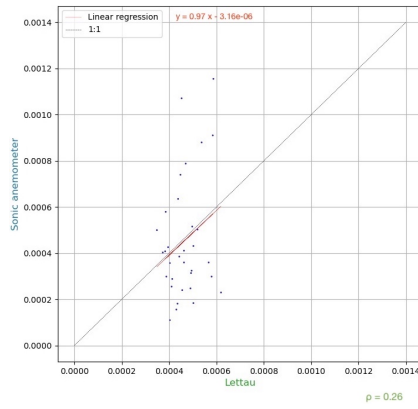
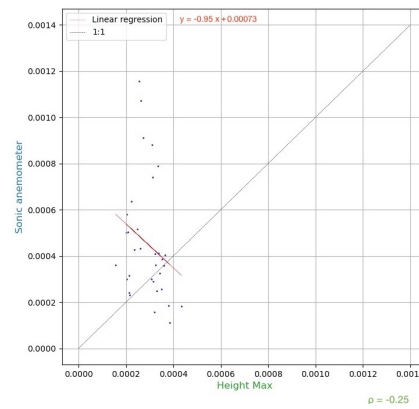


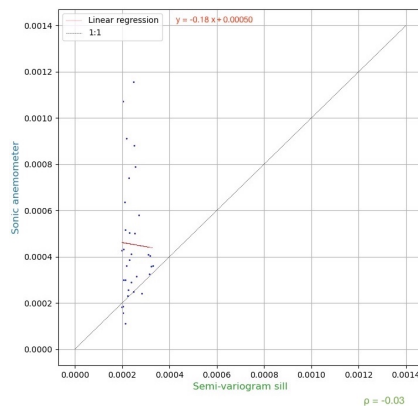
Figure 4.20: Comparison the aerodynamic roughness length z_0 derived from the sonic anemometer and the laser scanner, as a function of time from 2022-01-18 to 2022-01-20



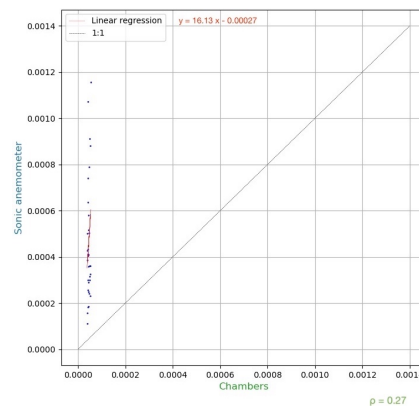
(a) Lettau



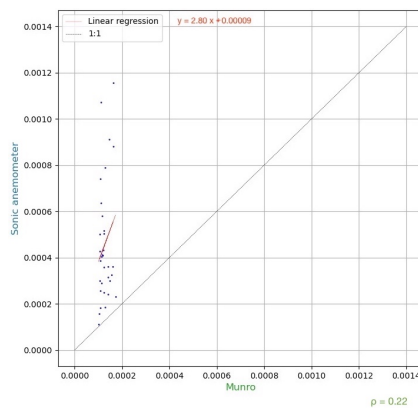
(b) Height max



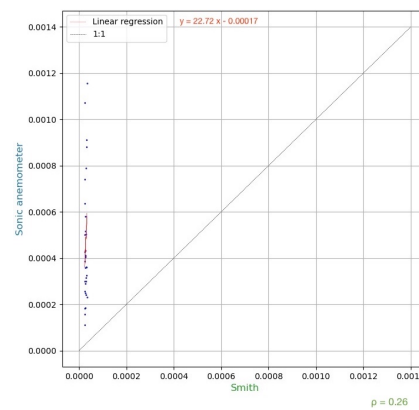
(c) Semi-variogram sill



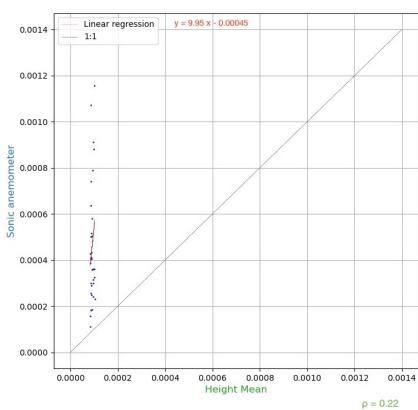
(d) Chambers



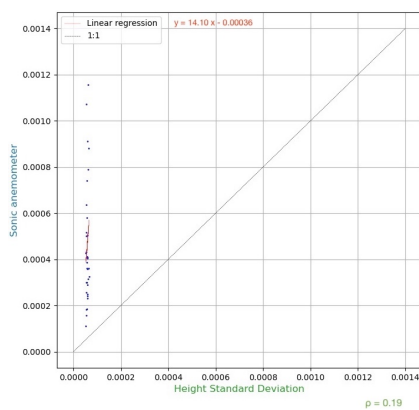
(e) Munro



(f) Smith

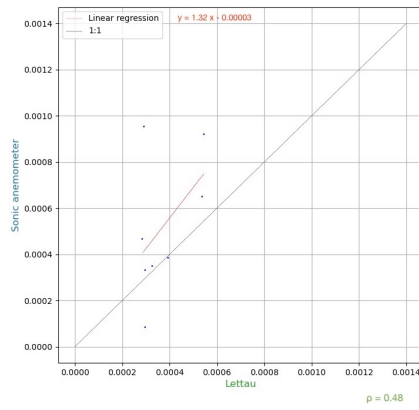


(g) Height mean

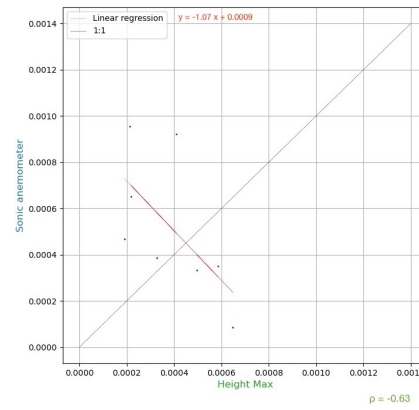


(h) Height Standard Deviation

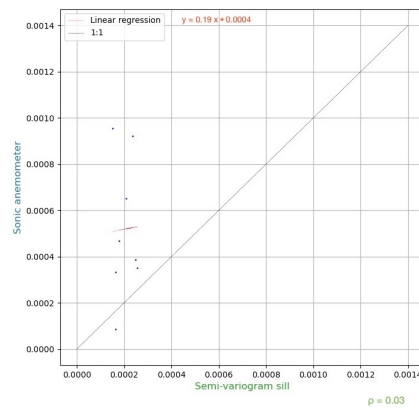
 Figure 4.21: Aerodynamic roughness length z_0 [m] derived from the sonic anemometer versus derived with the DEMs from 2022-01-25 to 2022-01-27



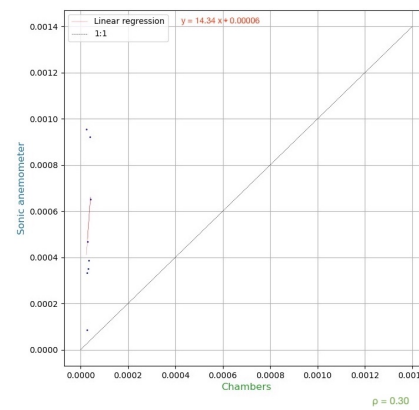
(a) Lettau



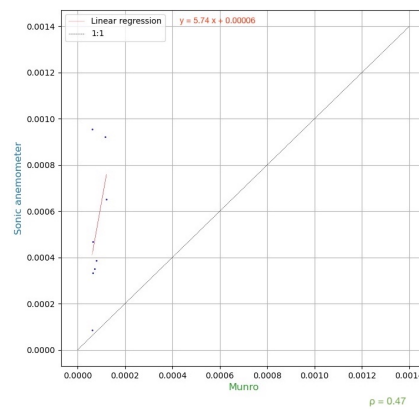
(b) Height max



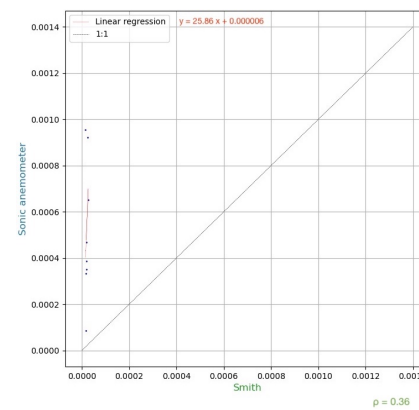
(c) Semi-variogram sill



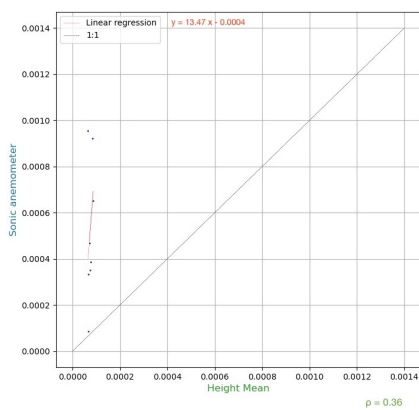
(d) Chambers



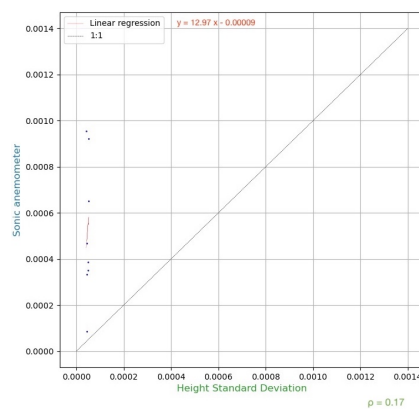
(e) Munro



(f) Smith



(g) Height mean



(h) Height Standard Deviation

 Figure 4.22: Aerodynamic roughness length z_0 [m] derived from the sonic anemometer versus derived with the DEMs from 2022-01-18 to 2022-01-20

4.3 Surface snow type analysis

In this section, an assessment of the potential of the laser scanner to distinguish different surface snow types based on the reflectance values is presented. This section presents the results of an experiment carried out in the SLF cold laboratory with the laser scanner on October 27, 2021, and the results of an analysis of the data from the WFJ field site from November 5-9, 2021, by using the laser scanner data and meteorological data.

The laser scanner determines a reflectance value of the scanned surface by measuring the intensity of the backscattered laser beam. This reflectance value is used to assign a corresponding grey value to every single point in the range 0 - 255 (black-white). Nonetheless, this is not the real "reflectance value" of the snow surface for 905 nm, which would be about 0.6 - 0.9 according to Fig. 4.23, but it is a reflectance value specific to the laser scanner which probably correlates with the real physical reflectance value. Regarding snow surfaces, the signal intensity received by the scanner depends mainly on the snow grain size and the grain shape, whereas the snow density has only a minor influence on the reflectance. An increasing grain size or an increasing liquid water content of the snow cover decrease the reflectance of the surface (Deems et al., 2013), which implies an intensity reduction of the received laser signal. The spectra of reflectance for snow of different grain size is presented in Fig. 4.23. At 905 nm, as the grain size increases or with more impurities in the snow, the reflectance decreases. Moreover, wet snow has a lower reflectance than a dry snow because the reflectance of the water is low at 905 nm (Green et al., 2002). The grain shape, either faceted, dendritic or rounded affects the contribution of specular reflections on the surface and thus the variability of reflectance values from a snow surface.

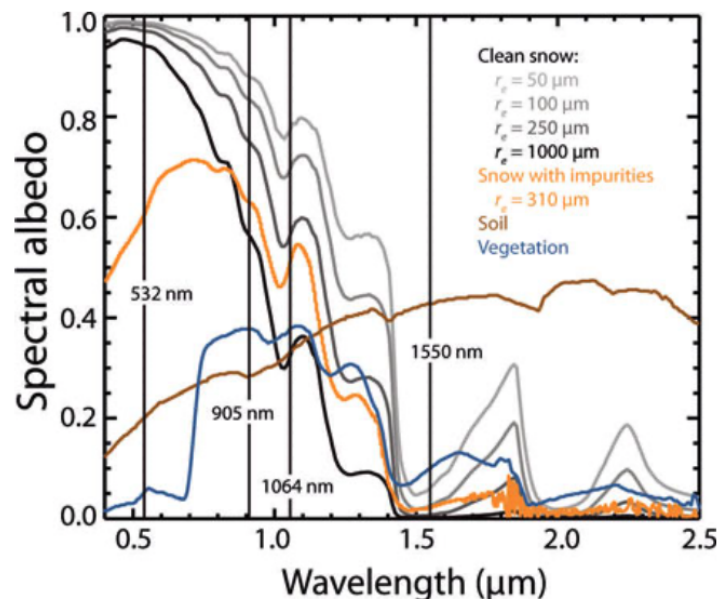


Figure 4.23: Spectra of reflectance for snow of different grain size (50, 100, 250 and 1000 μm), snow with high impurity content (mineral dust with snow grain size of 310 μm), soil and vegetation (source: Deems et al. (2013))

The experiment in the cold laboratory was carried out by Benjamin Walter on October 27, 2021. Three different snow types were scanned with the laser scanner, including depth hoar, rounded grains, and fresh snow. The snow samples contained in boxes are illustrated in Fig. 4.24. The point cloud is illustrated in Fig. 4.25 with the reflectance values as a scalar field.



Figure 4.24: Picture of three different snow types scanned (photo: Benjamin Walter)

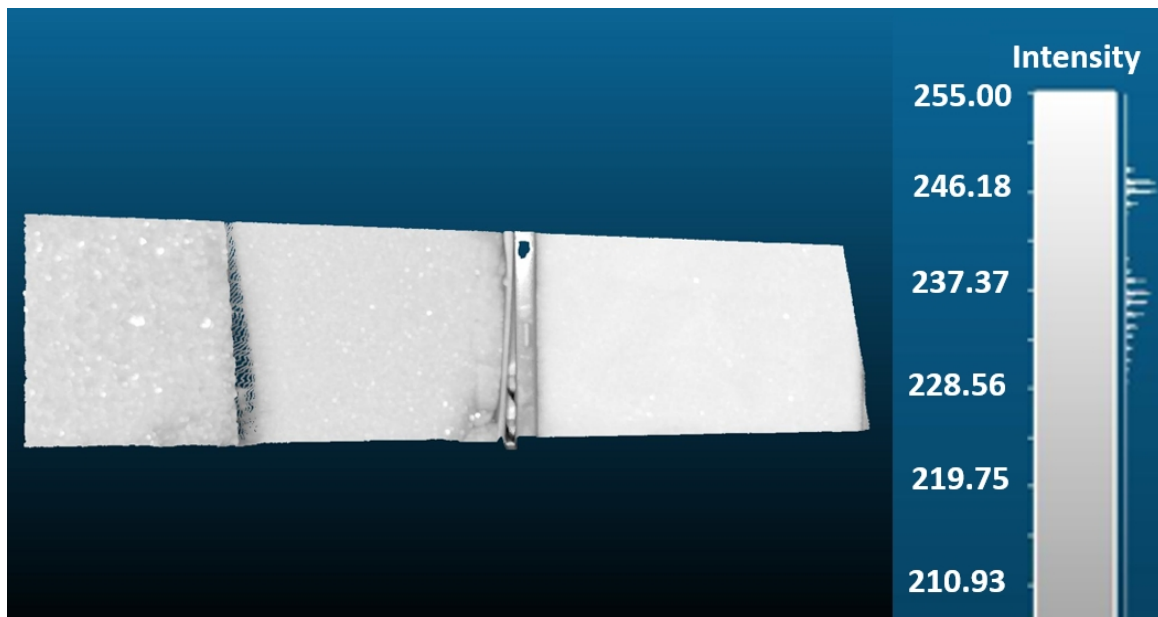


Figure 4.25: Point cloud of the three different snow types scanned, from the left to the right: depth hoar, rounded grains, and fresh snow, with the reflectance values as a scalar field [-] (CloudCompare).

The distributions of the snow reflectance for the three snow types scanned in the laboratory are presented in Fig. 4.26. Notes that the reflectance values given by the scanner are whole numbers. For the three snow types, the distributions are similar to normal distributions. The mean value of the reflectance on the snow surface for each snow type and the standard deviation are presented in Table 4.1. The values of the reflectance range from 0 (minimum) to 255 (maximum). The depth hoar has the lowest mean reflectance (about 235) among the three snow types, the rounded grains mean reflectance is slightly higher (237) and the fresh snow has the highest one (247). For these three different types of snow, the standard deviation of the reflectance is strongly negatively correlated to the mean reflectance values, the Pearson's correlation coefficient is $\rho = -0.81$.

Based on the previous arguments, the difference in the mean reflectance values and the standard deviation can be explained by the different sizes and shapes of the snow grains. The depth hoar has big crystals which can reach a few centimeters, so the specular reflection may strongly deviate the laser light in a certain direction. This results in the more or less bright spots for the depth hoar in Fig. 4.25. That the overall "mean" reflectance is lower for the larger grains is due to absorption of the radiation in the larger ice grains. The larger the grains, the longer the path the light travels through ice and the more light is absorbed in the ice. The highly faceted depth hoar grains result in an inhomogeneous reflectance distribution and thus a relatively large variability of the reflectance values resulting in the high standard deviation (Tab. 4.1).

The rounded grains have a smaller grain size compared to the depth hoar, which results in an overall higher reflectance because less light is absorbed in the smaller grains compared to the depth hoar (Fig. 4.23). The homogeneously oriented rounded grains result in less specular reflections of the laser beam and thus in a lower standard deviation of the reflectance signal.

The fresh snow consists of the smallest grains, therefore resulting in the highest reflectance values at 905nm (Fig. 4.23) and in the smallest standard deviation as the reflectance of the fresh snow surface is quite homogeneous due to the small grain size which is significantly smaller than the incident laser beam with a diameter of approximately 1-2 mm.

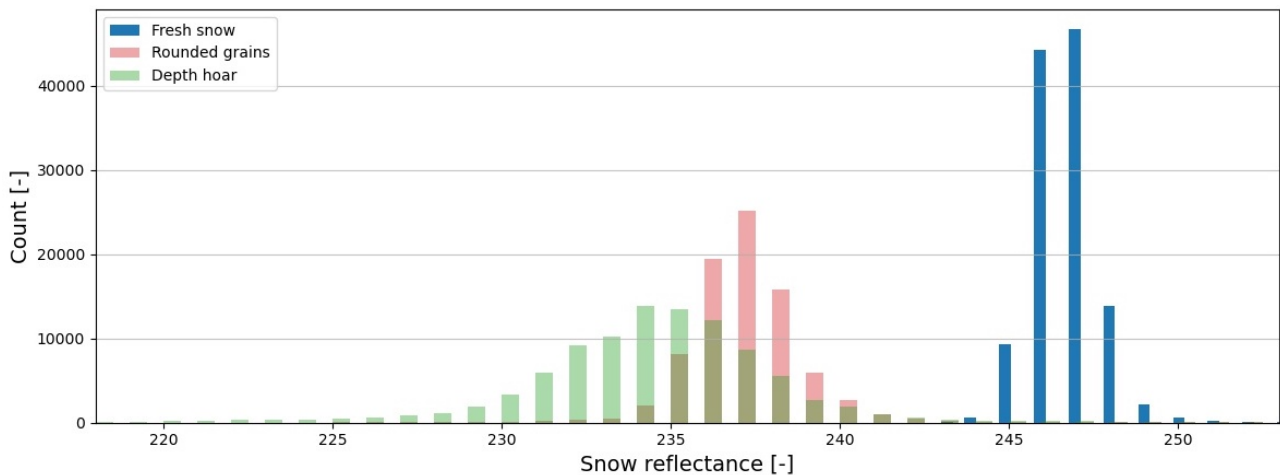


Figure 4.26: Snow reflectance distributions for three snow types scanned in the laboratory

Table 4.1: Statistic indicators for the reflectance measured with the laser scanner in the laboratory for three different types of snow

	<i>Mean</i>	<i>Standard deviation</i>
Depth hoar	234.4	3.79
Rounded grains	237.2	1.70
Fresh snow	246.6	0.98

On November 6, 2021, large surface hoar crystals (> 2 mm) were visually detected on the snow surface at the WFJ field site by Charles Fierz at 08:00. Surface hoar crystals are illustrated in Fig. 4.29(a), and their size can be a few millimeters to a few centimeters like the crystals at the center of the picture. This observation provides the opportunity to compare the reflectance measurement in the laboratory and in the field for surface hoar and depth hoar, and for others snow types. In the laboratory, depth hoar was scanned, whereas in the field it was surface hoar. Nevertheless, both are of about the same size and of similar faceted shapes, and should have similar optical properties. The snow surface reflectance is extracted from the laser scanner data from November 5 to 9, 2021, in order to see the reflectance value for surface hoar in the field, and also to understand how the reflectance is changing over time under the influence of atmospheric variables for a small time period.

The mean snow reflectance is plotted in Fig. 4.27 and is the mean reflectance of the snow over a small surface (about 8 m^2) close to the laser scanner, where the incidence angle is as large as possible (ca. 60°). Between November 5 and 9, the mean snow reflectance is varying between 236 and 240. Its standard deviation, plotted in Fig. 4.27, varies between 3.7 and 5. When the reflectance is high or increasing, its standard deviation is low or decreasing. The plot of the reflectance versus its standard deviation is presented in Fig. 4.28. The Pearson's correlation coefficient between these two variables is $\rho = -0.75$, so they are strongly negatively correlated as for the laboratory experiment.

On Nov. 5, loose new snow was observed on the surface with a reflectance value from the scanner of about 240, which is the highest value of the period studied. The high reflectance value of the new snow was expected based on the experiment in the cold lab and the previous discussion above. The different snow types observed in the field for this period are summarized in Table 4.2.

In the laboratory, the surface hoar reflectance was about 235. In the field, the reflectance decreased to 237-238 in the morning of November 6 when the surface hoar was observed. These two values are close, however the conditions are different between the lab and the field at WFJ: the scanner and the snow surface are more distant in the field and there are disturbing environmental effects like natural radiation. This could result in the field in a slight difference of the reflectance value, and it could explain as well the overall higher standard deviation. The larger standard deviations in the field compared to the lab could also be the result of the surface roughness, which may result in incidence angles of the beam well below the 60° (higher than 30° from the surface normal). A difference in the crystal size of the surface hoar between the field and the laboratory could also explain a change in the mean reflectance value. Furthermore, the snow on the surface analysed everyday is not located in the scanned area, and the snow type could be slightly different between the two areas. Another difference in the experimental setting is that in the field the angle to the vertical was around 30° , whereas it was about 0° in the laboratory. However, the intensity of back-scattered light is expected to be the same from 0° to 30° because the Bidirectional Reflectance Distribution Function (BRDF) is typically quite homogeneous in the range $0\text{-}30^\circ$, thus this difference in between the angles shouldn't affect the reflectance value too much.

On Nov. 7, loose facets are observed on the surface, the snow reflectance is about 238.5. Facets are solid snow grains with multiple flat faces and sharp edges as illustrated in Fig. 4.29(b) and their size can be a few millimeters. On Nov. 8, small surface hoar crystals are observed, however, the snow reflectance increases to about 239. On Nov. 9, loose facets are observed again and the snow reflectance is about 239 - 239.5.

These reflectance values for each snow type are relatively consistent with the lab experiment for Nov. 5-7 in the field, whereas on Nov. 8 and 9 the values are rather high. Nevertheless, this is only a first assessment and evaluation of the laser scanner reflectance values regarding surface snow type determination, which is promising but leaving room for more detailed analyses.

The snow reflectance seems to decrease significantly at noon for each day, and this suggests this could be an effect of solar radiation, because the solar radiation (plotted in Fig. 4.27) is negatively correlated with the mean snow reflectance, with a correlation coefficient of 0.61.

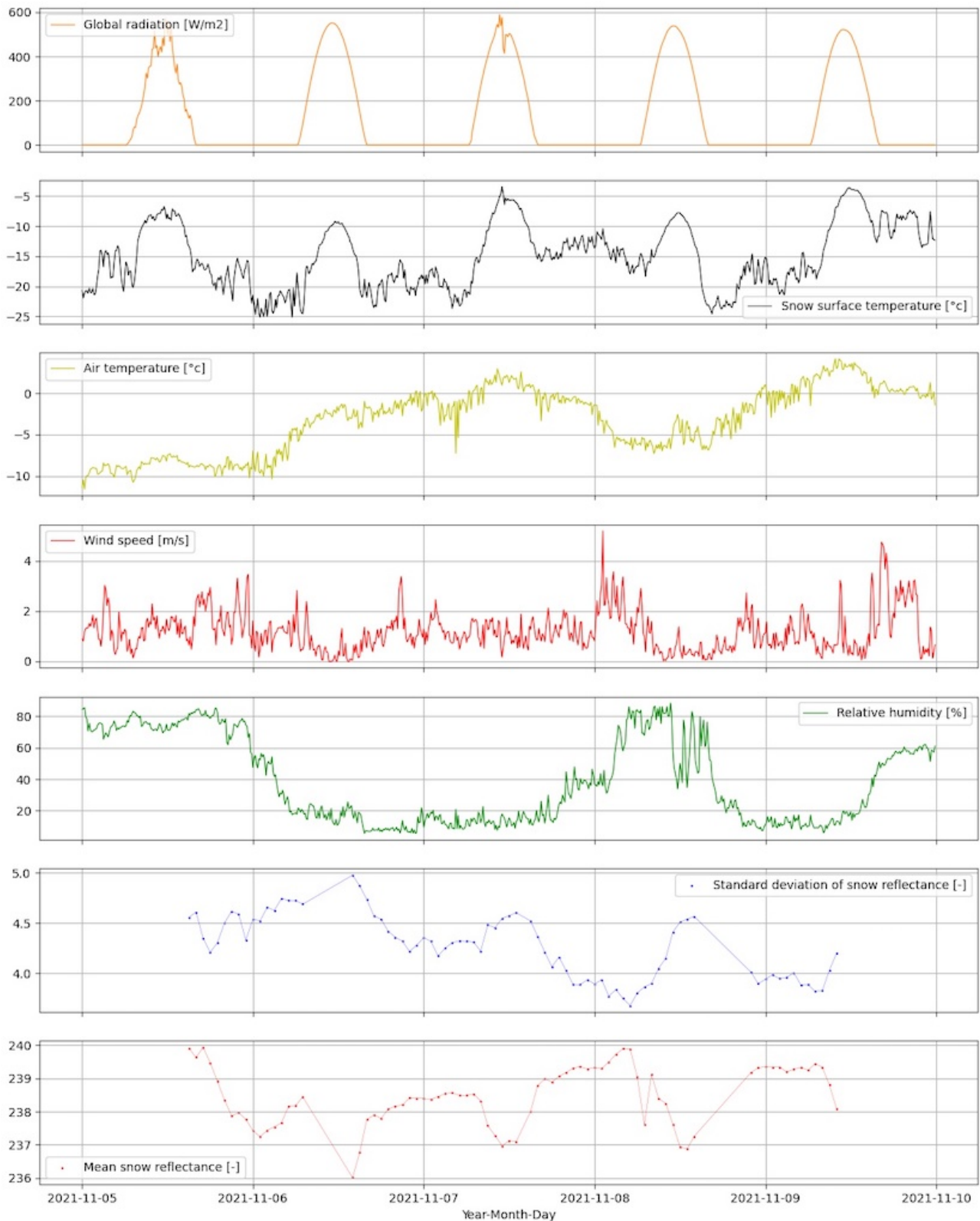


Figure 4.27: Subplot of the snow surface temperature (mean over 30min), the air temperature (mean over 10 min), the wind speed (vectorial mean over 1h), the relative humidity (mean over 10 min), the standard deviation of the snow reflectance value and the snow reflectance value as a function of time from November 5 to 9, 2021. The reflectance ranges from 0-255.

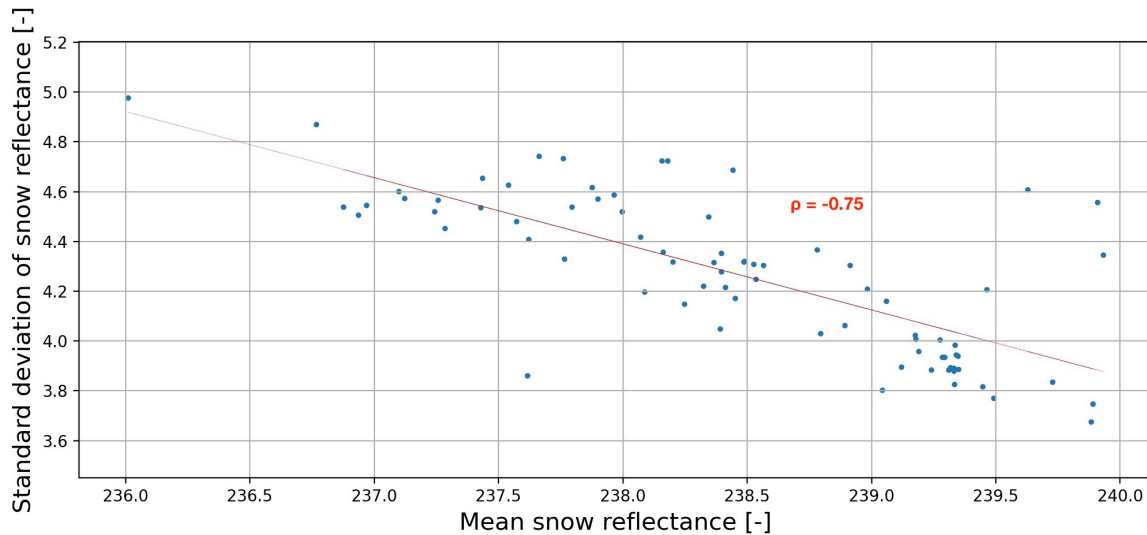


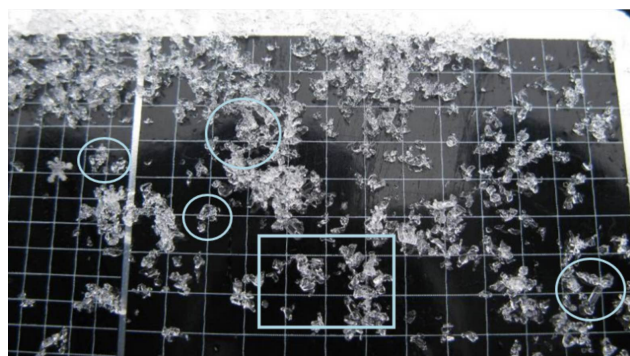
Figure 4.28: Mean snow reflectance versus its standard deviation, with a trendline (red), for the period between November 5 to 9, 2021. The reflectance ranges from 0-255.

Table 4.2: Snow types observed on the snow surface at 08:00 am between November 5 and 9, 2021, at the WFJ field site.

<i>Date</i>	<i>Snow type</i>
2021-11-05	loose new snow
2021-11-06	surface hoar (large)
2021-11-07	loose facets
2021-11-08	surface hoar (small)
2021-11-09	loose facets



(a) Surface hoar



(b) Loose facets (source: snowcrystals.it)

Figure 4.29: Different snow types similar to some observed on the surface between November 5 and 9, 2021

Regarding the surface hoar formed on the snow surface on those days, the reflectance is expected to be lower when the surface hoar is formed on the surface, and the reflectance should decrease during its formation because of the size and shape of the crystals. For those days the sky was clear during the day and the night, so the surface hoar could be formed during the night, early in the morning or late in the evening, because it needs clear sky and no direct or weak sunshine. During the Nov. 5-6 night, the reflectance decreased from 6pm

to midnight which could suggest surface hoar formation, but it increased after midnight. The increase after midnight could be the result of a strongly decreasing relative humidity starting around midnight which may result in sublimation of the surface hoar crystals resulting in the increase of the reflectance value. For the other days, the reflectance slightly increases during the night, whereas it decreases between 7am and noon, however surface hoar formation is not expected at this time because of direct sun light.

Nevertheless, other parameters than the hour of the day and clear sky influence the surface hoar formation. The surface hoar needs humidity to be formed, a cold snow surface, and it needs calm/light wind conditions (Stössel et al., 2010). These parameters are plotted in Fig. 4.27.

First, regarding the relative humidity, three periods of high humidity are noticed (about 50-75%: 05.11 00h00 to 06.11 02:00, 08.11 02:00 to 08.11 14:00 and 09.11 14:00 to 10.11 00:00). These periods should be more favorable to surface hoar formation than the others. Regarding the wind speed, the ideal wind speed is about 1-1.5 m/s for surface hoar formation, which is more favorable to moisture dynamic in the air. The wind speed was often about 1 m/s, and about 2-5 m/s only for a few times. High wind speeds could destroy the surface hoar or make its formation impossible. Nevertheless, given the wind speed, it suggests that it was not a problem for surface hoar formation. Besides, a snow surface colder than the air is needed, so that the vapor from the warmer air condenses on the snow surface. Regarding the data (Fig. 4.27) this could happen almost all the time, but it's probably more favorable when the difference is bigger.

Thus, the ideal conditions for surface hoar formation are: i) a high relative humidity and ii) a snow surface temperature (much) lower than the air temperature. The periods when surface hoar could have been formed are on 05.11 18h00 to 06.11 00:00, although the reflectance increases a bit afterward and the relative humidity drops to 25%, and on 08.11 02:00 to 08.11 11:00, where a low wind speed is observed which could be not ideal but the reflectance decreases until 11:00 when the solar radiation is not weak anymore. These two periods suggested for the surface hoar formation based on the atmospheric conditions are in agreement with the field observations because on the morning of 06.11 and 08.11, large and small surface hoar crystals respectively, were observed on the snow surface.

This analysis of a small-time window allows to distinguish surface hoar and fresh snow, but further investigations would be necessary to understand the influence of the atmospheric conditions on the reflectance value in particular for the small variations during the day. To further investigate this, a test would be to scan different snow types in the field for different atmospheric conditions.

The snow reflectance has also been extracted for the first measurement campaign with the laser scanner, from February 9 to June 22, 2021. Figure 4.30 shows the mean reflectance of the snow (red dots) and its standard deviation (blue bars) as a function of time for February 9 to June 22, 2021. The standard deviation of the snow reflectance value is plotted in Fig. 4.31. The Pearson's correlation coefficient between these two variables is $\rho = -0.45$, they are moderately negatively correlated, a plot of the reflectance versus its standard deviation is presented in Fig. 4.32.

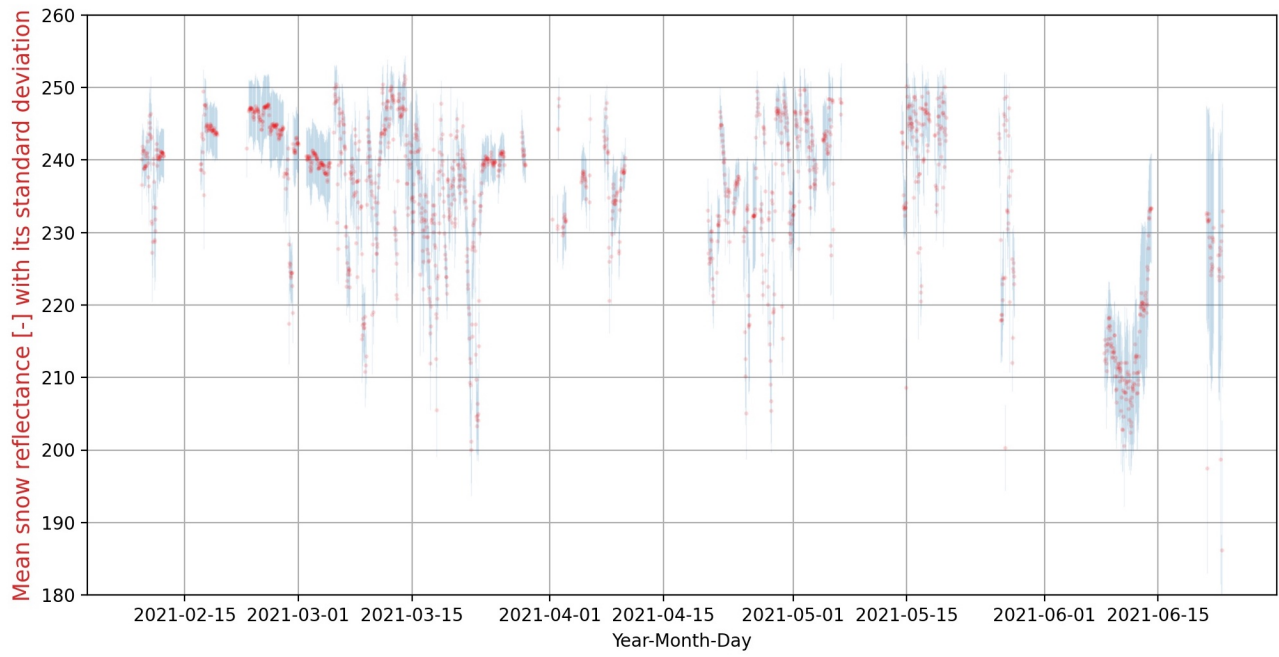


Figure 4.30: Mean snow reflectance as a function of time from February 9 to June 22, 2021. The reflectance ranges from 0-255.

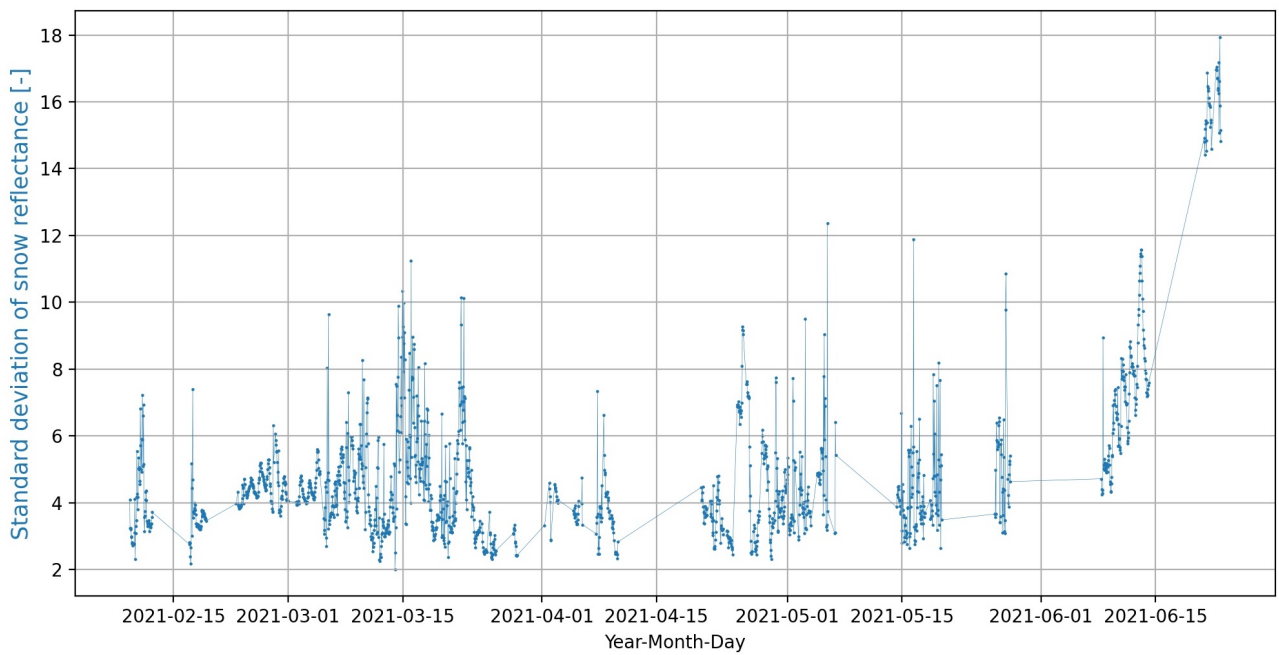


Figure 4.31: Standard deviation of snow reflectance as a function of time from February 9 to June 22, 2021

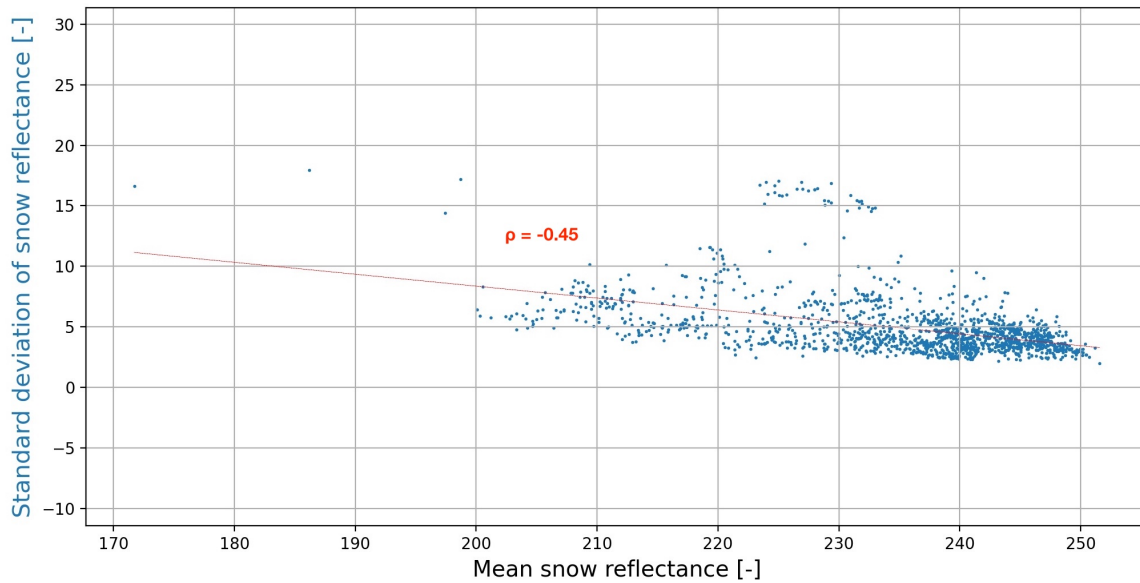


Figure 4.32: Mean snow reflectance versus its standard deviation, with a trendline (red), for the period between February 9 to June 22, 2021. The reflectance ranges from 0-255.

The data for June shows overall much lower reflectance value and higher standard deviations. This is probably due to bigger snow grains and a higher surface roughness implying “shadow areas” where the laser has a very high incident angle which reduces the backscattered light according to the BRDF. Another reason can be due to wetness or impurities on the surface which also decreases the reflectance values.

In June, the surface roughness is higher at the end of the month, with an amplitude of about 18 cm for June 21 (see Fig. 4.33(b)), than in early June where there is an amplitude of about 4 cm for June 9 (see Fig. 4.33(a)). However, the reflectance is much lower around June 9 (about 210) than around June 21 (about 230). The times of high scatter with reflectance values below 220 appears during rainfall events, then they are probably due to precipitation, clouds and to a wet surface. Also, the high scatter in April and May are probably due to wet surface.

Between the beginning of February to the end of May, the snow reflectance is overall between 230 and 250, however, there are outliers with low reflectance values (between 200 and 230) which may be due to a wet surface or precipitation. From the reflectance data, analysis can be conducted for small periods to investigate the temporal changes. Besides, detailed data of the snow type at the surface would be very precious to do more in-depth comparisons.

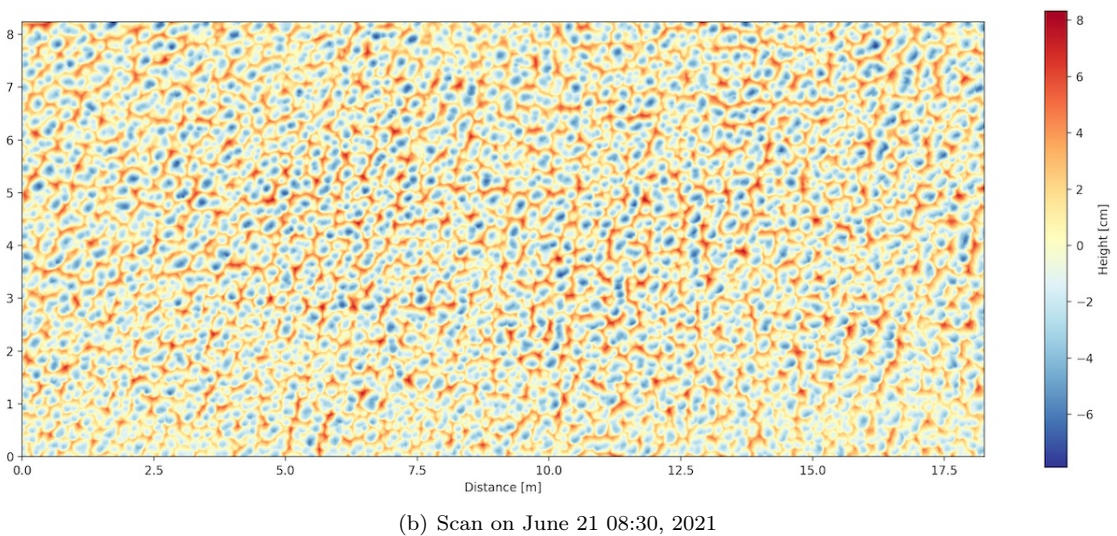
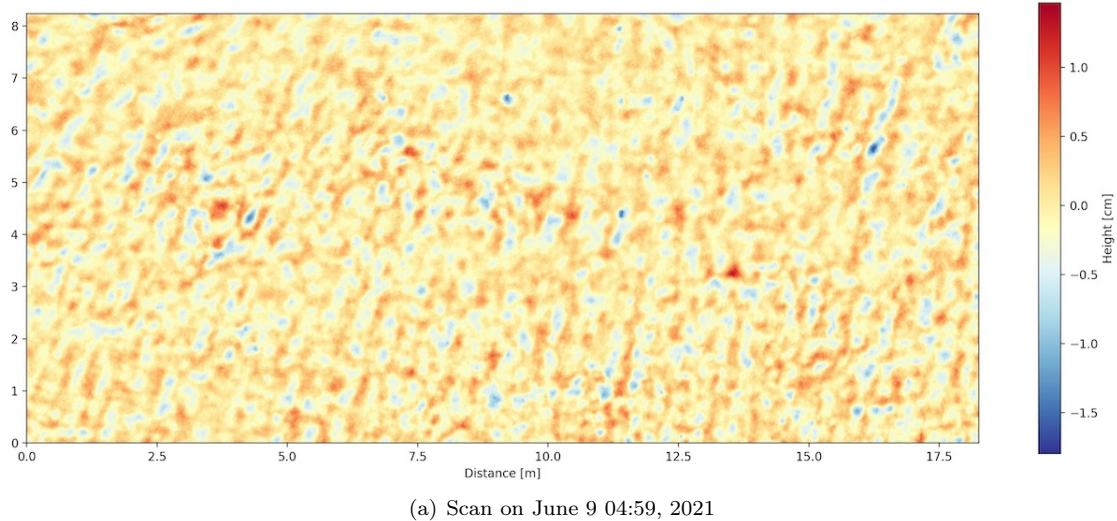


Figure 4.33: Detrended DEMs for two scans to compare the surface roughness

The reflectance values seem to provide good information on the surface grain size and shape for the following conditions: the snow surface is dry, the snow surface is not too rough (to prevent shadowing effects), there is no precipitation or fog, and the solar radiation is low (avoid mid-day in case of clear sky). These situations should be excluded for a future detailed data analysis.

Overall, the high sensitivity of the reflectance values to surface snow type changes is very promising. The obtained reflectance values don't show a perfect agreement with the snow type observations, nevertheless by excluding critical periods the data show promising results for developing a method to monitor the spatio-temporal variability of surface snow grain size and shape.

5 Conclusions and Outlook

This work presented methods and results of a field investigation conducted at WFJ over two winter seasons using a fixed automated high-resolution 3D laser scanner to continuously map the snow surface. This thesis aimed first to produce snow roughness maps and a snow height following from raw laser scanner point clouds. This unique data set demonstrates the ability of the laser scanner to monitor the snow height over the whole season by comparing it with snow height reference measurement. Different models were used to estimate the aerodynamic roughness length z_0 from the micro-topography. A comparison of the different models over a small period showed that z_0 varies by about 1 order of magnitude between the models, but overall z_0 shows the same temporal variability for all the models. A sensitivity analysis of the cell size used for the interpolation process showed that the cell size for the methods based on Lettau's equation has a large impact on the z_0 values, ranging up to 1 order of magnitude or more. Moreover, the window size of the low-pass filter used for the detrending process affects the height of the snow features obtained and has a large impact on the z_0 values if too small, presenting a range up to 1 order of magnitude or more. Over the snow season, the z_0 values range from 0.1 mm to 4 mm which is in agreement with the literature values. The variability agrees also with the observations where z_0 shows a strong variability after strong snowfall or wind events (for instance Mid-march), and z_0 increases during the melting period when the snow surface roughness increases. z_0 was measured in the field using a sonic anemometer, however, a few variations seem unrealistic and are probably linked to wind variability. The model of Lettau for the derivation of z_0 from the scans was found to agree best with the measured z_0 values from the sonic anemometer during stable wind conditions. The model's Height max and Sill give also close results to the Sonic. Furthermore, the temporal evolution of the z_0 values from the scanner was in most cases explained by the prevailing atmospheric conditions for a few short periods, especially for the model's comparison and overall over the season. Finally, the laser scanner reflectance values were found to be very sensitive to surface snow grain sizes and shapes for certain conditions requiring dry snow surface and not too rough to prevent shadowing effects, no precipitation or fog, and low solar radiation. The experiment in the coldlab and on the field site showed the scanner ability to distinguish different snow types and their formation, for instance, when the snow surface reflectivity decreases during the surface hoar formation.

This study raised several questions that could not been fully studied. As a continuation of this work, an outlook would be first to include all the data available from the laser scanner and the sonic anemometer that could not processed from this thesis. z_0 presents a diurnal variability that needs to be explained and corrected in the results. Afterward, a detailed temporal analysis of z_0 changes on all the data would allow to better understand the variability of z_0 with the atmospheric conditions. Moreover, the laser scanner offers a set up with a higher spatial resolution, to do a few scans with a better resolution would be interesting to check that with the interpolation process z_0 converges when the cell size tends a smaller values. The origin of the non-ground points presents in the point clouds is not clearly determined, however, they are negatively correlated with the radiation. Investigate this field would be interesting to understand how the scanner interacts with the natural radiation and to explain why there are non-ground points. Finally, a future study could focused on the reflectance changes over the whole season in comparison with the snow types.

A Additional pictures



Figure A.1: Study area on October 28, 2021 after the installation of the laser scanner

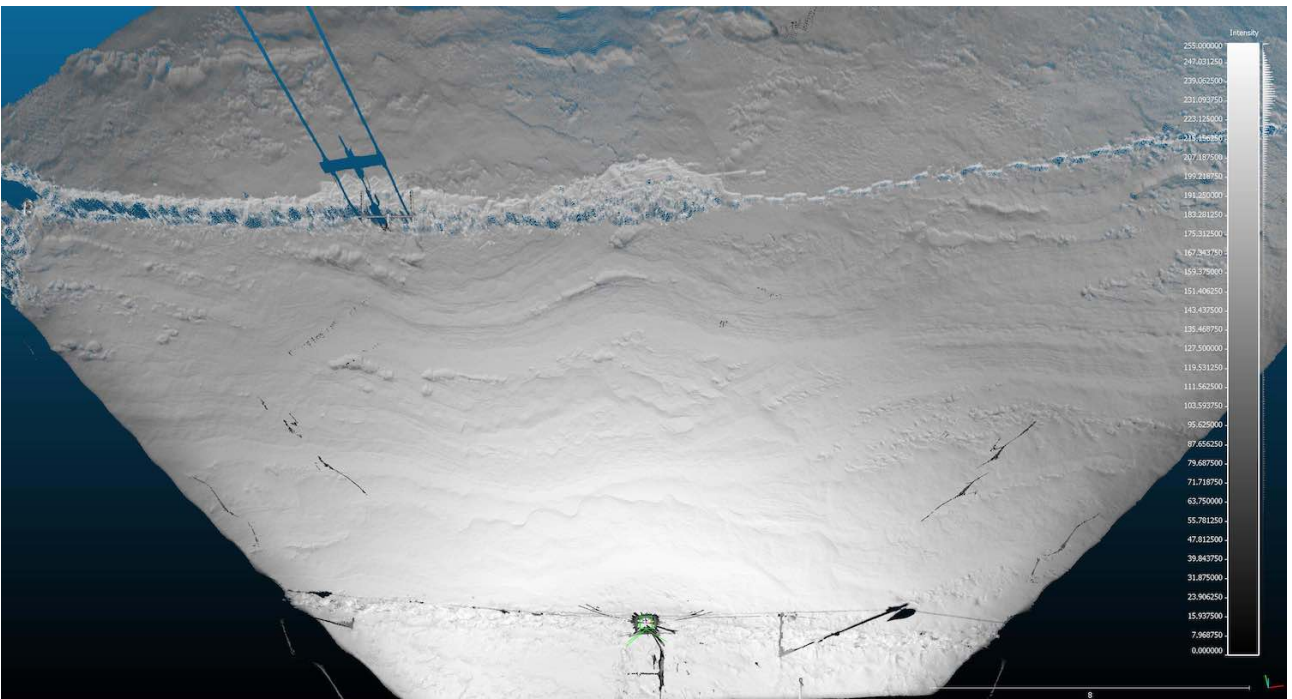


Figure A.2: SPC on the scanned area, scan on the 2021-02-26 04:24



Figure A.3: WFJ field site view from behind (photo: Luca Bianchi)



Figure A.4: WFJ field site view from above (photo: Luca Bianchi)



Figure A.5: Front view of the WFJ field site (photo: Luca Bianchi)



Figure A.6: The scanner set up seen from below

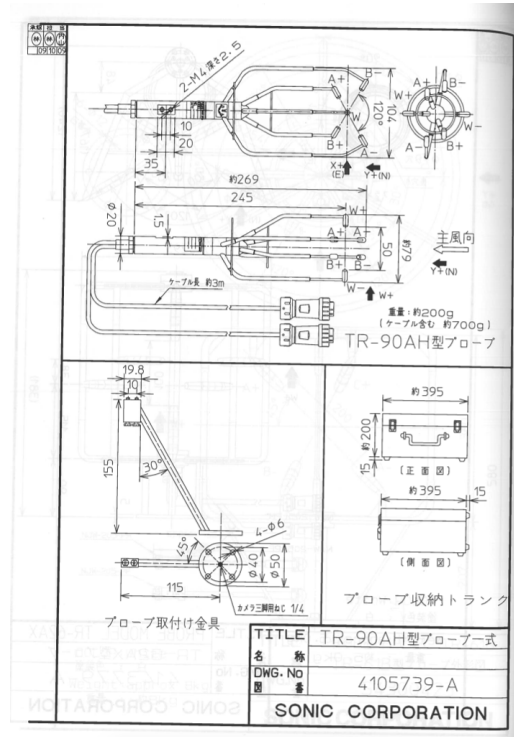


Figure A.7: Schema of the probe TR-90AH (source: Sonic Corporation)



Figure A.8: Installation of the sonic anemometer, the waterproof box contain the converter.



Figure A.9: Snow towers on the snow surface



(a) Snow towers picture (2022-02-24 12:14)



(b) View from the laser scan (2022-02-24 12:23; Cloudcompare)

Figure A.10: Snow towers of the snow surface

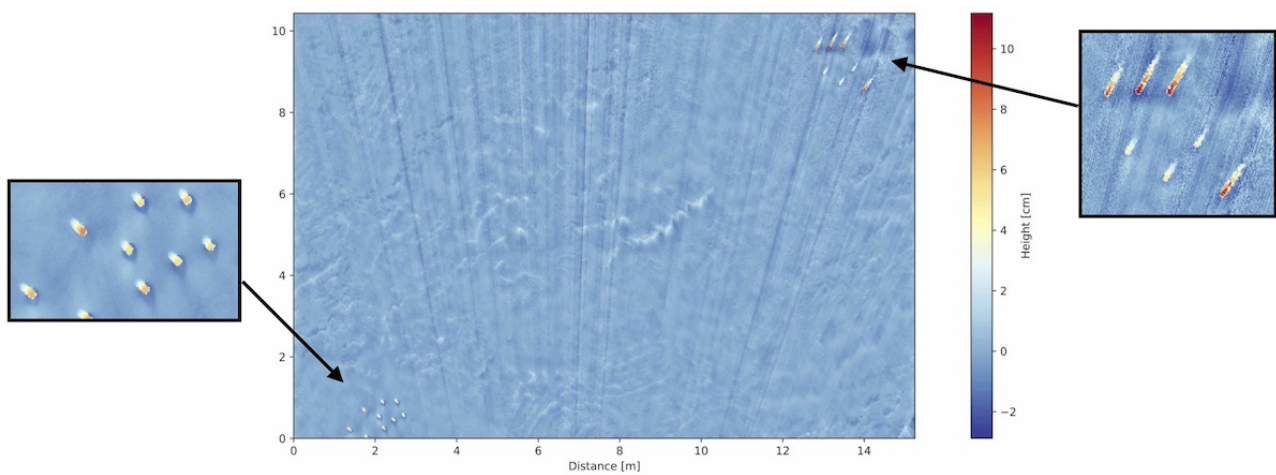


Figure A.11: Detrended DEM of the snow towers (2022-02-24 12:23) with two enlarged windows showing both zone of towers

References

- B. W. Brock, I. C. Willis, and M. J. Sharp. Measurement and parameterization of aerodynamic roughness length variations at haut glacier d'arolla, switzerland. *Journal of Glaciology*, 52(177):281–297, 2006. doi: 10.3189/172756506781828746.
- J. R. Chambers, M. W. Smith, D. J. Quincey, J. L. Carrivick, A. N. Ross, and M. R. James. Glacial aerodynamic roughness estimates: Uncertainty, sensitivity, and precision in field measurements. *Journal of Geophysical Research: Earth Surface*, 125(2):e2019JF005167, 2020. doi: <https://doi.org/10.1029/2019JF005167>. URL <https://agupubs.onlinelibrary.wiley.com/doi/abs/10.1029/2019JF005167>.
- CloudCompare. 2022. URL <http://www.cloudcompare.org>.
- A. Dachauer. Aerodynamic roughness length of crevassed tidewater glaciers from uav mapping. *MS thesis*, 2020. URL https://folk.ntnu.no/richahan/Publications/2020_Dachauer_Thesis.pdf.
- A. Dachauer, R. Hann, and A. J. Hodson. Aerodynamic roughness length of crevassed tidewater glaciers from uav mapping. *The Cryosphere*, 15(12):5513–5528, 2021. doi: 10.5194/tc-15-5513-2021. URL <https://tc.copernicus.org/articles/15/5513/2021/>.
- J. S. Deems, T. H. Painter, and D. C. Finnegan. Lidar measurement of snow depth: a review. *Journal of Glaciology*, 59(215):467–479, 2013. doi: 10.3189/2013JoG12J154.
- J. U. Eitel, C. J. Williams, L. A. Vierling, O. Z. Al-Hamdan, and F. B. Pierson. Suitability of terrestrial laser scanning for studying surface roughness effects on concentrated flow erosion processes in rangelands. *CATENA*, 87(3):398–407, 2011. ISSN 0341-8162. doi: <https://doi.org/10.1016/j.catena.2011.07.009>. URL <https://www.sciencedirect.com/science/article/pii/S0341816211001469>.
- L. S. FARO®. Faro® focus3d s120 manual - february 2013. URL <https://downloads.faro.com/index.php/s/CY5BS9Jd2JEf8YY>.
- N. Fitzpatrick, V. Radić, and B. Menounos. A multi-season investigation of glacier surface roughness lengths through in situ and remote observation. *The Cryosphere*, 13(3):1051–1071, 2019. doi: 10.5194/tc-13-1051-2019. URL <https://tc.copernicus.org/articles/13/1051/2019/>.
- R. Green, J. Dozier, D. Roberts, and T. Painter. Spectral snow reflectance models for grain-size and liquid-water fraction in melted snow for the solar-reflected spectrum. *Annals of Glaciology*, 34:71–73, 01 2002. doi: 10.3189/172756402781817987.
- R. Hock and B. Holmgren. Some aspects of energy balance and ablation of storglaciären, northern sweden. *Geografiska Annaler. Series A, Physical Geography*, 78(2/3):121–131, 1996. ISSN 04353676, 14680459. URL <http://www.jstor.org/stable/520974>.
- R. Hock and B. Holmgren. A distributed surface energy-balance model for complex topography and its application to storglaciären, sweden. *Journal of Glaciology*, 51(172):25–36, 2005. doi: 10.3189/172756505781829566.
- T. D. Irvine-Fynn, E. Sanz-Ablanedo, N. Rutter, M. W. Smith, and J. H. Chandler. Measuring glacier surface roughness using plot-scale, close-range digital photogrammetry. *Journal of Glaciology*, 60(223):957–969, 2014. doi: 10.3189/2014JoG14J032.
- D. Lague, N. Brodu, and J. Leroux. Accurate 3d comparison of complex topography with terrestrial laser scanner: Application to the rangitikei canyon (n-z). *ISPRS Journal of Photogrammetry and Remote Sensing*, 82:10–26, 2013. ISSN 0924-2716. doi: <https://doi.org/10.1016/j.isprsjprs.2013.04.009>. URL <https://www.sciencedirect.com/science/article/pii/S0924271613001184>.

- H. Lettau. Note on aerodynamic roughness-parameter estimation on the basis of roughness-element description. *Journal of Applied Meteorology and Climatology*, 8(5):828 – 832, 1969. doi: 10.1175/1520-0450(1969)008<0828:NOARPE>2.0.CO;2. URL https://journals.ametsoc.org/view/journals/apme/8/5/1520-0450_1969_008_0828_noarpe_2_0_co_2.xml.
- C. Marty and R. Meister. Long-term snow and weather observations at weissfluhjoch and its relation to other high-altitude observatories in the alps. *Theoretical and Applied Climatology*, 110, 12 2012. doi: 10.1007/s00704-012-0584-3.
- E. S. Miles, J. F. Steiner, and F. Brun. Highly variable aerodynamic roughness length (z_0) for a hummocky debris-covered glacier. *Journal of Geophysical Research: Atmospheres*, 122(16):8447–8466, 2017. doi: <https://doi.org/10.1002/2017JD026510>. URL <https://agupubs.onlinelibrary.wiley.com/doi/abs/10.1002/2017JD026510>.
- R. Mott, M. Schirmer, M. Bavay, T. Grünewald, and M. Lehning. Understanding snow-transport processes shaping the mountain snow-cover. *The Cryosphere*, 4(4):545–559, 2010. doi: 10.5194/tc-4-545-2010. URL <https://tc.copernicus.org/articles/4/545/2010/>.
- D. S. Munro. Surface roughness and bulk heat transfer on a glacier: Comparison with eddy correlation. *Journal of Glaciology*, 35:343–348, 1989.
- H. Nfaoui. 2.04 - wind energy potential. pages 73–92, 2012. doi: <https://doi.org/10.1016/B978-0-08-087872-0.00204-3>. URL <https://www.sciencedirect.com/science/article/pii/B9780080878720002043>.
- J. M. Nield, J. King, G. F. S. Wiggs, J. Leyland, R. G. Bryant, R. C. Chiverrell, S. E. Darby, F. D. Eckardt, D. S. G. Thomas, L. H. Vircavs, and R. Washington. Estimating aerodynamic roughness over complex surface terrain. *Journal of Geophysical Research: Atmospheres*, 118(23):12,948–12,961, 2013. doi: <https://doi.org/10.1002/2013JD020632>. URL <https://agupubs.onlinelibrary.wiley.com/doi/abs/10.1002/2013JD020632>.
- L. Prandtl. Über die ausgebildete turbulenz. *Verh. 2nd. Intl. Kong. Fur Tech. Mech. Zurich, (english translation, NACA technical memoir)*, 435:62–74, 1926.
- A. Prokop. Assessing the applicability of terrestrial laser scanning for spatial snow depth measurements. *Cold Regions Science and Technology*, 54(3):155–163, 2008. ISSN 0165-232X. doi: <https://doi.org/10.1016/j.coldregions.2008.07.002>. URL <https://www.sciencedirect.com/science/article/pii/S0165232X08001018>. Snow avalanche formation and dynamics.
- D. Quincey, M. Smith, D. Rounce, A. Ross, O. King, and C. Watson. Evaluating morphological estimates of the aerodynamic roughness of debris covered glacier ice. *Earth Surface Processes and Landforms*, 42(15): 2541–2553, 2017. doi: <https://doi.org/10.1002/esp.4198>. URL <https://onlinelibrary.wiley.com/doi/abs/10.1002/esp.4198>.
- D. R. Rounce, D. J. Quincey, and D. C. McKinney. Debris-covered glacier energy balance model for imja-lhotse shar glacier in the everest region of nepal. *The Cryosphere*, 9(6):2295–2310, 2015. doi: 10.5194/tc-9-2295-2015. URL <https://tc.copernicus.org/articles/9/2295/2015/>.
- J. E. Sanow, S. R. Fassnacht, D. J. Kamin, G. A. Sexstone, W. L. Bauerle, and I. Oprea. Geometric versus anemometric surface roughness for a shallow accumulating snowpack. *Geosciences*, 8(12), 2018. ISSN 2076-3263. doi: 10.3390/geosciences8120463. URL <https://www.mdpi.com/2076-3263/8/12/463>.
- M. W. Smith, D. J. Quincey, T. Dixon, R. G. Bingham, J. L. Carrivick, T. D. L. Irvine-Fynn, and D. M. Rippin. Aerodynamic roughness of glacial ice surfaces derived from high-resolution topographic data. *Journal of Geophysical Research: Earth Surface*, 121(4):748–766, 2016. doi: <https://doi.org/10.1002/2015JF003759>. URL <https://agupubs.onlinelibrary.wiley.com/doi/abs/10.1002/2015JF003759>.

- T. Smith, M. W. Smith, J. R. Chambers, R. Sailer, L. Nicholson, J. Mertes, D. J. Quincey, J. L. Carrivick, and I. Stiperski. A scale-dependent model to represent changing aerodynamic roughness of ablating glacier ice based on repeat topographic surveys. *Journal of Glaciology*, 66(260):950–964, 2020. doi: 10.1017/jog.2020.56.
- F. Stössel, M. Guala, C. Fierz, C. Manes, and M. Lehning. Micrometeorological and morphological observations of surface hoar dynamics on a mountain snow cover. *Water Resources Research*, 46(4), 2010. doi: <https://doi.org/10.1029/2009WR008198>. URL <https://agupubs.onlinelibrary.wiley.com/doi/abs/10.1029/2009WR008198>.
- N. Weber. Wfj mod meteorological and snowpack measurements from weissfluhjoch, davos, switzerland, 2017.
- J. Weil. The synthesis of cloth objects. *SIGGRAPH Comput. Graph.*, 20(4):49–54, aug 1986. ISSN 0097-8930. doi: 10.1145/15886.15891. URL <https://doi.org/10.1145/15886.15891>.
- W. Zhang, J. Qi, P. Wan, H. Wang, D. Xie, X. Wang, and G. Yan. An easy-to-use airborne lidar data filtering method based on cloth simulation. *Remote Sensing*, 8(6), 2016. ISSN 2072-4292. doi: 10.3390/rs8060501. URL <https://www.mdpi.com/2072-4292/8/6/501>.